EUROPEAN ORGANIZATION FOR NUCLEAR RESEARCH
CERN - A & B DEPARTMENT

AB-Note-2004-044 (ABP)

Measurements on Pb^{27+} Sources for the CERN Heavy Ion Injection Chain

James Anthony Chamings

Abstract

CERN, the world's largest particle physics laboratory near Geneva, is currently in the process of building the Large Hadron Collider (LHC). Lead-208 will be used in this accelerator and to meet the injection requirements much work is required to find a suitable and reliable heavy ion source. The work in this report covers two ion sources, the Laser Ion Source (LIS), and the Electron Cyclotron Resonance Ion Source (ECRIS).

An emittance measurement, using a pepper pot and CCD camera, was completed on the recently re-installed LIS, measured and analysed to be 140mm.mrad un-normalised and 0.8mm.mrad normalised 4rms for the maximum intensity charge state, Pb^{27+}.

A Visual Basic Program was modified to allow Charge State Distribution (CSD) and other scans of the ECRIS at CERN to be taken. Chapter 5 presents the results of the CSD scans taken. This program provided a new method to take 1 dimensional transverse beam profiles. From this a direct emittance measurement was formed for the first time since the source was on the test bench. This showed the charge state Pb^{27+} extracted from the source to have 4rms emittance 100mm.mrad un-normalised. This experiment was repeated while the source was providing $Indium^{21+}$ during the summer of 2003, and the emittance recorded as 125mm.mrad.

A 2 dimensional beam profile of the ECRIS is required and in Chapter 7 is a preliminary test to determine the lifetimes of two different types of beam screen. A lifetime was not determined for the Phosphor-47 coated metal plate, due to charge build-up on the surface. A Schott Glass plate, coated with layer of Aluminium of thickness 50nm, was calculated to have a lifetime of 50 minutes when placed after the ECRIS.

A dissertation submitted to the Physics Department at the University of Surrey
in partial fulfilment of the degree of Master in Physics,
Department of Physics, University of Surrey

January 2003 – April 2004

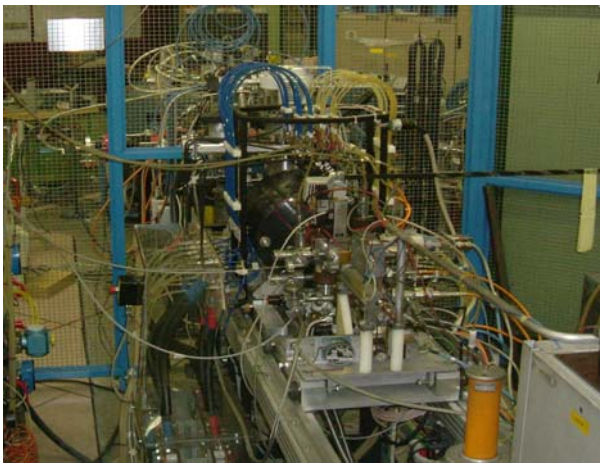

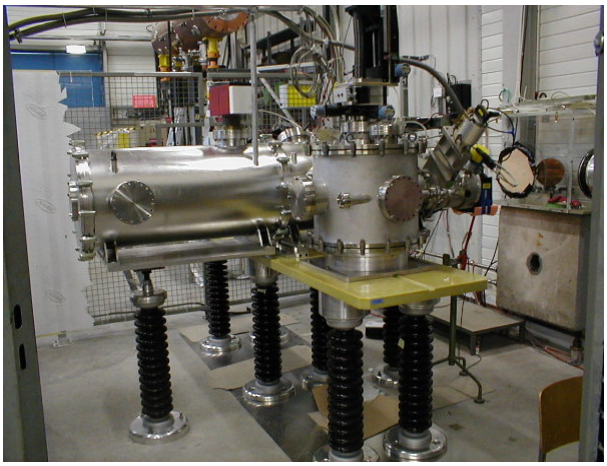

Acknowledgements

The most important mention here goes jointly to Prof. A. Clough, who advised and helped me to achieve a position at CERN for a year, and to Dr. Richard Scrivens, my supervisor at CERN, who always made me feel welcome and gave help whenever needed.

I thank the members of the Laser Ion Source, Hartmut Kugler, Sergey Kondrashev, and Oliver Camut for accepting me into the group at a tough time, and for giving me the name “Young James”. I wish you the best of luck for the future.

The Hadron Sources & Linac group: Charles Hill, Detlef Küchler, Mike O’Neil, Alessandra Lombardi, Thomas Steiner, Victor Coco, and Edgar Sargsyan all gave me support and help with work.

Also the technical expertise of Christian Mastrostefano was very useful over the course of the year.

Personally, I should mention the support my family gave me. Those weekly phone calls did really help Mum!

Lastly, I am sure my year would not have been so great if it wasn’t for my three housemates, Ville, my eternal drinking and girl-chasing partner, Daniel, the Czech who doesn’t drink alcohol! And Gianluca, the postgraduate who always made sure the house was clean. I’ll miss you guys the most.

List of Acronyms

CERN	Conseil Européen pour la Recherche Nucléaire
LHC	Large Hadron Collider
LEP	Large Electron-Positron collider
ALICE	A Large Ion Collider Experiment
I-LHC	heavy Ions for LHC
LIS	Laser Ion Source
MO-PA	Master Oscillator and Power Amplifier
LEAR	Low Energy Accumulation Ring
LEIR	Low Energy Ion Ring
Linac	LINear ACcelerator
ECR (IS)	Electron Cyclotron Resonance (Ion Source)
PS	Proton Synchrotron
IH	Inter-digital H structure tank
RF	Radio Waves
SPS	Super Proton Synchrotron
SEM	Secondary Emission Monitor
LEBT	Low Energy Beam Transport line
MEBT	Medium Energy Beam Transport line
PSB	Proton Synchrotron Booster
CSD	Charge State Distribution
FWHM	Full Width at Half Maximum
RFQ	Radio Frequency Quadrupole
HSL	Hadron Sources and Linac group
RMS	Root Mean Square

Contents

Roll Of The Author

During my year at CERN, I was lucky enough to work with two different lead ion sources. It was fortunate that the majority of people working on these were English speaking, so communication was not a problem.

For the first 3 months I was part of the Laser Ion Source research group. This consisted of 4 members and me. Because this source was a separate (from the main accelerator complex) research project, these members had the say of what occurred day-to-day, and I felt I had a slight influence. This allowed me to become a part of the project by helping out each member completing various hands-on tasks, while I was settling into life abroad. One such task was relocating the extraction electrodes, or when a flood occurred, to pump out many litres of water. I particularly enjoyed preparing objects to be placed into vacuum, be it a whole vacuum chamber or the emittance device used in Chapter 4. That chapter explains the measurement I was assigned, which was taking the emittance of the newly installed laser system. With help from my supervisor, I assembled the apparatus, which among other things involved testing the system for breakdowns under high voltage. The whole team operated the source for me, while I took pictures using the CCD camera. Then it was responsibility to analyse all the data recorded. Once I found the result, it was necessary to report back to the rest of the group. It was very rewarding to feel responsibility in a cutting-edge research group.

With the Laser Ion Source moving to Russia, I become a part of the group that looked after the Linac's. Fortunately, I did not move far, my supervisor was already a part of this work, and could help introduce me to the new equipment. However, because Linac 3 is part of the main accelerating complex at CERN, the hands-on work decreased for several months, as everything has to be checked with supervisors and above. Hence I spent more time in the office programming and simulating. I soon learnt how to control Linac 3 using the computers, and often helped other students become familiar with the controls, for measurements to back up simulations. I also had some minor tasks, apart from the measurements in this report. These included designing the beam line and support for the beam profile measurement taken in Chapter 7. From this I acquired some experience in technical drawing and how to communicate with technicians building my design. Also I completed a 3 dimensional simulation of the Electron Cyclotron Resonance Ion Source using KOBRA, which helped me develop my knowledge of the theory of this source. An electro-magnetic field simulation of a dipole magnet was needed to test a theory for the multi-charge acceleration, and so I spend some time evaluating that.

Chapter 1: Introduction

1.1: Introduction to CERN

The Conseil Européen pour la Recherche Nucléaire [1-1], known as CERN, was formed in 1951, when 11 European governments wished to study the fundamental nuclear physics problems of that time [1-2] as a joint institute. They decided to build a laboratory near Geneva for this purpose. Since then CERN has become the world's largest particle physics research centre, expanding the laboratories into France, and gaining many more contributing countries. It has strived to produce groundbreaking results, and its achievements include the invention of the drift and multi-wire proportional chambers, and the discovery of W and Z bosons [1-2]. Now, CERN's goal is to constantly look towards the future for the next way to improve high-energy physics.

The current project that CERN is working towards is the Large Hadron Collider (LHC). Due to be commissioned in 2007 and housed in the existing 27km tunnel previously used for the Large Electron-Positron collider (LEP), the LHC is expected to be the most powerful particle accelerator ever made, reaching energies for proton collisions at 7 to 7 TeV [1-3], and lead-208 particle energies of 2.76 TeV/u [1-4]. Many projects have been developed for the LHC, including research into high magnetic field type 2 super-conducting magnets, producing 8 Tesla to bend the particles around the ring. Also, the data acquision from the experimental detectors is so large, the computing department has broken records for data transfer in their studies, reaching over 2 giga-bytes per second. With this accelerator installed, detectors such as ALICE (A Large Ion Collider Experiment) will be used to search for and investigate the properties of quark-gluon plasma. From this it is hoped we can get a better understanding of what happened a very short space of time after the big bang.

1.2: The Heavy Ion Injection Chain and Choice of Sources

To allow the LHC to operate at maximum energy, the injector chain must fulfil certain parameters. This chain consists of the current generation accelerators at CERN, and these can be seen in Figure 1. For the heavy Ions for LHC (I-LHC), this has proved to be challenging. Firstly, there was a choice to either use a Laser Ion Source (LIS), to make a single turn injection chain, or the conversion of a Low Energy Accumulation Ring (LEAR) into a Low Energy Ion Ring (LEIR) for a multi-turn injection procedure.

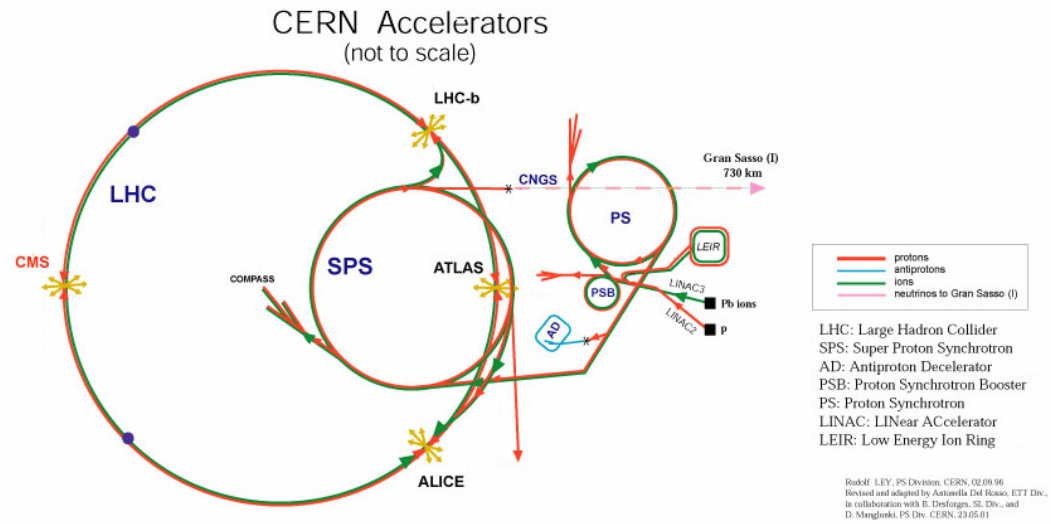

Figure 1: The CERN accelerator complex.

A LIS research team has been working at CERN for many years [1-5]. The goal is to find a high current, single turn injection source suitable for the LHC. In 2002, a 100J, 26ns laser was delivered to CERN, in the hope that increased power would be able to produce more reliable results. An overview of this system is described in the experimental apparatus. However, due to the cost overrun of the LHC, research and development has been restricted such that the LIS study has been terminated at CERN.

Another option for the I-LHC injection chain is the LEIR route. The path of the Ions is shown in Figure 2.

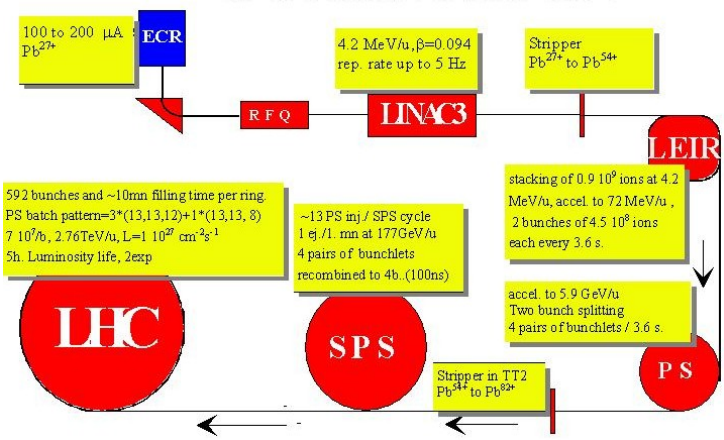

Figure 2: Path of Lead Ions Using the LEIR injection chain [1-8].

The existing lead pre-injector is the 4.2MeV/u Heavy Ion Linac, known as Linac 3. This is optimised to provide beams of $_{208}Pb^{27+}$, using an Electron Cyclotron Resonance (ECR) source running at 14.5GHz [1-6]. After a Radio Frequency Quadrupole (RFQ) the beam is accelerated through 3 Interdigital H (IH) tanks, and then placed through a stripper that increases the charge state of the ions to Pb^{53+}. The beam then passes to the PS booster and into the accelerating complex. For the LHC beam, the ECR source will be upgraded to produce a higher intensity ion beam, and an extra Radio Frequency (RF) cavity will be placed after the last IH tank, to ramp the energy of the ion beam during injection. Once in LEIR, the ions are first cooled, to reduce emittance using strong electron cooling techniques [1-7], then stacked into bunches, and accelerated to 72MeV/u. This forms 4 of the 592 bunches needed to fill the LHC ring. From there, the existing path of PS to SPS and to LHC is taken, accelerating the beam as shown in Figure 2. Using this process would take 10 minutes to fill the LHC.

It was decided that the LEIR would be the best method for the I-LHC, and the conversion process has already begun. This decision had a follow-on effect for Linac 3, which would be creating and providing the heavy ions for LEIR. It was calculated that the injection parameters required a greater intensity beam from the Linac, as the present beam would mean very stringent loss requirements further along the injection chain. Therefore a complete restudy of Linac 3 was proposed for 2003, to asses if any bottle necks exist, which if found, could provide a cheap an easy method to increase the intensity.

Chapter 2: Theoretical Background

2.1: Beam Dynamics

All particle beams consist of a stream of charged particles. Hence all beam dynamics deals with how the particles interact with electric and magnetic fields surrounding them.

A particle with charge q moving with velocity **v** in the presence of a magnetic **B** and electric **E** field is acted upon by a force **F** as given by [2-1]:

$$\mathbf{F} = q\mathbf{E} + \frac{q}{c}(\mathbf{v} \times \mathbf{B}) \tag{2.1.1}$$

Where c is the speed of light. This is the Lorentz force and the motion of all charged particles in a magnetic field depend on this. The Lorentz force shows why electric fields are used for accelerating and magnetic fields are used for bending and focusing. The first term in (2.1.1) is the component of the force created by electric fields, and this acts in the same direction as the velocity of the particle. It does not depend on the velocity, this is why electric fields can be used when the particles are almost stationary, e.g. in a source, and also to accelerate the particle near to the speed of light. Due to the vector product in the term for the magnetic field, the component of the force created by a magnetic field only acts perpendicular to the velocity of the particles, and hence does not give energy to a particle.

2.1.1: Beam Emittance and the Twiss parameters

Emittance is a very important parameter for particle beams, as it leads to the size of the beam pipe required, and also the collision rate in a collider [2-1]. It considers the position and

momentum of the particles, hence it is able to describe the distribution within the beam. It is divided into three coordinates corresponding to horizontal, vertical and longitudinal planes.

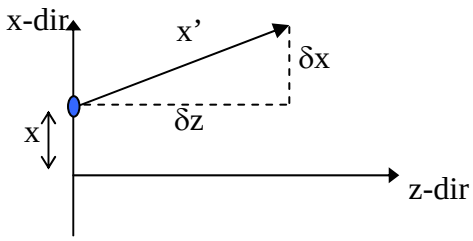

Figure 3: Showing position and motion of a single particle within a beam.

Consider a single particle within a beam travelling along the z axis, as shown in Figure 3. Its x position is the distance the particle is away from the z axis, and the x' value is the direction (or slope) of the particle, which is the transverse momentum. This gives the particles co-ordinates in phase space as:

$$\left(x, x' = \frac{\partial x}{\partial z} \right) \tag{2.1.1.1}$$

For a beam that is diverging in the x direction, the comparison between particle position and phase space diagram is shown in Figure 4.

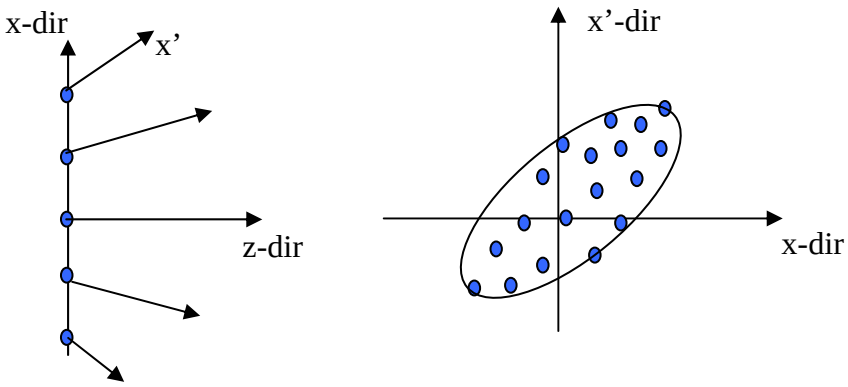

Figure 4: Showing the comparison between particle positions and phase space.

If the x, x' co-ordinates of the particles are plotted, it will generally form a phase ellipse of the general equation [2-2], where a^2 is the area, and b, c and d characterise the phase ellipse shape:

$$bx^2 + 2cxx' + dx'^2 = a^2 \tag{2.1.1.2}$$

The shape of the ellipse gives you information of the characteristics of the beam. For example in Figure 4, because the ellipse is "leaning" forward, we know that the beam is diverging in the x-plane. We can also tell the beam envelope size (beam width) from the maximum extent of the ellipse in the horizontal direction.

There are many ways to define emittance, but the simplest is to say that the emittance multiplied by π, is the area of the phase ellipse, which encircles all the particles within the boundary. This is called the total emittance [2-2].

$$area\ \ of\ \ ellipse = \pi a^2 = \pi.\varepsilon_{total} \tag{2.1.1.3}$$

The different definitions of emittance depend on how you measure the area of the phase ellipse. For example, if you have an ideal Gaussian beam, but then you have one exception, a particle that is very far away from all the others, the *total* emittance will change considerably to account for the single obscure particle. You therefore could encircle 95% or 99% of the particles to reduce this error, but it is more common to take the statistical area of the particles. The standard deviation for a set of values [2-2] is:

$$\sigma^2 = \frac{1}{N}\sum_{i=1}^{N}\left(x_i - \bar{x}\right)^2 = \left\langle x^2 \right\rangle - \left\langle x \right\rangle^2 \tag{2.1.1.4}$$

Which is the root mean square (rms) of those values. Thus the definition of the rms of emittance is [2-2]:

$$\varepsilon_{rms}{}^2 = \overline{x}^2 . \overline{x'}^2 - \left(\overline{xx'}\right)^2 \qquad (2.1.1.5)$$

Another emittance that is used often is called 4rms emittance, and it is defined as:

$$\varepsilon_{4rms} = 4 \times \varepsilon_{rms} \qquad (2.1.1.6)$$

There are other parameters that describe a particle beam. These are called the Twiss parameters. They are α, β and γ and they can give the geometrical shape of the beam in phase space.

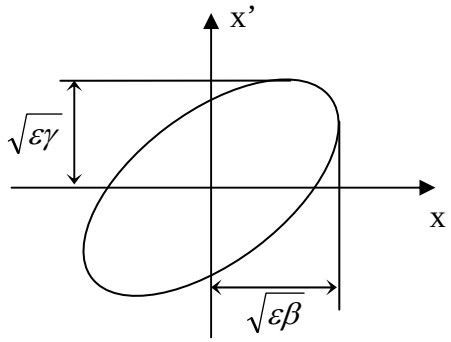

Figure 5: Parameters of a phase ellipse with area ε.

The equation with Twiss parameters for the phase ellipse is defined as [2-2]:

$$\gamma x^2 + 2\alpha x x' + \beta x'^2 = \varepsilon \qquad (2.1.1.7)$$

With comparison to equation (2.1.1.2), the parameters α, β and γ can be defined on Figure 5. From this, the parameter $\sqrt{\beta\varepsilon}$ represents the maximum beam envelope and so β is proportional to the beam envelope size. $\sqrt{\gamma\varepsilon}$ represents the maximum beam divergence, making γ proportional to the beam divergence. For ε_{4rms}, $\sqrt{\beta\varepsilon_{4rms}}$ represents the 2σ beam width, given from a Gaussian distribution.

It can be also shown [2-2] that:

$$\beta\gamma = 1 + \alpha^2 \qquad \alpha = -\frac{1}{2}\frac{\partial\beta}{\partial z} \qquad (2.1.1.8)$$

So α is proportional to the rate of change of the beam envelope size. Using the ellipse equation, it is possible to calculate the three Twiss parameters and the emittance from the phase ellipse.

Through a transport line where the particles stay at constant energy, the beam size and divergence may vary, but emittance stays constant, if non-linear forces (e.g. space charge) are not taken into account. However, when the energy of the particles is changed, as is the case in an accelerator, 4rms emittance is not invariant. Due to this it is common to define normalised emittance as [2-2]:

$$\varepsilon_N = \beta_{rel}\gamma_{rel}\varepsilon_{4\text{rms}} \qquad (2.1.1.9)$$

This allows emittance to be conserved during acceleration. Notice that in this case, β_{rel} and γ_{rel} are the relativistic quantities where $\beta_{rel} = v/c$ and $\gamma_{rel} = 1/\sqrt{1-\beta_{rel}^2}$, and shouldn't be confused with the Twiss parameters.

2.1.2: Measurement of Emittance

From the definition of emittance above, one can see that the parameters to be measured are the transverse position and the transverse momentum. A method to measure emittance uses slits and a screen, which is what was used for the measurements in chapter 4, see Figure 6.

The beam is incident onto a metal plate with small holes on it, called a pepper pot. When the beam passes through the plate, the transverse particle positions are defined (the positions of the holes) and so are known. Down-stream of the pepper pot there is a screen, which is

sensitive to the beam. This might consist of a glass plate with a layer of phosphor-47, which emits visible radiation when a particle hits it. From this it is possible to again measure the transverse particle positions, using a CCD camera to photograph the emitted photons. The change in position between the plate and screen shows the transverse velocity and therefore the transverse momentum can be calculated.

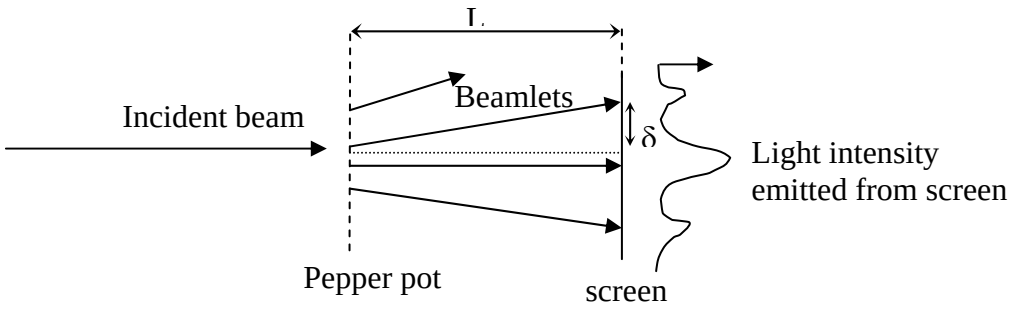

Figure 6: Drawing showing the components of measuring emittance.

This is a simple way to measure emittance, but has some disadvantages. It destroys the beam, and assumes the transverse momentum of the particle is constant between the pepper pot and screen (i.e. no space charge –the inter-particle interactions). It is a suitable method for the measurements in Chapter 4, because it only requires one shot to get a measurement, and so can show shot-to-shot instabilities of the beam.

Most emittance devices measure the transverse profile. SEM grids or wire scanners can be used for this purpose, with minimal disturbance to the beam. At Figure 5 it was stated that $\sqrt{\beta\varepsilon}$ represents the 2σ beam width. So if the beam width is measured as a function of a parameter which is connected to β and ε, it is possible to calculate the Twiss parameters and Emittance. This method has been used in Chapter 6, and is described there in further detail.

2.1.3: Matrix representation of the beam

For particle simulations, a good way to describe the beam dynamics is by using matrix representation. Imagine a part of the beam line is a solenoid and a quadrupole, separated by a gap. A diagram of this is shown in Figure 7. Both the beam and the beam line can be formulated with matrices, namely a σ matrix and an R matrix.

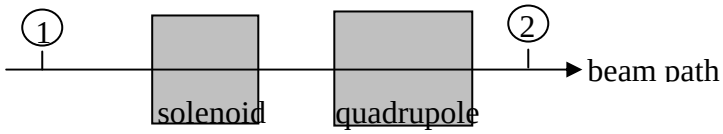

Figure 7: The example beam line.

So from point 1 to point 2 the beam passes through five elements; three drift spaces, a solenoid and a quadrupole. The matrix representation of this beam line is given as [2-4]:

$$\sigma_2 = R\sigma_1 R^T \qquad (2.1.3.1)$$

Where σ_n is the sigma matrix of the beam at the point n along the beam path, and R is the total transfer matrix between the two points, which is related only to the beam-line elements.

The sigma matrix consists of items from the beam phase ellipse.

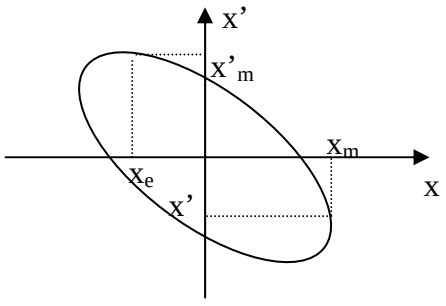

Figure 8: The phase ellipse, now with different notation.

The whole sigma matrix represents the geometric properties of the beam and so has a size of 6 x 6, two rows and two columns for each of the phase space planes. The leading diagonal shows the square of the maximal extend of the phase ellipse in each of the six directions, and the off-diagonal elements give the product of the extents between two directions [2-4], which can be seen in equation (2.1.3.3).

To simplify things it is possible to separate each phase plane into sub-matrices to give the total sigma matrix to be:

$$\sigma_n = \begin{pmatrix} \sigma_{xx} & \sigma_{xy} & \sigma_{xz} \\ \sigma_{yx} & \sigma_{yy} & \sigma_{yz} \\ \sigma_{zx} & \sigma_{zy} & \sigma_{zz} \end{pmatrix} \tag{2.1.3.2}$$

Here is the symbol form for the x-plane sub-matrix, with the notations from Figure 8.

$$\sigma_{xx} = \begin{pmatrix} {x_m}^2 & x_e x'_m \\ x'_e x_m & (x'_m)^2 \end{pmatrix} \tag{2.1.3.3}$$

This can be related to the Twiss parameters [2-4],

$$\sigma_{xx} = \begin{pmatrix} \beta_x \varepsilon_x & -\alpha_x \varepsilon_x \\ -\alpha_x \varepsilon_x & \gamma_x \varepsilon_x \end{pmatrix} \tag{2.1.3.4}$$

Which allows us to relate the sigma matrix with the phase ellipse at any point.

The transfer matrix has a similar structure to the sigma matrix. It is also simplified as in (2.1.3.2). Hence if there are no cross-terms in the transfer matrix, the planes can be calculated separately using just 2 by 2 matrices into equation (2.1.3.1). Each element in the beam line has a separate transfer matrix, and the relevant matrices are given in the beam optics section. To create the overall transfer matrix, each element matrix is multiplied in reverse n^{th} order. For example, for the 5 elements:

$$R = R_5 \cdot R_4 \cdot \ldots \cdot R_1 \tag{2.1.3.5}$$

2.1.4: Magnetic Rigidity

When a particle of velocity **v** and charge q travels in the presence of a magnetic field **B**, it moves in a circle with radius ρ, which is formed when equating the Lorentz force and the centripetal force for an object moving in circular motion:

$$\rho = \frac{mv}{Bq} \tag{2.1.4.1}$$

This is why the charge to mass ration is important. However, it is more useful to define the magnetic rigidity, the field multiplied the radius, which is also the ratio of momentum per charge, of the particle.

$$B\rho = \frac{mv}{q} \equiv \frac{\sqrt{\left[2V_o\left(\frac{mc^2}{q}\right)\right]}}{c} \tag{2.1.4.2}$$

Where V_o is the extraction voltage and c is the speed of light [2-5]. This is a useful quantity because it allows the calculation of the change in angle of a particle:

$$\theta = \frac{L}{\rho} = \frac{BL}{B\rho} \tag{2.1.4.3}$$

Where L is the effective length of the element.

2.2: Beam Optics

As a beam travels down its path, the items that affect its trajectory are part of the optics of the beam. This section describes some of those items. In the magnetic field diagrams, the blue section with a cross is the coils, and the red outline is the iron core. For the transfer matrices,

the longitudinal (z) plane is not included, as this does not affect the other two planes for these elements, and space charge has been assumed to be negligible.

2.2.1: Drift Space

A drift space is a length of the beam line where no magnetic field is present and so there is no external force on the particles. The transfer matrix for a drift space of length L is:

$$R_{drift} = \begin{pmatrix} 1 & L & & 0 \\ 0 & 1 & & \\ & & 1 & L \\ & 0 & 0 & 1 \end{pmatrix} \qquad (2.2.1.1)$$

2.2.2: Dipoles (Bending and Steering Magnets)

In a bending magnet, which an example is shown in Figure 9, it can be seen that the direction of the magnetic field is vertical, and hence the force is horizontal. The charged particles are pulled in one way in the horizontal plane, creating a bend. It is preferred that the magnetic field be as uniform as possible, so minimising focusing or defocusing effects.

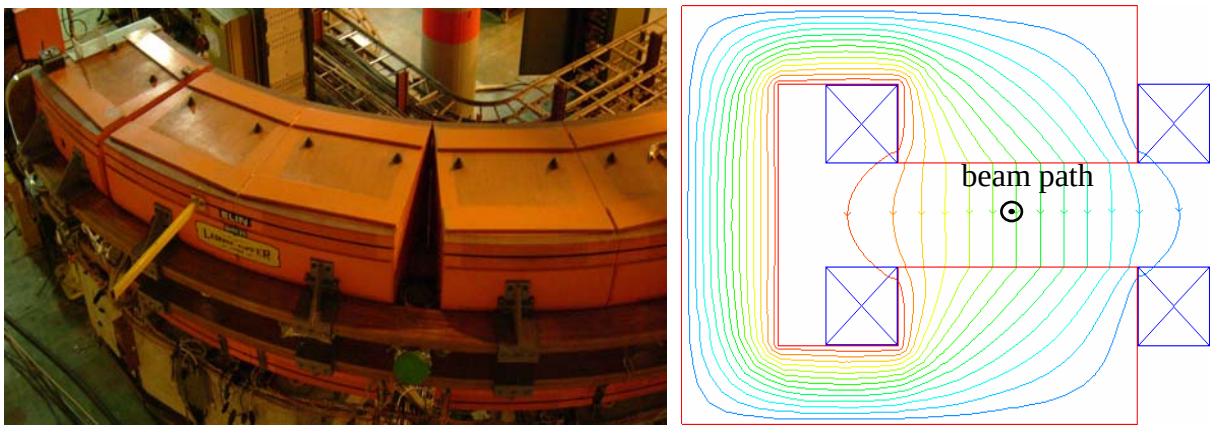

Figure 9: Photo of a bending magnet, and a cross-section showing magnetic flux lines.

The transfer matrix of a bending magnet is not used in this report, but details can be found in [2-4].

2.2.3: Solenoids

A solenoid is a relatively simple magnetic lens, which is placed in a beam line to focus or defocus the beam. It consists of wire, coiled and surrounded by an iron yoke [2-2], this is shown in Figure 10. The magnetic field lines are also shown, and this shows that if a charge was travelling down the centre line, there would be no change of direction. However, if a charge has a transverse position away from the centre axis, the radial component of the magnetic field causes the particle to obtain a transverse component of momentum, which then couples to the longitudinal field to focus the particle towards the solenoid axis [2-6]. This creates a focal point after the solenoid. Unlike an optical lens, the image is rotated at the focal point [2-2]. This means that the two transverse directions affect each other, and so they are coupled.

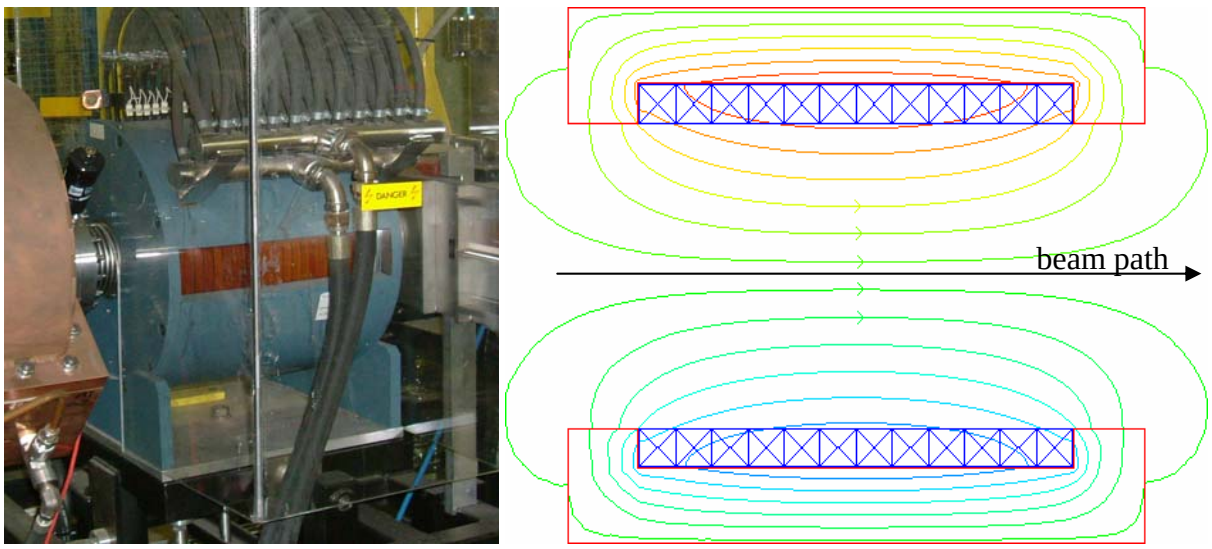

Figure 10: Solenoid ITL.SOL02, and also magnetic flux lines within a typical solenoid.

The transfer matrix in the x and y planes for a solenoid is [2-4]:

$$R_{sol} = \begin{pmatrix} C^2 & \frac{SC}{k} & SC & \frac{S^2}{k} \\ -kSC & C^2 & -kS^2 & SC \\ -SC & -\frac{S^2}{k} & C^2 & \frac{SC}{k} \\ kS^2 & SC & -kSC & C^2 \end{pmatrix} \qquad (2.2.3.1)$$

Where L is the effective length, and;

$$k = \frac{B}{2B\rho} \qquad C = \cos(kL) \qquad S = \sin(kL) \qquad (2.2.3.2)$$

This is consistent that the two planes are coupled by the non-zero cross terms.

2.2.4: Quadrupoles

Quadrupoles are also used to focus particle beams, and they are more effective than solenoids at higher energies [2-2]. They can also be used to match the beam parameters to components further along the beam pipe. The arrangement of the magnetic field is very different from a solenoid, as shown in Figure 11. Because of this magnetic field arrangement, quadrupoles only focus in one transverse direction, either the x or y plane, and defocus in the other. Therefore in most cases it is required that three quadrupoles are put together to make a triplet, to match the beam in all planes.

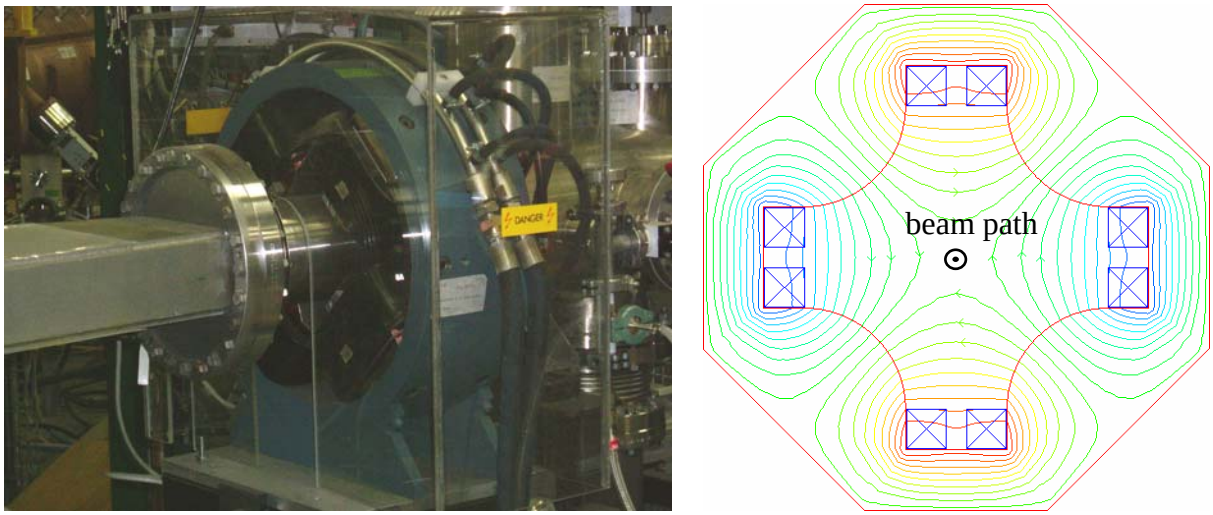

Figure 11: Quadrupole ITL.QDN01, and a cross section showing the magnetic flux lines.

In a quadrupole, the x and y planes are not coupled, and this can be confirmed in the transfer matrix by the zero cross terms:

$$R_{quad} = \begin{pmatrix} F \text{ or } D & 0 \\ 0 & D \text{ or } F \end{pmatrix} \qquad (2.2.4.1)$$

$$F = \begin{pmatrix} C & \frac{S}{k} \\ -kS & C \end{pmatrix} \qquad D = \begin{pmatrix} Ch & \frac{Sh}{k} \\ -kSh & Ch \end{pmatrix} \qquad (2.2.4.2)$$

$$k = \left[\left| \frac{B}{B\rho} \right| \right]^{\frac{1}{2}} \qquad (2.2.4.3)$$

C and S are the same as in the solenoid, and Sh and Ch are the hyperbolic functions. In the diagonal elements either a plane is focusing (F sub-matrix), or defocusing (D sub-matrix), and they must be opposite. The orientation of the transfer matrix is determined by the sign of $B/B\rho$ (R_{xx}=F and R_{yy}=D if positive).

2.3: Beam Diagnostics

2.3.1: The Faraday Cup

The faraday cup is a reliable device to measure the electrical current of the beam. This is achieved by using a beam trap in the shape of a cup, which is electrically connected to an oscilloscope. This method is destructive, so the beam is lost and hence is not suitable for circular accelerators or beams that are required for collisions.

Above certain particle energies, secondary electrons are produced during contact with the walls of the beam trap. To stop these electrons escaping the trap, which increases the measured current, a negative electrode is placed at the front of the trap. This also means that the Faraday cup is only used to measure the current of low energy beams [2-7].

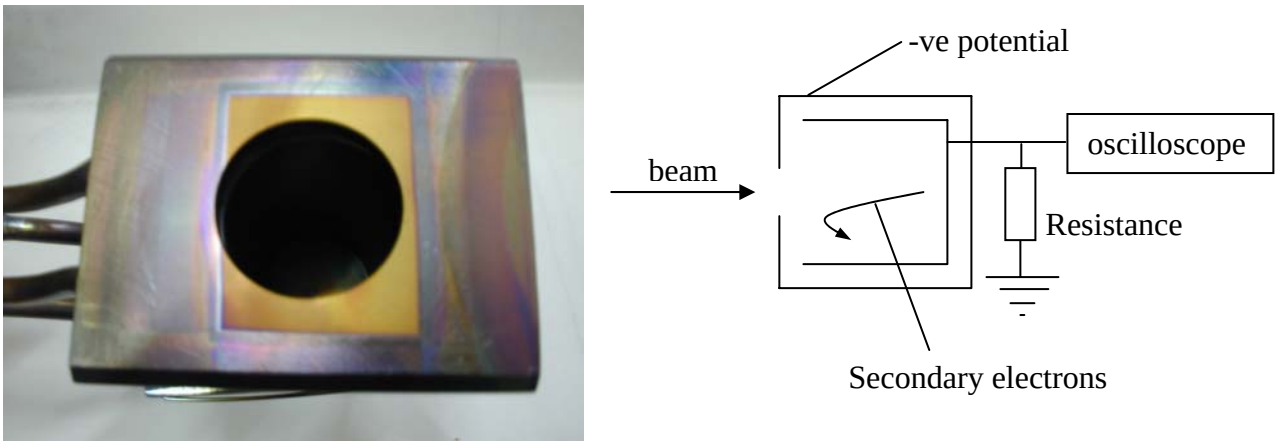

Figure 12: Photo of ITL.MFC01, and a diagram of a faraday cup.

2.3.2: The Beam Current Transformer

The Beam Current transformer is another method to measure the electrical current of the beam, and the main advantage is its non-intrusive nature. It consists of a ring shaped iron core, placed around the beam [2-7], and a wire coiled around it. This arrangement acts as a transformer, where the beam is the primary windings and the inductive coil is the second winding. Therefore the output voltage can be calibrated to become proportional to the current of the beam.

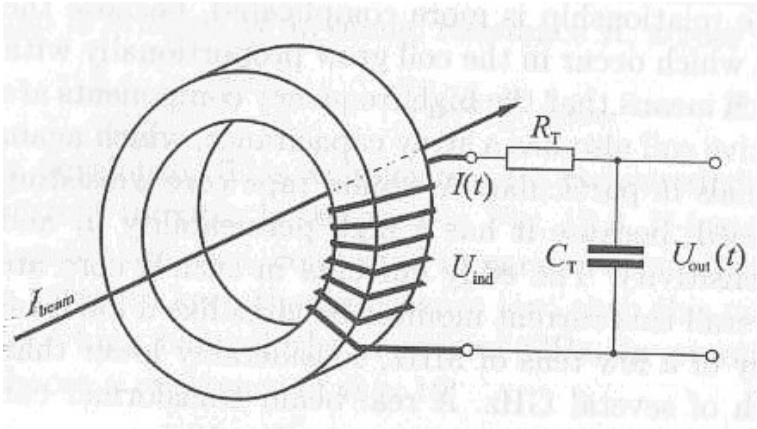

Figure 13: Core and simplified circuit for a beam current transformer [2-7].

2.3.3: The Secondary Emission Monitor (SEM) grid

When a particle with a certain amount of energy hits a solid, it is able to knock electrons off that solid. This is called secondary emission. A SEM grid consists of a number of thin wires placed evenly across the beam. When the beam particles knock off electrons, it is possible to measure the charge depletion in each of the wires, and this is proportional to the density of the beam. From this it is possible to form a transverse density profile of the beam.

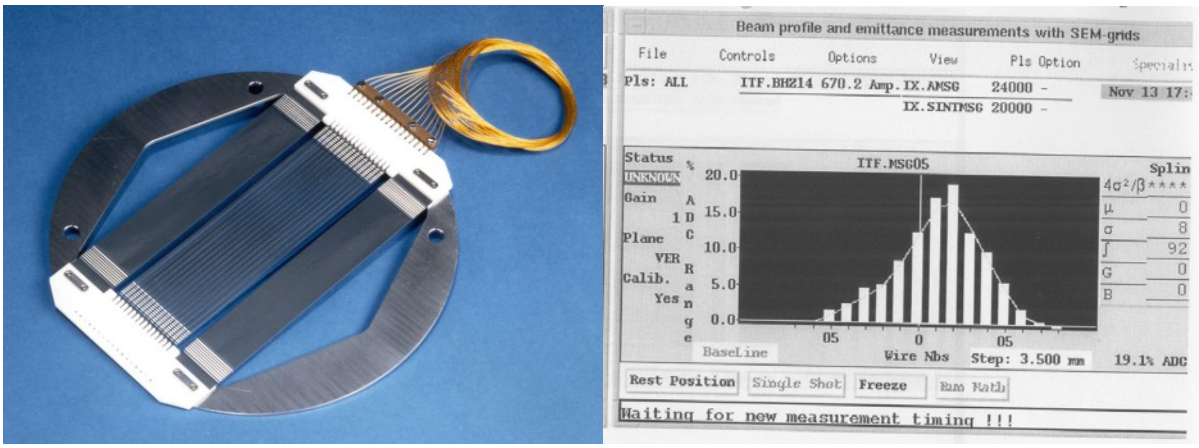

Figure 14: A photo of a SEM grid, and a typical readout.

Chapter 3: Experimental Apparatus

3.1: The Laser Ion Source

An option for the LHC lead injection Chain is the LIS route. This source can produce a high intensity, short pulse heavy ion beam, which is ideal for single turn injection into synchrotrons. This source is still in the research and development stage, and the aim of the study is to create a source that is capable of reliably meeting the LHC injector chain requirements in emittance and intensity.

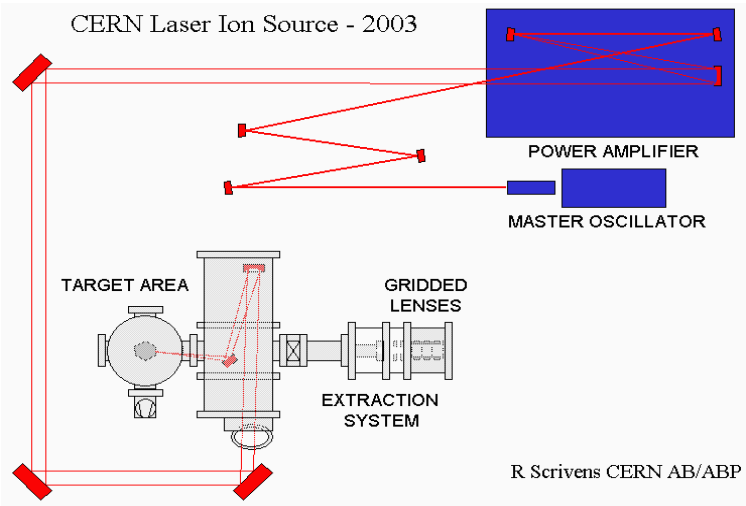

Figure 15: Scheme of the Laser Ion Source with new 100J CO_2 laser.

In 2002, a new CO_2 laser system was installed into the Faraday cage of building 363 at CERN. The ITEP (Institute of Theoretical and Experimental Physics) and TRINITI (Troitsk Institute for Innovation and Fusion Research) constructed laser, consists of a Master Oscillator and Power Amplifier (MO-PA) laser chain to produce laser pulses at 1Hz, up to 100J in a pulse length of 25ns, at a wavelength of 10.6μm.

This beam is then transported to the source area and focused onto a solid metal target. When the laser beam hits the surface of the metal, some of the energy of the laser radiation is absorbed, causing localised heating and leading to evaporation. This evaporation of the metal target allows the lead plasma to be formed, when the absorption of laser frequency at the surface is similar to the plasma density [3-1]. The plasma contains high charge-state ions and electrons, and these ions must then be extracted to form the ion beam. The maximum intensity charge state of the LIS ion beam is Pb^{27+}. For more information on the LIS, refer to [3-2].

The emittance measurements in Chapter 4 are taken after the extraction electrodes, and so is the emittance of all the charge states within the beam.

The rest of the injection chain to LHC has not been built, but the scheme has been envisaged. After extraction the beam would be transported and matched (using a solenoid or gridded lens apparatus) to a Radio Frequency Quadrupole (RFQ). Then after this, a switchyard would form the MEBT (Medium Energy Beam Transport line), which would transport the beam to the existing Linac. Then after acceleration through Linac 3, it would be directly injected into the PS booster, which would also need upgrading, and from then, on the usual accelerator chain at CERN (PS, SPS, LHC) would be used.

3.2: The CERN heavy ion facility, Linac 3

The experiments in Chapter 5, Chapter 6 and Chapter 7 were performed using the CERN heavy ion facility, known as Linac 3. The layout is shown in Figure 16. The ion beam is created in the ECR source and is extracted to an energy of 2.5keV/u. The Low Energy Beam Transport line (LEBT) transports and matches the ions to the RFQ, and consists of a spectrometer to select a charge state. In the RFQ the particles are bunched and accelerated to

250keV/u. Then the MEBT focuses and matches the beam to the other accelerating IH tanks, IA1, IA2 and IA3. After the final tank, where the ions now have energy of 4.2MeV/u, there is a stripper, which increases the charge state of the beam. The stripper produces many different charge states and so the ITF line has another spectrometer to single out the charged particles that are needed, which are Pb^{53+}. The beam then passes down transfer lines towards the PSB. The next few sections of this report provide greater detail of areas that have most significance for the measurements completed here.

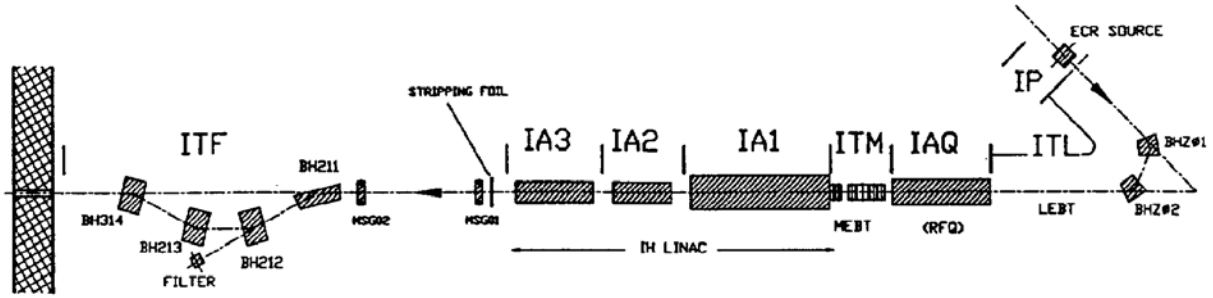

Figure 16: The layout of Linac 3, showing the names of the different sections.

3.2.1: Naming conventions on Linac 3

Throughout this report, the magnetic components and diagnostic equipment are named using the convention applied on Linac 3:

Section.Abbreviation and Number (3.2.1.1)

With each element having an abbreviation as shown in Table 1.

Element Name	Abbreviation
Bending Magnet	BHZ
Quadrupole (Defocusing in horizontal plane)	QDN
Quadrupole (Focusing in horizontal plane)	QFN
Solenoid	SOL
Faraday Cup	MFC
Spectrometer Slits (horizontal and vertical)	SL (HV)
Secondary Emission Grids (horizontal and vertical)	MSG (HV)

Table 1: Abbreviations of elements on Linac 3.

The number in the name is the nth item of that element within the section. From this, the first quadrupole in the LEBT, or ITL, is named ITL.QDN01.

3.2.2: The Electron Cyclotron Resonance Ion Source

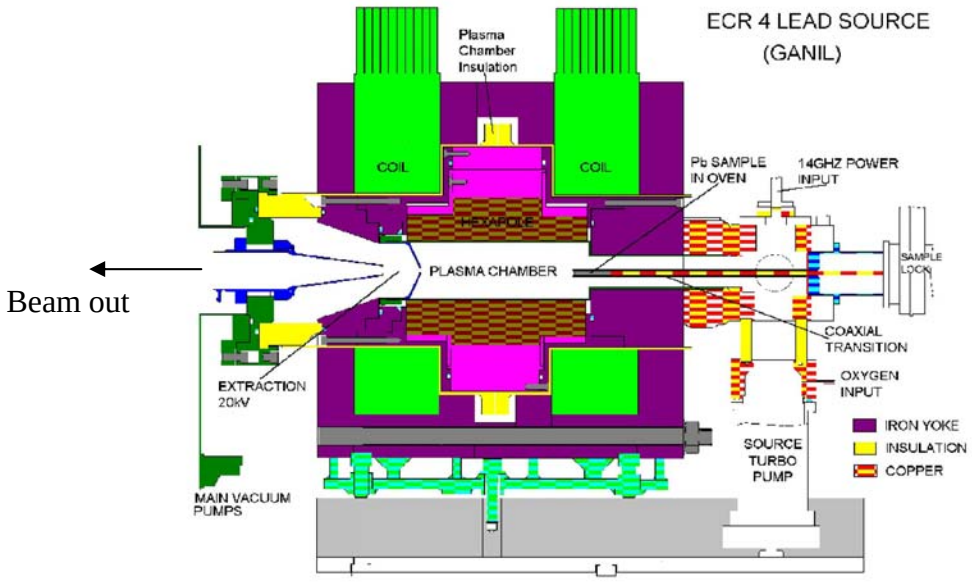

Figure 17: A schematic layout of the ECR source in Linac 3.

The Electron Cyclotron Resonance (ECR) source is a plasma generator, and Figure 17 shows the layout of the central region of the source. The plasma is generated inside the tank within

the iron core, and is confined in an open magnetic trap. The two solenoid coils provide the longitudinal confinement, and radially the plasma is confined by the Fe-Nd-B hexapole. The plasma is created by microwave RF frequency waves, and the ion beam is extracted at 20kV with a frequency of 10Hz.

The ECR source increases the charge states of the particles in the plasma by using a multi-step electron impact ionisation process [3-3], as given in equation (3.2.1). This ionisation can occur when an electron collides with an ion. The electron energy must be at least as high as the required ionisation potential.

$$e^- + A^{k+} \Rightarrow e^- + A^{(k+1)+} + e^- \qquad (3.2.2.1)$$

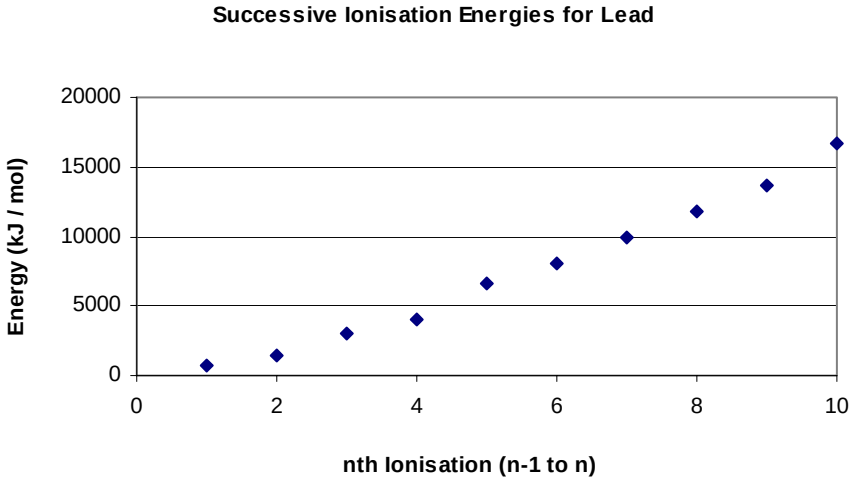

Figure 18: A graph showing the energy required for each successive ionisation [3-7].

Figure 18 shows that is takes more energy to remove each electron as the charge state increases. Therefore, one of the parameters that govern the highest charge state achievable is the energy distribution of the electrons in the plasma. This means to get the high charge states, the source requires a way to increase the energy of the electrons. In an ECR source this

is done by using the electron cyclotron resonance condition, hence the name of the source. When micro-waves and a magnetic field occupy the same volume, there is a surface where the micro-wave frequency ω_c and the magnetic field B corresponds to the resonance condition [3-4]:

$$\omega_c = \left(\frac{e}{m}\right) \times B \qquad (3.2.2.2)$$

Where e and m are the charge and mass of an electron respectively. When electrons cross this surface, they gain energy, creating the high-energy electrons for ionisation.

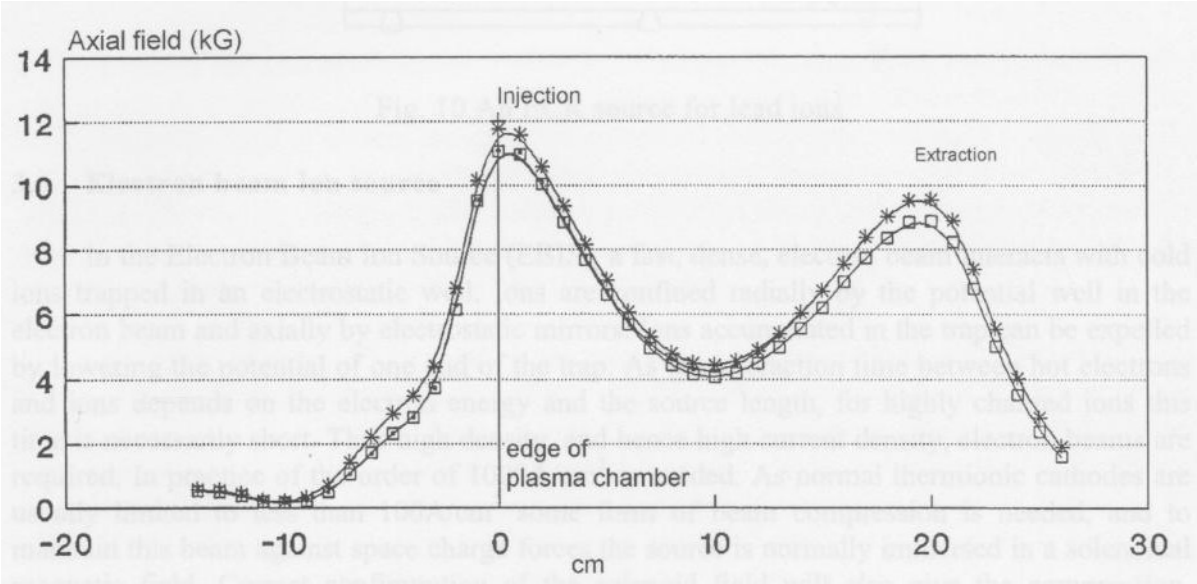

Figure 19: The longitudinal magnetic field in the plasma chamber [3-8].

We also require that the ions remain confined in the plasma long enough to undergo many collisions, necessary for the ionisation of many charge states. So a plasma that is stable and turbulence free is desired. The magnetic mirrors, which are solenoids, at each end of the chamber and the permanent hexapole stop any charged particles escaping. The longitudinal magnetic field in the trap is shown in Figure 19. Only particles that have a small solid angle

along the trap axis can break free. When two charged particles collide, the Coulomb force between them can alter their direction and this Coulomb scattering allows a steady stream of particles to exit the trap.

The confinement time for ions and electrons are given in (3.2.2.3) and (3.2.2.4) respectively [3-5].

$$\tau_i = Rl\sqrt{\pi AM/(2T_i)}\exp(iU/T_i) \qquad (3.2.2.3)$$

Where R is the mirror ratio (B_{max} / B_{min}), A is the atomic mass number, M is nucleon rest mass, l is the effective source length, i is the charge state and U is the electric plasma potential. Although this equation is not used in this report, it is interesting to see what determines the efficiency of the ECR source.

$$\tau_e = 1.48*\left(\ln R + \sqrt{\ln R}\right)/\ \nu_e \qquad (3.2.2.4)$$

Where ν_e is the frequency of electron collisions in the plasma, and this is related to electron temperature by [3-3]:

$$\nu_e \propto \frac{1}{\sqrt{T_e^{\ 3}}} \qquad (3.2.2.5)$$

From (3.2.2.3), it is shown that the higher charge states have a longer confinement time, due to the charge state, "i", term in the exponential. Therefore, the average charge state is higher inside the plasma, than the ions that are being extracted [3-5]. It would be desirable to release all of these higher charged ions into the beam. This is possible by reducing the confinement conditions on the plasma. One way to do this is to rapidly remove one of the magnetic

mirrors, allowing all the particles in the trap to escape in one given direction. The method that is used in the ECR source at CERN is called the afterglow method. After a certain time, the RF waves that heat the electrons are switched off. As the electrons cool down, their confinement time drops rapidly, shown by combining (3.2.2.4) and (3.2.2.5), and so they escape in abundance. The plasma must remain charge neutral [3-6], so the high charged ions follow, creating a pulse of the particles contained in the trap. In this way, ECR sources that operate in an afterglow mode will generally produce more intense and higher charge beams than those sources that operate in the continuous mode.

To further the confinement time, a light (compared to the extracted ions) gas is injected into the working region of the plasma. This is to decrease the temperature of the heavy ions [3-5]. At lower temperature the ions have a longer confinement time, from the equation (3.2.2.3), and so more electron collisions occur, to give a higher mean charge state. For the ECR source at CERN the gas injected is oxygen. One problem with this gas is that the charge states Pb^{26+} and O^{2+} have the same charge to mass ratio. This means the two ions cannot be separated using a magnetic spectrometer as used on Linac 3.

3.2.3: The Low Energy Beam Transport Line (LEBT)

The objectives of the LEBT are to transport the beam from the source to the RFQ, separate the charge states, while matching the beam dynamics to those required by the RFQ. Figure 20 shows the layout of the LEBT, with all the element labels. There are three main sections to the LEBT; the first solenoid focuses the beam at the object point of the spectrometer, the quadrupole keeps the beam at a constant vertical beam width during the path along the bending magnets, then there is the spectrometer, which selects a single charge state from the

beam. The quadrupole triplet and second solenoid are in charge of matching the beam to the RFQ.

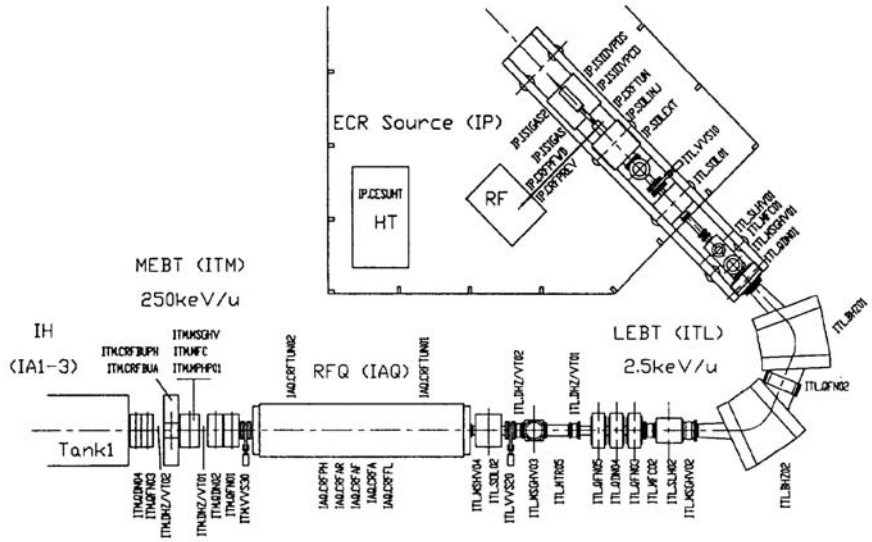

Figure 20: A view of the Source, LEBT and MEBT, showing the names of each element.

Chapter 4: Emittance Measurements of the CERN Laser Ion Source

4.1: Introduction

In this chapter, emittance measurements using a pepper pot and a digital CCD camera, of the LIS are presented and an analysis of the data has been carried out. It has been found that the emittance of the source is 140mm.mrad un-normalised and 0.8mm.mrad normalised. This was completed with the parameters given in Table 2.

Distance of Target to Extraction	1.76 m
Apertures of Extraction Electrodes	24.4 / 28 / 28 mm
Potential of Extraction / Puller Electrodes	100 / -10 kV
Element	208-Pb
Maximum Intensity Charge State	27+
Range of Charge States (above 0.1% of total current)	19+ to 32+
Ion Pulse Length (for 27+)	3.5 μs
Ion Average current, peak current	22 mA, 57 mA
Distance of Extraction to Emittance Device	140 mm
Wavelength of Laser	10.6 μm
Pulse length of Laser	28 ns
Laser Energy	90 – 105 J
Theoretical Laser Spot Diameter	0.1 mm
Theoretical Laser Power Density	3.6×10^{13} W m^{-2}

Table 2: Parameters of the emittance measurements [4-1].

4.2: The emittance device

The apparatus consisted of the LIS system (Figure 15), but with the gridded lenses removed. The pepper pot was placed at a distance from the extraction electrodes of 140mm [4-1]. The support for the emittance device could be raised or lowered so that either a faraday cup or the pepper pot was incident onto the beam, this was to make sure the laser was stable before putting the emittance device into the beam, and this is shown in Figure 21. The pepper pot consisted of 169 holes with nominal diameter 0.2mm, which were arranged into a 5mm

spacing square grid of 13 by 13 rows. The distance from pepper pot to viewing screen was L=79.3mm±1.3mm.

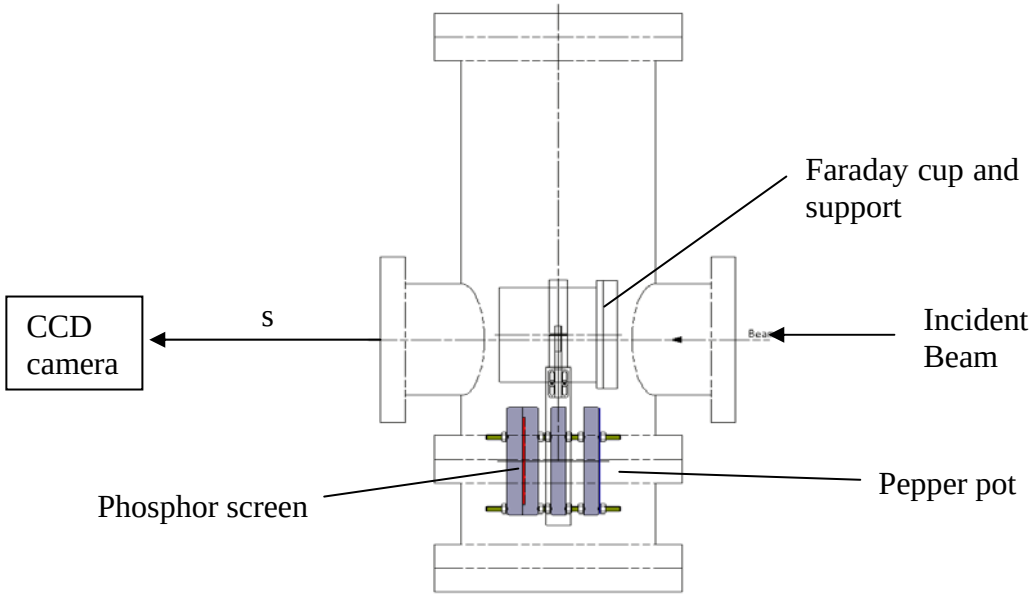

Figure 21: Diagram of apparatus used in the experiment (here the faraday cup is incident on the beam)

The distance "s" is the length between the back of the screen and the lens of the CCD camera. Previous tests were completed to find the pixels per mm of the camera at different distances [4-2], and for the measurements, a distance of 1.9m, which gives a value of 7.53pixels/mm. This was also confirmed by placing a test pattern on the back of the screen. This pattern and the corresponding picture are shown in Figure 22. This was also very useful in focusing the camera on the back of the screen. Between the camera and the emittance device, black paper was wrapped around to form a tube, stopping light from the room producing too much background noise.

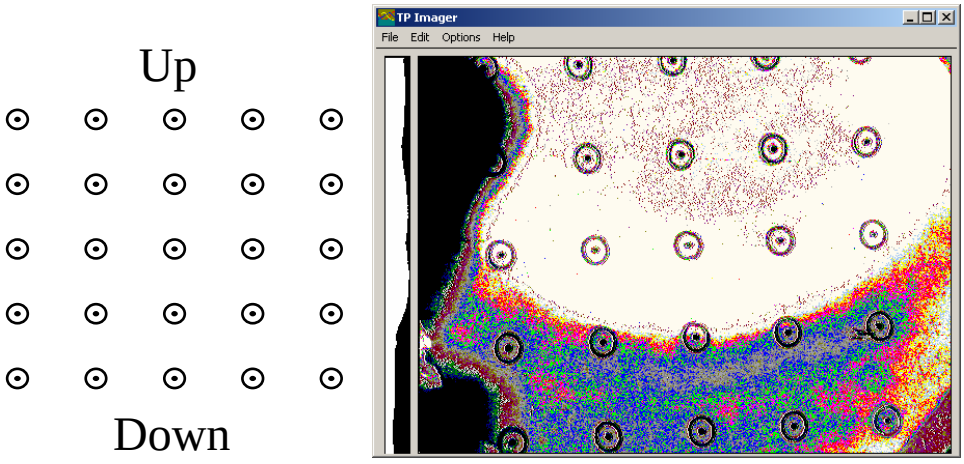

Figure 22: The test pattern (not actual size), and how it looked through the CCD camera.

4.3: Method

The source was put at high voltage (100kV and –10kV on the puller electrode) and was kept at this voltage for a few hours to stabilise. This was to reduce the chance of a breakdown in the extraction electrodes. This sometimes created a large noise pulse in the electronics in the area (e.g. the vacuum pumps), which could damage them. The CCD camera is particularly sensitive to noise and any breakdowns during the operation of the camera could damage it. Once the source was stable, the camera was switched on, and the CCD allowed to cool down. The camera has an external trigger input and so it is possible to take the picture in different time intervals. 30 images could be taken during a 30 minute run of the laser. Laser regenerator problems restricted operation to 30 minutes per day.

After the pictures were taken, analysis was started to calculate the emittance. Here is a short description of the procedure, for a further view of each section, see the data analysis section. Each picture was loaded into the TP imager program, which displays the picture (examples can be seen in Figure 22 and Figure 26). This program was used to calculate a horizontal

integral of the picture as shown in Figure 23. Additionally, it can subtract background noise and rotate the images.

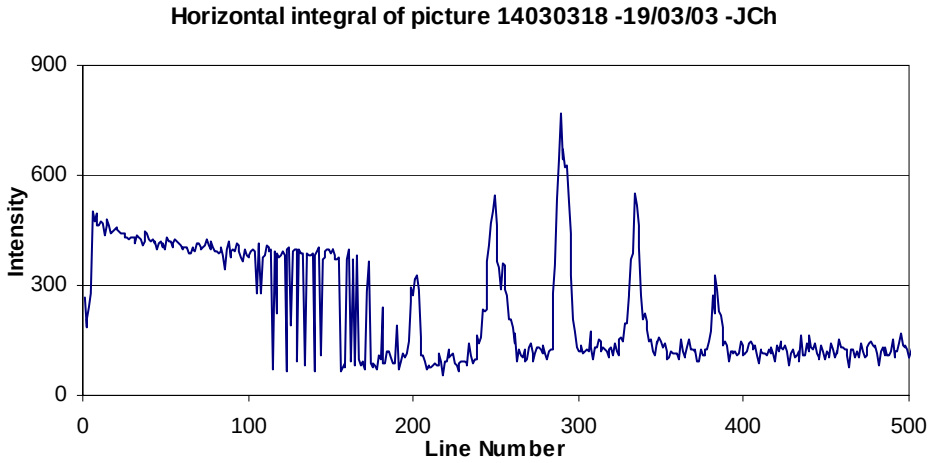

Figure 23: Example of a horizontal integral (file 14030318).

This profile was then placed into the Peak Assistant program. To reduce any non-linear noise, the baseline can be corrected in this program, using a parabolic curve subtracted from the profile. The signal can also be zeroed between the peaks. The peak ranges and profile was then copied and pasted into the excel spreadsheet "base30.xls". This spreadsheet calculates the total and 4rms emittance, draws phase diagrams for that profile and also gives the α, β and γ values for the phase ellipse.

4.4: Results

The emittance data was taken on two days in March 2003. On the 12th, the main aim was to test the system response to various parameters of the camera and pepper pot. Table 3 shows the results of these measurements. For the camera settings, "ad" is a multiplying factor similar to the gain, "Int G" is the internal gain factor, "Int t" is the time interval between the

ions being produced and the opening time of the camera shutter, and "Trig Δ" is the length of time the shutter is open.

Camera Settings ad / Int G / Int t /Trig Δ	**average ε_{4rms}**	**stand dev**	**stand dev %**
x2 /200 / 3μs / 4μs	149.96	55.12	36.8%
x2 / 220 / 3μs / 4μs	194.68	94.34	48.5%
x2 / 180 / 3μs / 4μs	162.80	76.40	46.9%
x2 / 220 / 3μs / 4μs (pepper pot 1kV)	173.49	40.15	23.1%
x2 / 220 / 3μs / 20μs (pepper pot 1kV)	222.36	37.51	16.9%

Table 3: Results of the emittance measurements on the 12th of March.

It was decided to trigger the camera with gain 200 at 3μs for an interval of 4μs, with a pepper pot biasing of +0.6kV for the measurements taken on the 14th. This was due to the signal to noise ratio being the greatest, and this is the time we expect Pb^{27+} ions. Table 4 shows the result of the second set of emittance measurements. The result is taken after the pictures had been rotated, and all noise reduction algorithms (with similar parameters) completed. This gives the value of the un-normalised 4rms emittance to be 140mm.mrad, with the standard deviation of the results being 20mm.mrad. An example of the phase plots produced by the emittance calculation routine is shown in Figure 24. Using equation 2.2.1.9, and given that the $\beta_{rel}\gamma_{rel}$ value (the relativistic variables) is 5.5×10^{-3}, the normalised 4rms emittance is calculated to be 0.8mm.mrad, for the maximum intensity charge state, Pb^{27+}. Other important laser and source parameters are given in Table 2.

filename	Rotation (°)	ε 4rms=	total ε=	α=	β=	γ=	<ε 4rms> (mm.mrad) σε (mm.mrad) σε / <ε 4rms> %
14030312	-2	115.5	250.5	-0.317	0.166	6.643	
14030313	-2	152.0	309.2	-1.689	0.743	5.190	
14030314	-2	160.0	346.5	-2.474	0.895	7.954	
14030315	-2	175.0	367.8	-0.747	0.286	5.447	
14030316	-2	130.6	285.2	-0.481	0.301	4.088	**142.6**
14030317	-2	118.3	266.5	-0.275	0.194	5.536	23.7
14030318	-2	143.9	274.5	-1.685	0.748	5.132	*16.6%*
14030319	-2	136.7	242.5	-1.633	0.684	5.359	
14030320	-2	110.8	226.6	-0.516	0.309	4.090	
14030321	-2	183.1	373.1	-1.884	0.692	6.577	

Table 4: Results of the emittance measurements on the 14th of March.

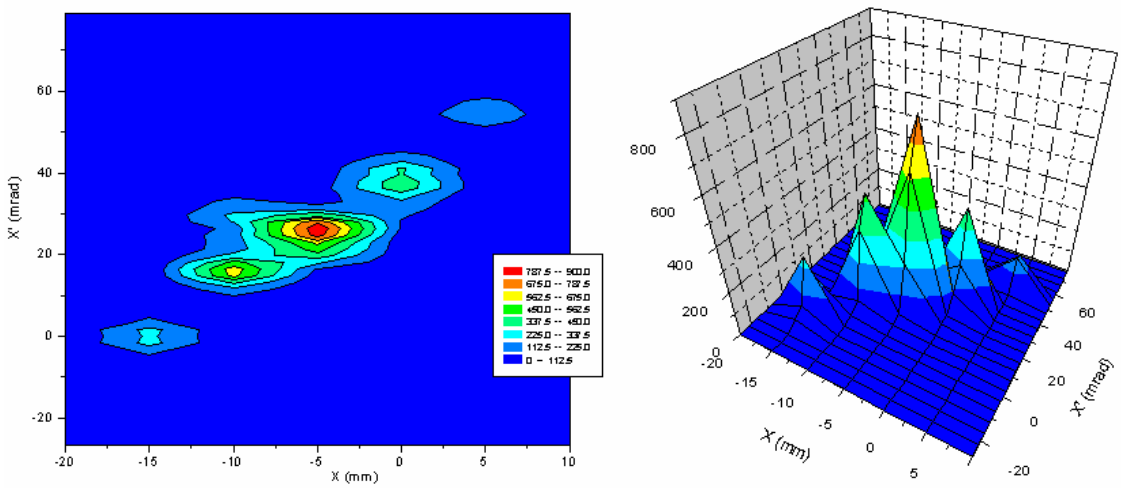

Figure 24: Example of the phase plots graphs (file 14030318).

A series of phase-space ellipses were calculated using this data and they can be seen in Figure 25. This shows that the measured emittance is not stable from shot-to-shot. The source does not have good ion current stability and so it is thought that this could be linked [4-3]. A preliminary test was completed to find if the ion current and emittance were correlated, but there were no clear results, and so more accurate measurements are required.

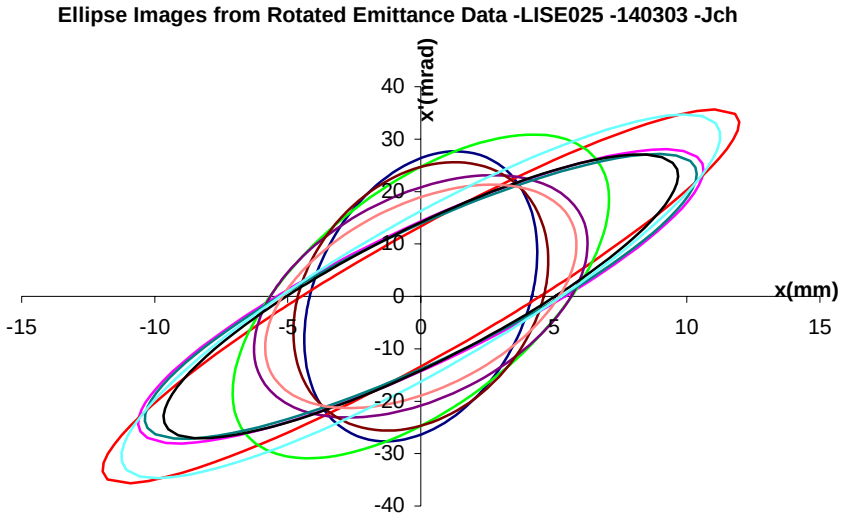

Figure 25: Phase ellipses for the emittance results.

4.5: Data Analysis

4.5.1: Rotation of the Pepper Pot

When the pictures were loaded into the TP imager, it could be seen that the pepper pot was not aligned with the horizontal and vertical axis of the CCD camera. Figure 26 shows a sample image, with a horizontal line placed along a row of dots, to show the error in alignment more clearly. When taking a horizontal integral, the offset of the outer holes would give the effect of increasing the peak width, and hence this would give an emittance that was too high.

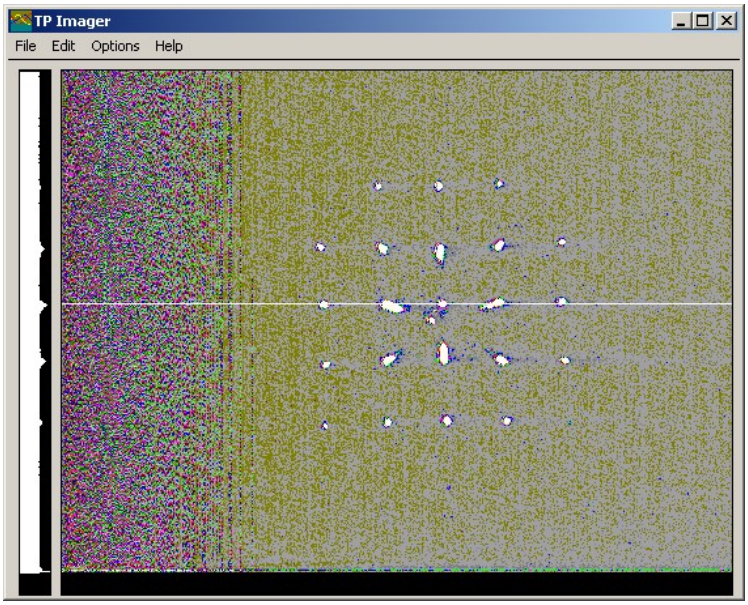

Figure 26: TP imager picture (file 14030313) showing the rotation of the pepper pot.

The angle that aligned the axis was determined by comparing the horizontal profile of the image at different angles. Each profile is an integration over the whole width of the picture, and so the area under each profile will remain constant. Hence the image was rotated until the integration gave the maximum peak intensity. The emittance was then calculated using the new angles of rotation, and compared to the original data.

filename	Rotation (°)	ε 4rms=	total ε=	α=	β=	γ=	<ε 4rms> (mm.mrad) σε (mm.mrad) σε / <ε 4rms> %
14030312	0	130.1	263.9	-0.360	0.170	6.646	
14030312	-2	115.5	250.5	-0.317	0.166	6.643	
14030313	0	215.1	429.1	-1.217	0.544	4.562	
14030313	-2	152.0	309.2	-1.689	0.743	5.190	For 0° **175.7**
14030314	0	209.9	391.8	-2.134	0.773	7.188	29.8
14030314	-2	160.0	346.5	-2.474	0.895	7.954	*17.0%*
14030315	0	194.4	359.8	-0.679	0.271	5.386	
14030315	-2	175.0	367.8	-0.747	0.286	5.447	
14030316	0	155.6	290.5	-0.480	0.267	4.605	
14030316	-2	130.6	285.2	-0.481	0.301	4.088	
14030317	0	137.7	253.2	-0.273	0.199	5.389	For -2° **142.6**
14030317	-2	118.3	266.5	-0.275	0.194	5.536	23.7 *16.6%*
14030318	0	185.2	319.8	-1.347	0.594	4.738	
14030318	-2	143.9	274.5	-1.685	0.748	5.132	
14030319	0	194.6	357.2	-1.259	0.516	5.014	
14030319	-2	136.7	242.5	-1.633	0.684	5.359	
14030320	0	141.7	282.5	-0.453	0.263	4.581	
14030320	-2	110.8	226.6	-0.516	0.309	4.090	
14030321	0	193.0	346.5	-1.759	0.654	6.254	
14030321	-2	183.1	373.1	-1.884	0.692	6.577	

Table 5: Summary of the emittance results before and after rotation.

As expected the emittance reduced when the images were correctly aligned. As shown in the table above, alignment was found when the images were rotated 2 degrees clockwise, and the average reduction of emittance from rotation was 19%.

4.5.2: Operator Dependant Noise Suppression

After the first measurements of emittance were analysed, it became clear that the existing noise reduction techniques were not adequate enough to reduce the background noise. The existing method was simply a constant level subtraction from the profile. It could be seen that the background level was not linear, and so the peak assistant program had to be modified to accommodate this.

Two algorithms have been made to reduce the noise level from the horizontal profile. The first is a parabolic fitting program which reduces the baseline to a linear level around zero. By selecting three points on the profile, a parabolic line can be drawn through these points. This function is then subtracted from the profile, which can be seen in Figure 27. However, this method relies heavily on the operator picking the correct points for fitting. If done incorrectly, this can cause major changes in the profile and give a very inaccurate value for the emittance. So, when this method has been done correctly, the baseline should be at zero the whole way across the profile.

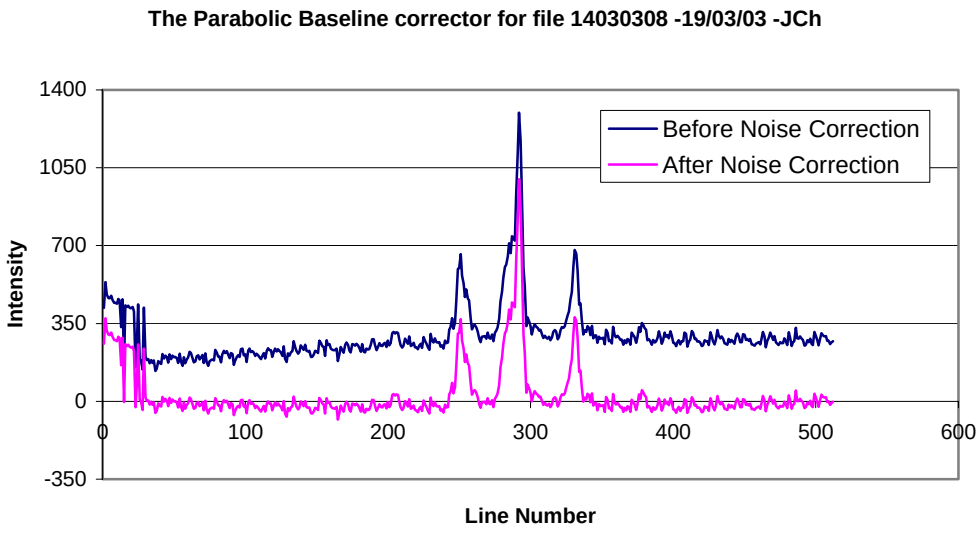

Figure 27: Before and after the parabolic noise reduction algorithm (file 14030308).

The second algorithm removes the entire signal that is not within a defined number of pixels from the peaks, with respect to a threshold level. Before this algorithm was created, the noise signal was manually set to zero in the excel spreadsheet, which was both time consuming and was inconsistent between different profiles.

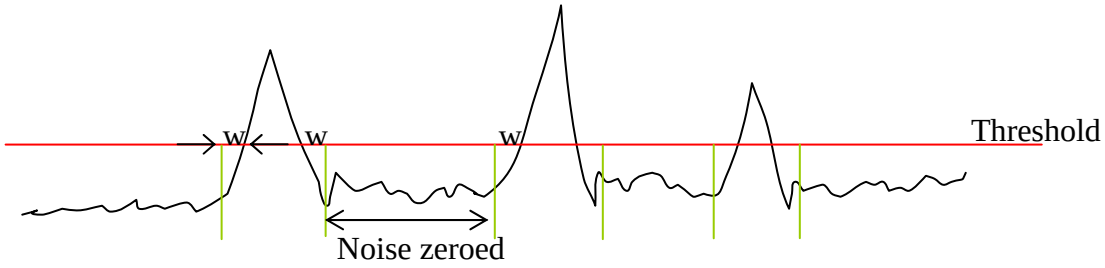

Figure 28: The width variable. All points outside the green lines are reduced to zero.

From Figure 28, it can be seen that the width variable, w, is a operator set number of pixels away from the point that the profile crosses the threshold level, which was set to 10% of the highest peak. All other values outside this area were set to zero. This allows the operator to delete all the noise. By keeping the width variable constant, gives more consistency in the results.

filename	ε 4rms=	Sum of Intensities	reduction of ε 4rms	% of intensity kept	Width Variable, w.
UNROTATED IMAGES					
14030318	**235.8**	17048	0.0%	100.0%	no suppression
14030318	**221.8**	16891	6.0%	99.1%	15
14030318	**216.5**	16802	8.2%	98.6%	13
14030318	**209.8**	16579	11.0%	97.2%	10
14030318	**196.1**	16298	16.8%	95.6%	7
14030318	**176.4**	15903	25.2%	93.3%	4
14030318	**145.4**	14809	38.3%	86.9%	0
ROTATED IMAGES					
14030318	**224.7**	17377	0.0%	100.0%	no suppression
14030318	**206.4**	17098	8.2%	98.4%	15
14030318	**195.1**	16993	13.2%	97.8%	13
14030318	**179.2**	16644	20.3%	95.8%	10
14030318	**166.5**	16318	25.9%	93.9%	7
14030318	**154.4**	15879	31.3%	91.4%	4
14030318	**127.6**	14393	43.2%	82.8%	0

Table 6: Summary of the noise reduction results.

To see how the value of the width variable changes, the emittance was calculated across a range of values, and the results can be seen above in Table 6. This is also operator dependant as it is their judgement that creates the line between chopping all the noise, and zeroing too much and some of the beam is lost. As can be see in Table 6 the emittance can be greatly affected by reducing the width variable.

4.5.3: Hole area correction

Each pepper pot is a circular metal plate with 169 holes of nominal diameter 0.2mm cut into it, in the pattern of a square array. The holes were cut by a laser and the reproducibility of the area of each hole was not known. It is important to know the size of the holes because then the relative intensity between each peak on a horizontal profile can be scaled to the amount of

beam passing through each hole. The area of each hole was measured with an optical microscope and by capturing an image, software allowed an accurate calculation of the area to be made. Two pepper pot plates were measured and the results of these measurements are shown in Figure 29. This shows that the plate number 2 had the most consistent area of holes, which is on the right. The large peaks are where there was "double holes", which could have been caused by a shift in the laser to plate alignment during cutting.

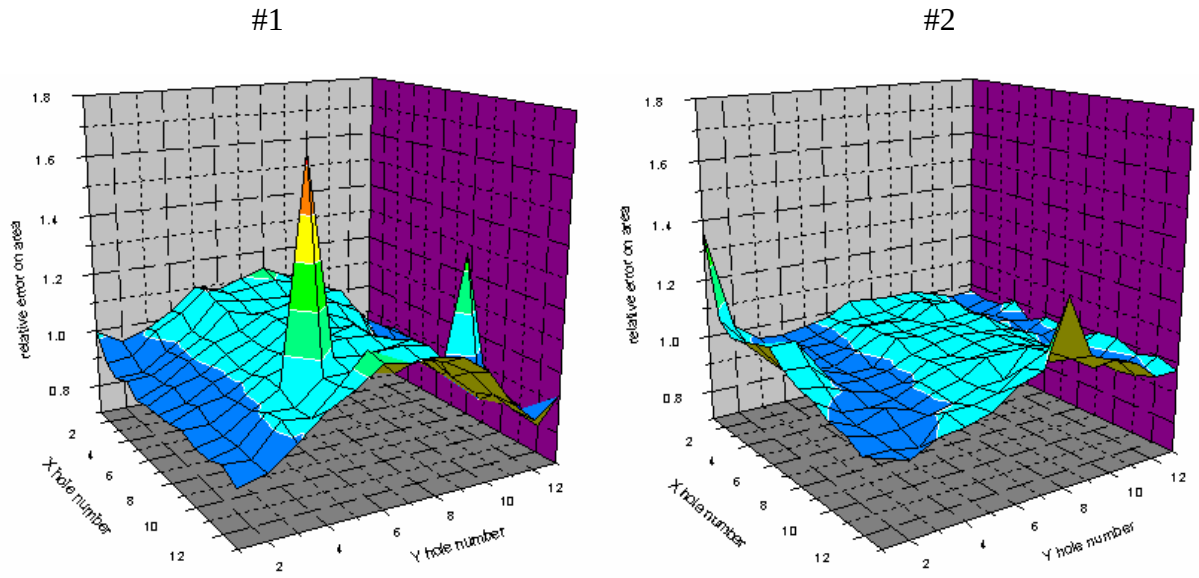

Figure 29: The consistency of area of the holes in the two plates.

The emittance of file 14030318 was calculated with and without the hole area correction data for plate number 2. All noise reduction parameters were kept the same. Table 7 shows that the difference in emittance after hole area correction is 1%. Due to this small difference, and to save time in the calculations, this data was not used during the calculation of emittance.

filename	ε 4rms=	total ε=	α=	β=	γ=	Option
14030318	**190.6**	338.4	-1.365	0.589	4.855	no hole area correction
14030318	**193.7**	338.4	-1.356	0.584	4.861	with hole area correction

Table 7: Summary of the hole area correction data results.

4.5.4: Error Summary of Emittance Measurements

Shown here are the errors for the emittance measurements. Some errors are caused by the accuracy of the equipment, and other cause by the method of calculating the emittance. Here is a list of the errors, with an estimate of the percentage error of each.

1. Noise suppression (operator dependent) –Repeated calculations on the same data, using different noise elimination, leads to variation of the resulting emittance with δ=10%.
2. The pepper pot has hole spacing error of δ=2%.
3. Screen to pepper pot distance δ=1%
4. The pepper pot was slightly rotated, compared to the horizontal and vertical axis of the CCD camera. Over 5 illuminated holes, it appears that the hole was displaced by 0.5mm, corresponding to a further error of δ=10%. After the image has been rotated in TPImager, this error can be cancelled to approximately 1 pixel per 100, which corresponds to $\delta \sim 2\%$
5. The hole areas have δ=5%, but this only affected the emittance result by 1%, and so the data collected to correct this was not used, as it added considerable time to the calculation.
6. The noise from ambient light and CCD noise was not accounted for.

As an estimation, the errors for the emittance are, by addition of the above:

$$\delta \sim 16\%$$

4.6: Conclusion

The emittance results of 140mm.mrad 4rms un-normalised found here is a good start for further investigation of the ion beam in the new LIS at CERN. As normalised emittance cannot decrease without expensive electron cooling systems, the emittance found should be lower than the estimated emittance further down the chain. To match the beam to the RFQ and the Linac, the emittance to be aiming for is 0.65mm.mrad 4rms normalised [4-4]. The results here are a little above that, but if the reliability issues can be over come, the emittance should be able to be within the limit, which corresponds to an un-normalised emittance of 120mm.mrad, and some shots were below this. Unfortunately, due to CERN choosing LEIR as the LHC heavy ion beam injector chain solution, the LIS was no longer able to be financially supported by CERN and work had to be ceased.

Chapter 5: Charge State Distribution measurements of the ECRIS

5.1: Introduction

As part of the restudy of the Linac, the Charge State Distribution (CSD) of the ECR source was measured. Having this data available can show how efficiently the source is operating, and how certain parameters affect source performance. For the multi-charge acceleration study being completed [5-1], it was useful to add this information to the simulations in order to show how the intensity of each charge state would enter the Linac's accelerating sections with the present source. This allows a more accurate simulation of the beam travelling through the Linac, if that scheme is used in the future.

It was first necessary to modify the existing CSD program, before any measurements could be made. This chapter will describe the modifications of the program and then present the charge state distribution (CSD) scans after the spectrometer in the LEBT of Linac 3, which have been obtained using the modified software.

A further CSD scan was also completed at a lower extraction voltage to include the O^{1+} peak in the charge state distribution. This allows an examination of all the waveforms from the 3 oxygen peaks.

After the Linac was switched to produce In^{21+} during the summer of 2003, the CSD scans were repeated for the indium beam.

5.2: The Linac Element Scanning Program

5.2.1: The Program

All variables on Linac 3 are controlled by computer. This includes the amount of current flowing through the wires in every magnetic item, and all the diagnostic equipment. For each element, there is a command (CCV) value and an acquisition (AQN) value. The CCV value is the value the user wants the computer to set the element.

The program, before modification, sets CCV values of up to four different elements on Linac 3, and retrieves a trace from an oscilloscope. Then it displays the average value in the time interval set either by the oscilloscope's gating cursors or using the retrieved trace data. The software then increments the CCV value and repeats the process, therefore creating a scan of CCV values.

5.2.2: Modifications to the CSD Program

Previously, Lab View and Visual Basic were used together. Visual Basic was the main programming language of the program, which set and incremented the CCV values. Lab View was used as a data server from an oscilloscope for the Visual basic program.

The modifications now use Visual Basic to take the trace from the oscilloscope and save it, so making it the only programming language in the program. This was done using Visual Basic GPIB functions taken from National Instruments programming documentation. It is also useful to see how the beam profile changes during a scan of an element, and so the program was modified to allow data to be recorded from a SEM grid.

5.2.3: Post Processing Program

During a CSD scan, the total oscilloscope waveform trace is saved at every element increment. Therefore it is possible to read in this data into a program, select the time interval required, and average the data within this time interval. This feature has been incorporated into the CSD software, which saves the new average data.

5.3: Charge State Distribution Scans of Lead

5.3.1: Introduction

The ions used for experimental physics are Lead, 208-Pb. A Charge State Distribution scan shows the relative intensity of all the different charge states of particles coming out of the source, by taking the intensity of the beam across a range of the spectrometer magnet currents.

5.3.2: Method

Elements ITL.BHZ01 and ITL.BHZ02 were scanned from 60 to 100 Amps each in 0.05 Amp steps, using the above scanning program. Both bending magnet currents were scanned with equal values. Also elements ITL.SOL01 and ITL.SOL01 were scanned relatively to the bending magnets, with the ratio:

$$eleCurr_{start} = eleCurr_{nom} \times \frac{bendCurr_{start}}{bendCurr_{nom}} \qquad (5.3.2.1)$$

Where “eleCurr” is the current of the solenoid or quadrupole to be set, at the new starting position, and takes the original, nominal settings. “bendCurr” is the bending magnet currents at the same places.

The trace of the oscilloscope was taken from Faraday cup ITL.MFC02 at each step of the scan. The average current was taken using the mean from oscilloscope cursors located at 0μs and 370μs after the input trigger IX.SEJ, which is at the start of the after-glow peak from the source. These results were taken using extra magnetic suppression around ITL.MFC02, to reduce negative signal between peaks.

A further scan was completed, with extraction voltage at 12.5kV, this is shown in Figure 31. This was done because the bending magnet’s maximum current limit is approximately 100Amps. With lower extraction voltage, particles have less kinetic energy, and so require less magnetic field to bend them around the spectrometer. This is so a calculation can be made of the O^{1+} peak, which would have a peak greater than 100 amps at the normal extraction voltage.

In Figure 32, the two scans were combined to give a wider charge state distribution range. The scan at 12.5kV was increased in vertical scale by 45%, so the main Pb peaks fitted over each other. The bending magnet values were also scaled to co-inside with the scan at 20.15kV, and the equation to do this was:

$$bendCurr_{20.15} = bendCurr_{12.5} \times \frac{O^{2+}Curr_{12.5}}{O^{2+}Curr_{20.15}} \qquad (5.3.2.2)$$

Where “bendCurr” is the bending magnet current at the two extraction voltages and “O^{2+}Curr” is the value of the current at the maximum of the O^{2+} peak at each voltage.

There are Faraday cups before and after the spectrometer bend in Linac 3. If we are not losing any beam between the two Faraday cups, the total current before it should be comparable with the sum of all the peak currents after the bending magnets.

5.3.3: After-Glow Results

Figure 30 shows the results for the scan of the bending magnet current at extraction voltage 20.15kV. It is unclear, in the O^{2+} / Pb^{26+} peak, of the relative amounts of the two charges, as they have the same charge to mass ratio, however, from the general trend in intensity of the charge states we can assume that the ratio is 1:1. When all the peak currents were summed from Figure 30, the result was 0.717mAmps, as shown in Table 8.

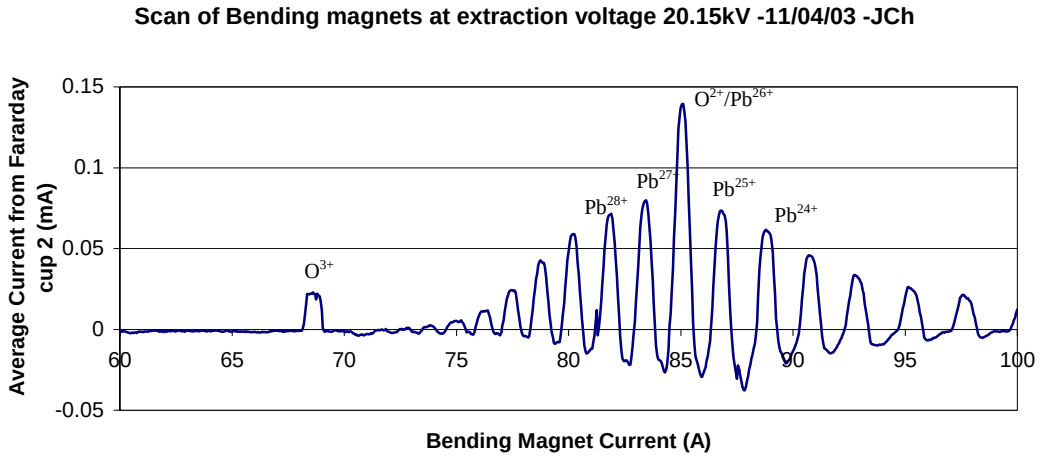

Figure 30: Scan of bending magnet currents at 20.15kV

Bending Current at peak maximum (A)	Charge State	Maximum Current of peak (mA)
68.60	O^{3+}	0.022
75.20	Pb^{33+}	0.005
76.35	Pb^{32+}	0.011
77.50	Pb^{31+}	0.024
78.75	Pb^{30+}	0.042
80.25	Pb^{29+}	0.059
81.90	Pb^{28+}	0.071
83.45	Pb^{27+}	0.079
85.10	O^{2+} / Pb^{26+}	0.139
86.80	Pb^{25+}	0.073
88.80	Pb^{24+}	0.061
90.70	Pb^{23+}	0.045
92.75	Pb^{22+}	0.033
95.15	Pb^{21+}	0.026
97.55	Pb^{20+}	0.021
Total Sum	**All**	**0.717**

Table 8: Showing maximum current at each peak from Figure 30.

The two scans (Figure 30 and Figure 31) were scaled together and this can be seen in Figure 32. From these results it is seen that the O^{1+} peak has an estimated current of 101μA at a bending magnet current of 123Amps.

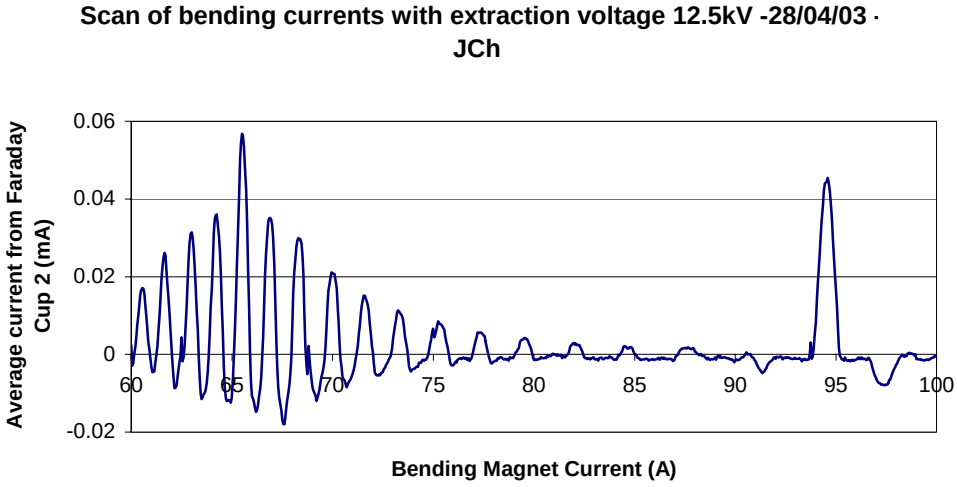

Figure 31: Scan of bending magnets at 12.5kV.

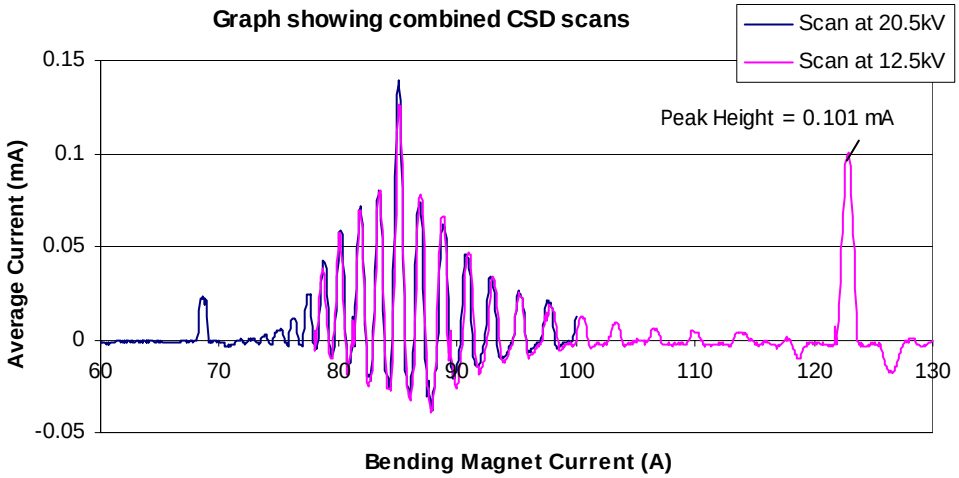

Figure 32: Combined scan, from the different extraction voltage scans.

Figure 33 shows some traces from Faraday cup ITL.MFC01. Having taken several traces, the average current in the same time interval (0μs to 370μs with respect to the trigger IX.SEJ) was 0.397mAmps. This is a lot less than the total current found in Faraday cup ITL.MFC02, so maybe we are not getting all of the beam into cup ITL.MFC01, which has an aperture of 30mm [5-2]. To put all of the beam into the cup, the scanning program could be used to scan the solenoid (ITL.SOL01) values to reduce the beam envelope size at the cup aperture, and find the maximum current. This was completed (the graph is shown in Figure 34, and the waveforms from Figure 33, come from this) and the maximum current was found to be 0.595mA with 138Amps on the solenoid.

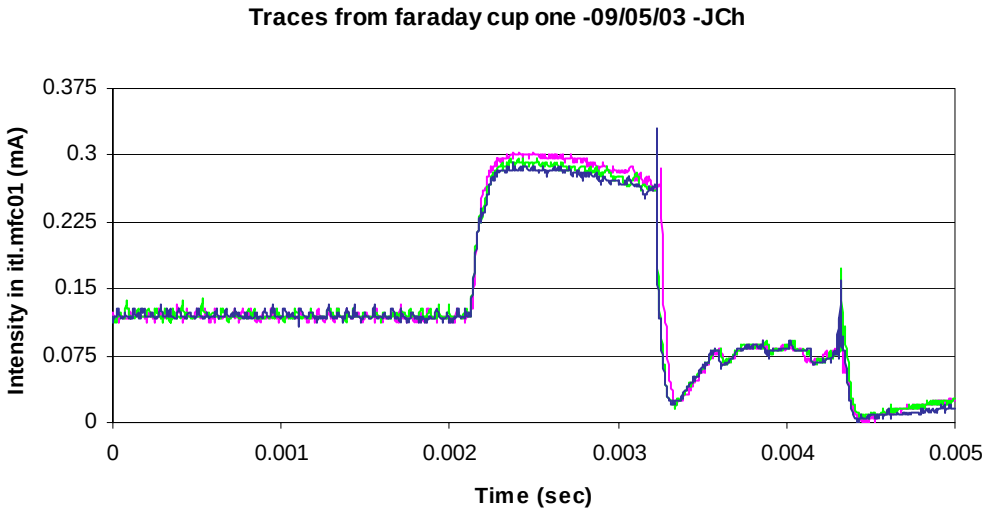

Figure 33: Examples of traces from Faraday cup ITL.MFC01.

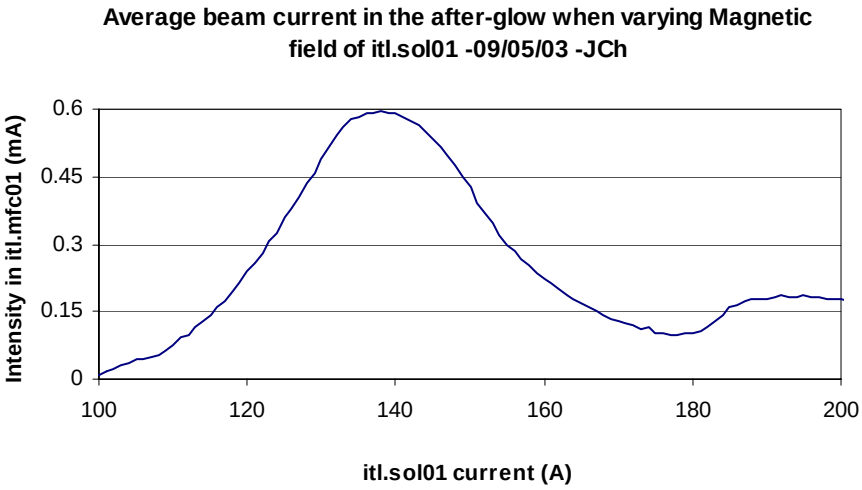

Figure 34: Beam current measured in Faraday Cup ITL.MFC01 as a function of solenoid ITL.SOL01 current.

This means that the beam current in Faraday cup ITL.MFC01 is 0.595mA compared to the 0.818mA current measured on Faraday cup ITL.MFC02, now with the O^{1+} current included. Notice that there is still less current before the spectrometer, approximately 0.2mA, than after

it. This could be explained by high-energy electrons coming out of the source, which would reduce the intensity in Faraday cup 1, but would not travel around the bending magnets.

Figure 34 shows 2 peaks in the current at 138 and 190 Amps. The second peak approximately corresponds to the solenoid current required to focus the O^{1+} beam into ITL.MFC01. This shows that not all the beam is focused into the Faraday cup at a single solenoid setting, and could explain why we see less current in ITL.MFC01. To see if theory supported this, the beam widths for the oxygen charge states were calculated as a function of solenoid strength, and can be seen in Figure 35. This was calculated using the MathCAD file also used in Chapter 6. This shows that if every charge state had the same Twiss parameters at the exit of extraction from the ECR source, then not all the intensity of all the charge states would go into the cup at any one solenoid strength. A simulation of the solenoid was then started to improve our understanding.

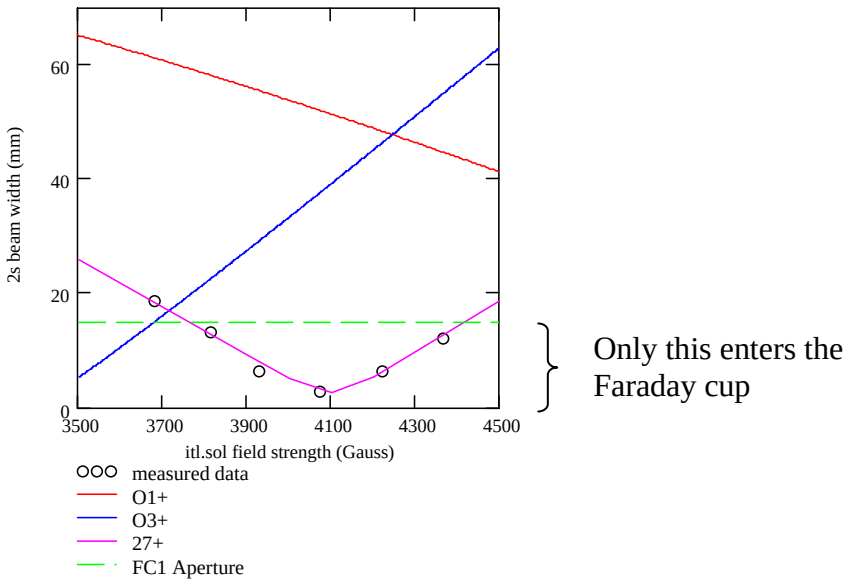

Figure 35: Plot of beam width (2σ) at Faraday cup ITL.MFC01 position as a function of solenoid ITL.SOL01 field strength.

A photo of the faraday cup is shown in Figure 12, with a 30mm aperture. In the beam width graphs the aperture limit is indicated, when the beam would not go into the cup. Assuming the beam is a Gaussian function, only a fraction of the intensity that reaches Faraday Cup ITL.MFC02 would go inside the first cup aperture. Hence, the formula to calculate the fraction of a Gaussian beam with beam width σ passing through an aperture of radius r is given as [5-3]:

$$\frac{I(r)}{I_0} = 1 - e^{\frac{-r^2}{2\sigma^2}} \qquad (5.3.3.1)$$

Assuming no beam is lost between the two cups and the correction factor is applied to each charge state in Faraday Cup ITL.MFC02, it should give the amount of beam current that passes into cup ITL.MFC01. The intensity of each charge state was taken from the CSD scan completed in Figure 32. Comparing this calculation with the measured current in Figure 34 gives the plot in Figure 36.

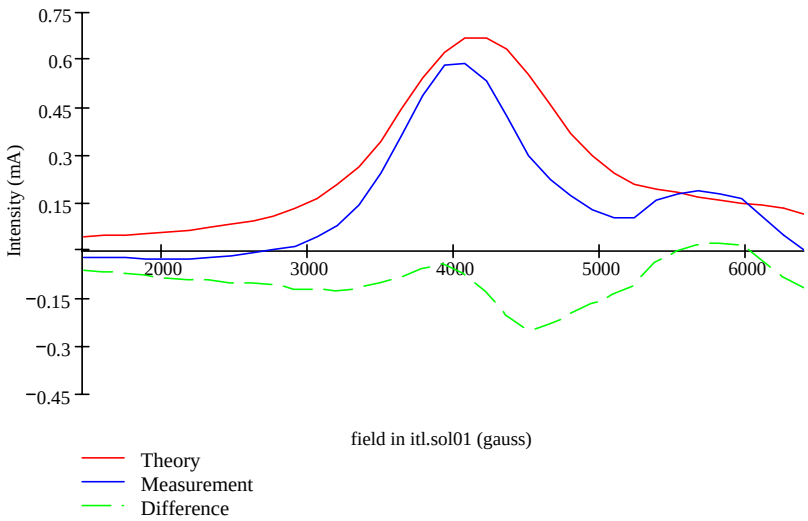

Figure 36: A comparison between measurement and theory for the solenoid scan.

As shown above, the new simulation matches the measured data better. However there are a few points to notice. At low ITL.SOL01 fields, the value of the intensity in ITL.MFC01 drops below zero in measurement. This indicates there could be electrons entering the cup from the source. Hence, a constant factor may need to be subtracted. Also, the increase in intensity from 5000 gauss in the measured data is not seen in the simulation. Assuming the main peak is where the oxygen 26+ is most focused into the cup, the secondary peak is where the oxygen 1+ is expected. With its small charge to mass ratio, some the intensity of the oxygen 1+ may be lost around the bending magnets, and so isn't measured in cup ITL.MFC02. To test if this was true, the intensity of the oxygen 1+ beam was increased to 0.450mA. This then created the bump not seen before in simulation, shown in Figure 37, and we can assume that oxygen 1+ is being lost in the bending magnets.

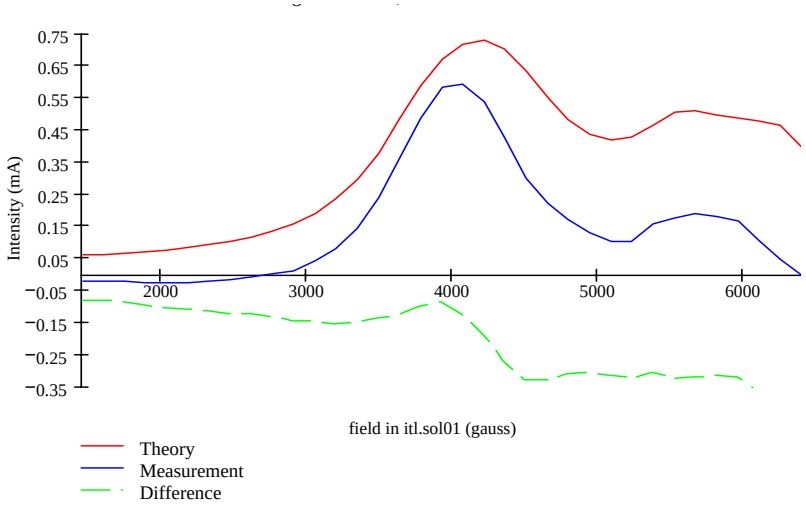

Figure 37: Simulation and Measurement after an increase of O^{1+} current.

As seen by the green line above, the difference between simulation and measurement on one side of the main peak is constant, but changes at the point of the maximum. This shows that there is an extra effect occurring on one of the two sides. This is not understood yet, but there

have been many assumptions in this simulation. No space charge has been included and the beam is assumed to be a Gaussian distribution with all the charge states having the same output Twiss parameters from the source. Also the beam is assumed to be centred, which ignores the effect that changing the strength of the solenoid could be steering the different charges states across the faraday cup. All these things, if investigated, could help to improve the current simulation and understanding of this part of the Linac.

5.3.4: Pre-glow Results

Figure 38 shows the pre-glow scan, taken from the waveform data collected on the 11th April 2003, which is shown in Figure 30. The time interval taken was 1800μs to 2000μs relative to the start of the oscilloscope trace. Relative to the input trigger on the oscilloscope, this corresponds to a time of −700μs to −500μs. A typical waveform trace is shown in Figure 39, and this shows the time interval used in this calculation.

The data shows the appreciable increase in the high charge state Pb ions and the reduction in the intensity of the oxygen beam in the afterglow. The ratio of intensities between O^{2+} and O^{3+} has almost halved, from approximately 6:1, to 7:2, showing the O^{3+} beam is suppressed during the afterglow peak.

The ratio to the O^{2+} peak to the lead peaks either side is 30:1. This value comes from the main peak having a maximum height of 0.177mA and the small Pb peaks having a maximum height of 6μA.

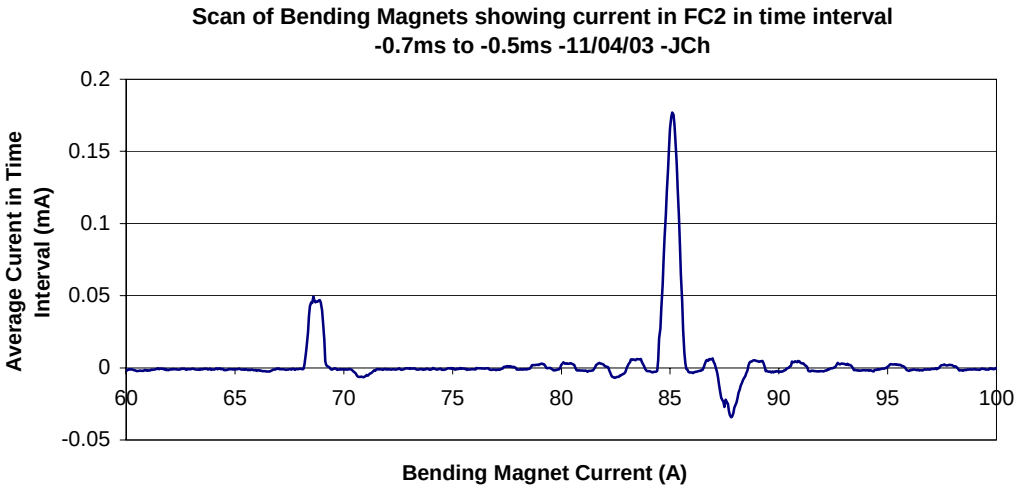

Figure 38: CSD scan during the Pre-glow into Itl.MFC02.

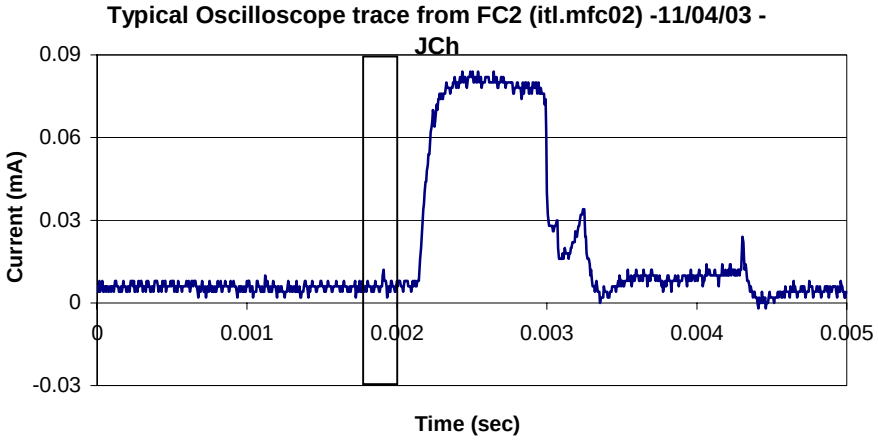

Figure 39: Typical oscilloscope waveform trace from ITL.MFC02, showing the time interval used for pre-glow.

5.3.5: Oxygen Peak Waveforms

Presented here is a selection of waveforms taken from Faraday cup ITL.MFC02. They were taken from the data summarised in Figure 30, around each maximum peak point. The bending magnet current, in amps, is given for each waveform.

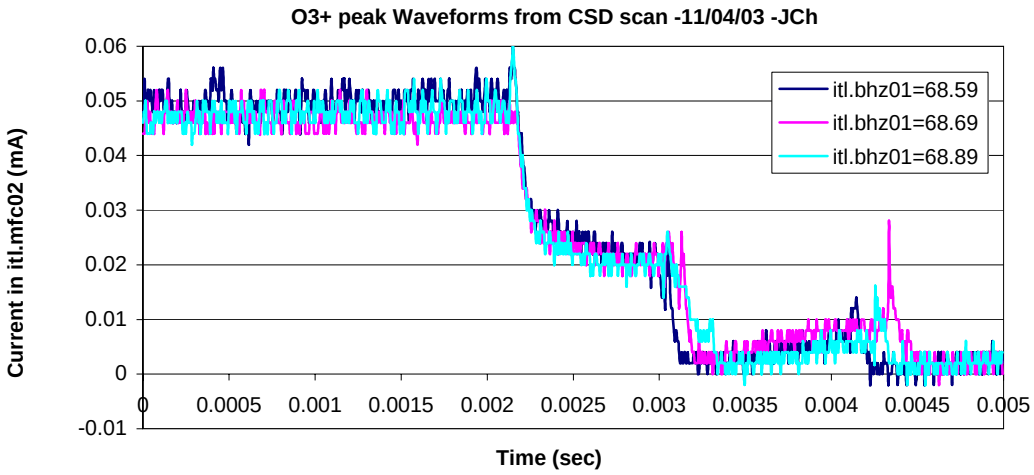

Figure 40: O^{3+} waveforms from CSD data.

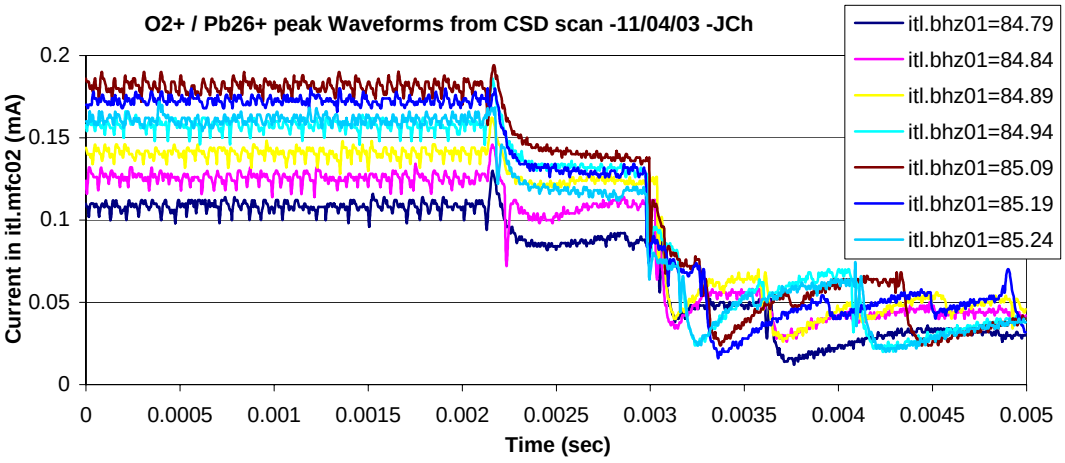

Figure 41: O^{2+}/Pb^{26+} waveforms from CSD data.

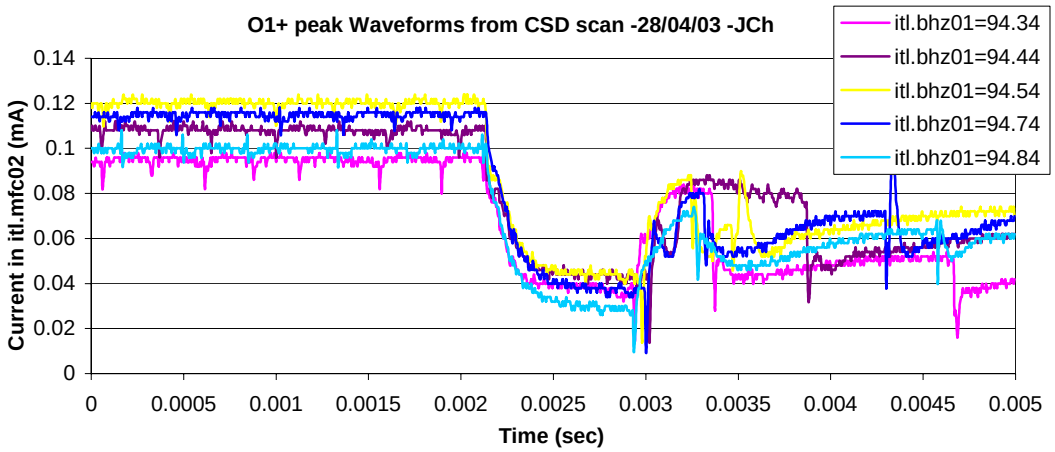

Figure 42: O^{1+} waveforms from CSD data.

Notice the O^{2+} waveform does not decay as much as the other two, this is due to the presence of Pb^{26+}, as they have the same charge to mass ratio. The O^{1+} has the same charge to mass ration as Pb^{13+}, and this may occur in the end of the afterglow. This could be causing the various peaks after the afterglow, in the time range greater than 3.5msec in the graph above.

5.4: Charge State Distribution scans with Indium

5.4.1: Method

CSD scans have also been performed with the Indium beam, which the Linac provided in 2003. As with lead, the bending magnets, the first solenoid and the first quadrupole were scanned together to give a CSD distribution into ITL.MFC02 (Faraday cup two). Also in another scan, the extraction voltage was reduced to 12.5kV, this was to measure the O^{1+} peak. The maximum intensity into Faraday cup ITL.MFC01 was found by a scan of the first solenoid.

5.4.2: Results

Figure 43 shows the scan of the solenoid ITL.SOL01 into Faraday cup ITL.MFC01. This gives the current of the indium beam before the bending magnets as 0.419mA.

The CSD scans are shown in Figure 44 and Figure 45. The combined scan of these two can be seen in Figure 46. The total current after the bending magnets for the indium beam is 0.592mA, and this includes the 0.099mA of the O^{1+} peak. The difference in intensities between Faraday cups one and two is approximately –0.2mA, which is similar to the difference of the Faraday cups with the lead beam. Unlike the lead results, this difference was not investigated.

In Figure 46 the pre-glows and the after-glows have been put onto the same graph. It is noticeable that the pre-glow peaks occur at a lower bending magnet current than the after-glow peaks, for the same elements. This means that the pre-glow was at a higher energy than the after-glow. This can be explained because the bouncer was switched on for the CSD of the indium. The bouncer was installed to only give the correct energy for the afterglow, and so varies the extraction voltage during this period.

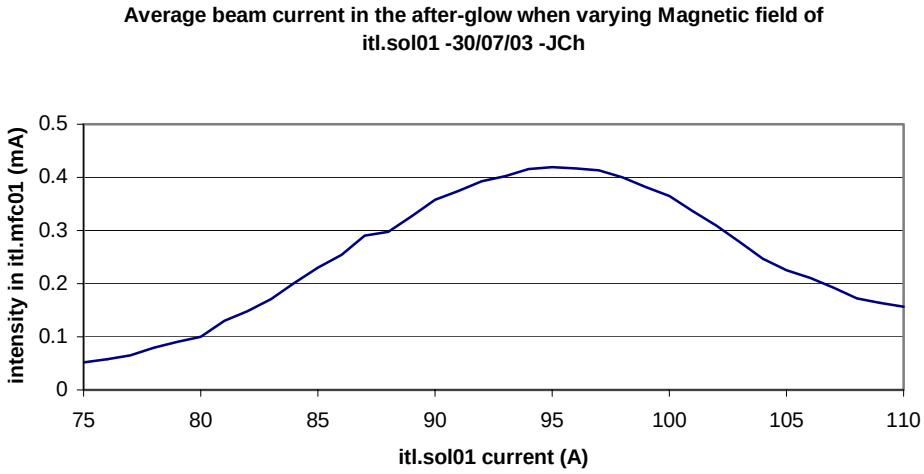

Figure 43: The intensity in Faraday cup ITL.MFC01 as a function of solenoid ITL.SOL01 strength.

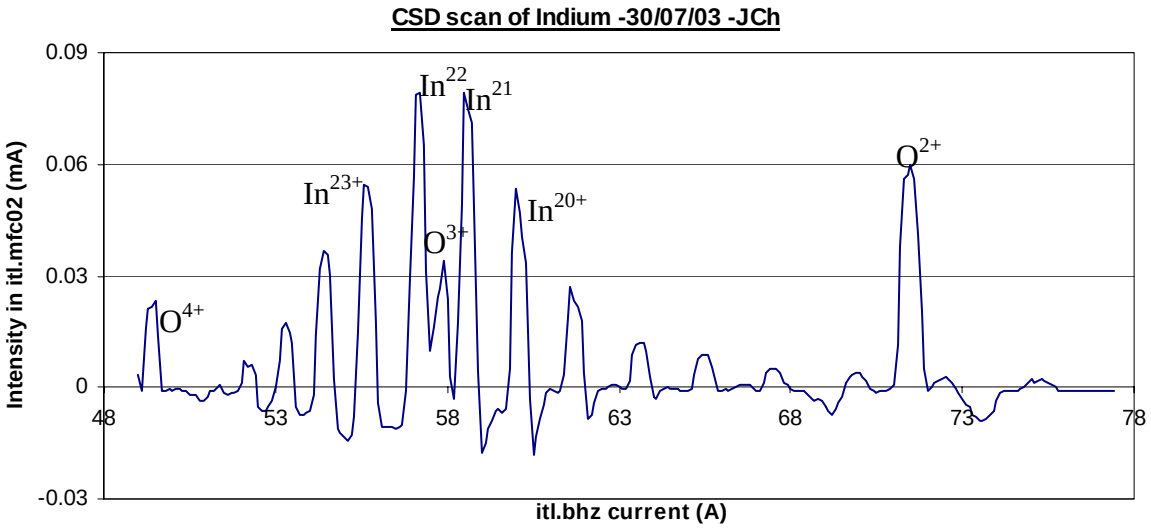

Figure 44: CSD scan of the indium beam at 14.3kV.

Bending Current at peak maximum (A)	Charge State	Maximum Current of peak (mA)
49.5	O^{4+}	0.0235
52.1	In^{26+}	0.0071
53.3	In^{25+}	0.0173
54.4	In^{24+}	0.0367
55.6	In^{23+}	0.0547
57.2	In^{22+}	0.0793
57.9	O^{3+}	0.0343
58.5	In^{21+}	0.0791
60.0	In^{20+}	0.0533
61.6	In^{19+}	0.0268
63.6	In^{18+}	0.0122
65.5	In^{17+}	0.0087
71.5	O^{2+}	0.0598
Total Sum	**All**	**0.493**

Table 9: Showing the peak heights of each charge state in the indium beam.

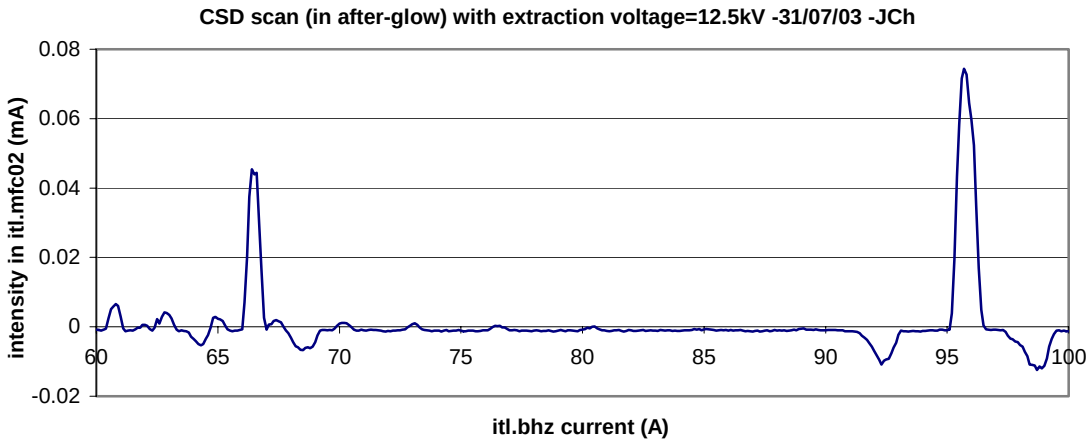

Figure 45: The CSD scan at 12.5kV of the Indium beam.

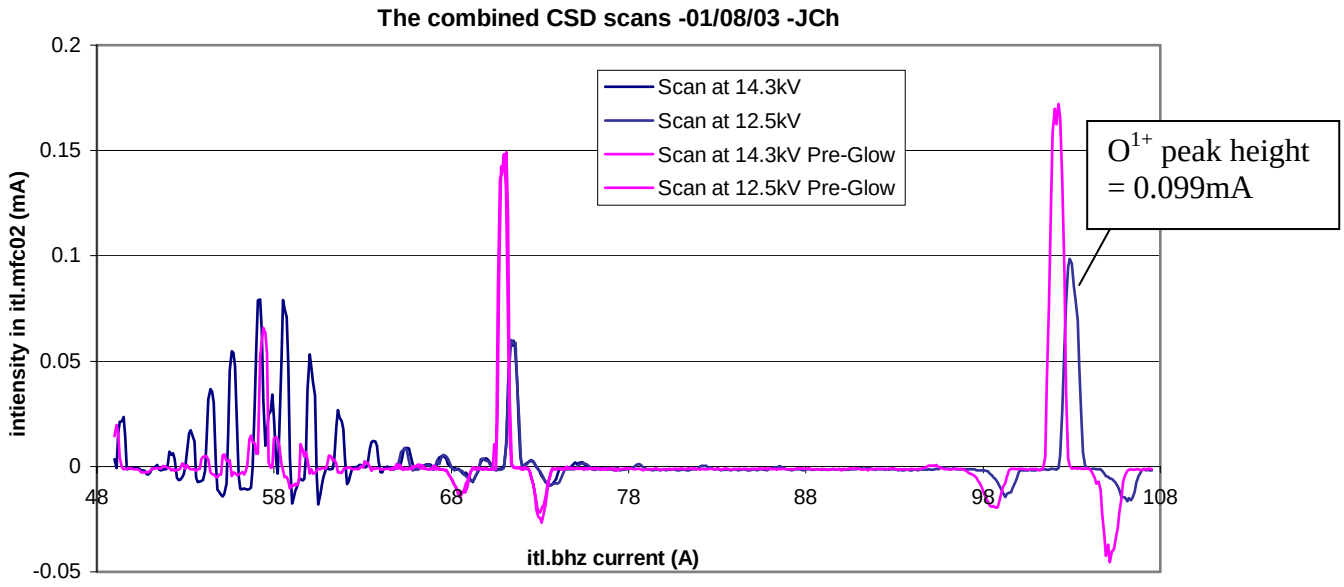

Figure 46: The pre-glow and after-glow of the CSD scans for indium.

5.5 Conclusions

Shown here are the CSD scans for Lead and Indium, which the ECR source at CERN supplied in 2003. These show the many charge states it produces, and their relative intensities. They also give a good reference when the source is operating correctly.

It has been determined that the intensity of O^{1+} in the afterglow of the Lead beam is 101μA into Faraday Cup ITL.MFC02. The intensity in ITL.MFC02 was greater than the intensity into ITL.MFC01, this is explained by the focusing properties of the solenoid ITL.SOL01 and that high-energy electrons could be extracted with the beam. It has also been suggested that O^{1+} is being lost in the bending magnets, ITL.BHZ01 and 02. This is not important as O^{1+} is not required after the spectrometer, and the vacuum conditions are sufficient with the losses.

Chapter 6: Single Charge Beam profiles for emittance measurements

6.1: Beam Profiles

A transverse beam profile gives the intensity distribution within the beam at right angles to its motion. Although the distribution of the ECR source is thought to be “star-shaped” [6-1] (see Figure 47), the measurements in this section assume the beam to have a Gaussian distribution, of the form [6-2]:

$$f(x) = \frac{1}{\sigma\sqrt{2\pi}} e^{-\frac{(x-\mu)^2}{(2\sigma^2)}} \qquad (6.1.1)$$

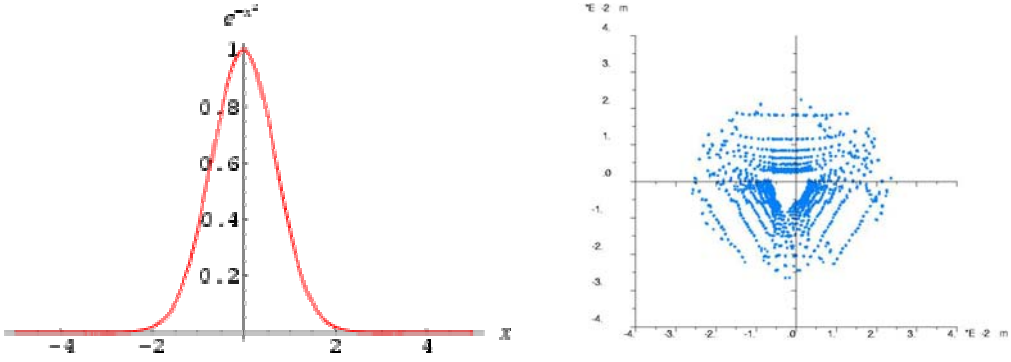

Figure 47: The transverse profile of a Gaussian beam (left) and a plan view of a star-shaped beam (right).

Where in equation 6.1.1, σ is the Full Width at Half Maximum (FWHM). Due to the measurements in this section being only 1 dimensional, this assumption does not induce a large error.

6.1.1: Introduction

Beam profile measurements at the LEBT of Linac 3 have been performed using the first set of spectrometer slits. The emittance of the ECR source has not been measured before the spectrometer since it was on the test bench, and so will provide a key test to see if the source is still performing as expected. This chapter shows the method and results of the measurements. Further measurements using this method are used to calculate the emittance of the ion beam before the spectrometer. After the Linac was switched to provide an Indium beam, the emittance of this beam was also calculated in the same place, to compare the two beams.

6.1.2: Method

Figure 48 shows the layout of the LEBT of Linac 3 [6-3]. The element, ITL.MSGHV01, which is a SEM grid, is not operational and so another method to find the beam profile at this point is needed. In this report, the spectrometer slits itl.slhv01 are used.

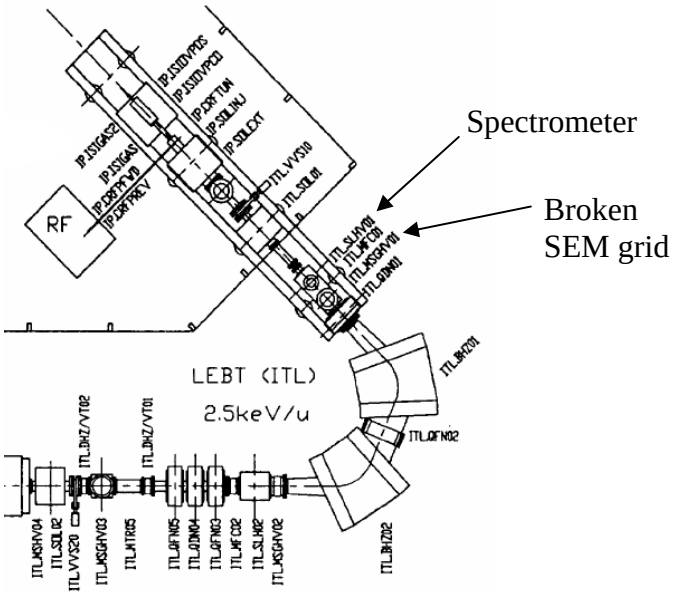

Figure 48: Schematic layout of LEBT.

Each spectrometer slit (left, right, top bottom), located before the spectrometer, can be moved in and out of the beam using computer control. Using the Charge State Distribution program given in Chapter 5, each slit was scanned along its entire travel of motion (see Table 10), taking the beam current in a Faraday cup at each slit position. This showed that each slit only moved 5mm past the centre point, and so two scans are necessary for each beam profile measurement.

Slit name	Minimum Position (mm)	Maximum Position (mm)
ITL.SLH01left	-45.00	-4.08
ITL.SLH01right	-5.50	37.80
ITL.SLH01top	-5.43	36.52
ITL.SLH01bottom	-36.98	5.88

Table 10: Table showing available motion of slits.

In Figure 49, it can be seen that by moving a slit into the beam, it reduces the intensity that passes the slits. Assuming the entire beam that passes the slits goes into the Faraday cup, the difference in the intensity between two steps corresponds to the intensity in the blue section in Figure 49.

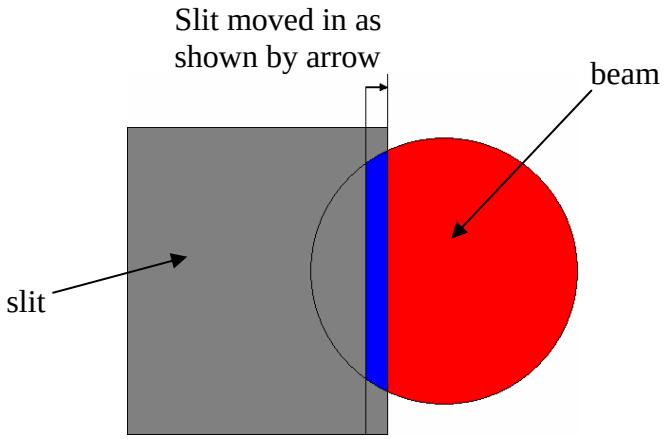

Figure 49: A step of the slit takes a chunk out of the beam.

From this, it is possible to find the 1 dimensional transverse beam profile by differentiating the intensity in the Faraday cup with respect to the slit position.

The beam profile of all the charge states was found by taking the intensity in ITL.MFC01, which is before the spectrometer bend. Selecting a charge state within the spectrometer, allowed the beam profile for that charge state alone, to be measured at the position of the slits before the spectrometer, by taking the beam current in ITL.MFC02.

6.1.3: Data Analysis

Figure 50 shows an example of a single slit guillotine scan.

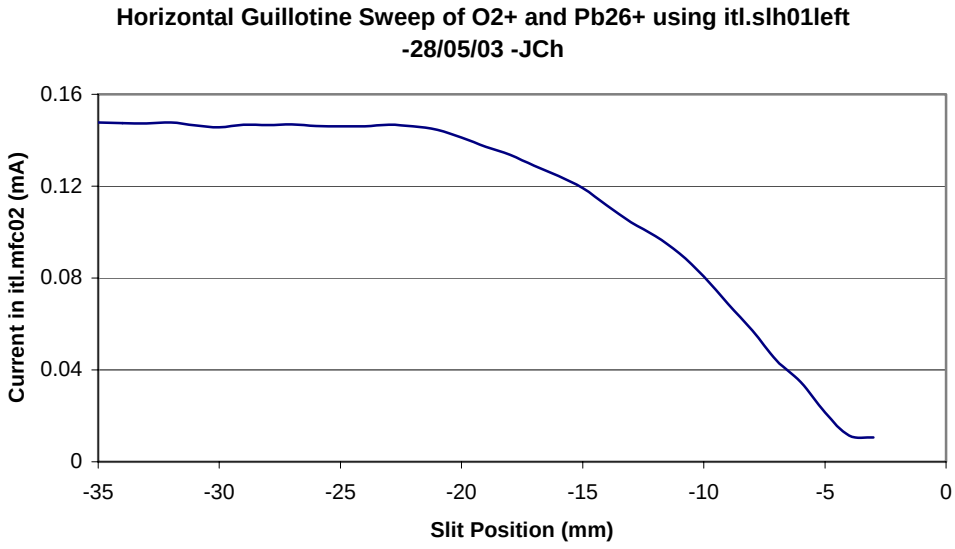

Figure 50: Example of a single slit guillotine sweep.

Notice that as the slit in Figure 50 is ITL.SLH01left, it does not reach the zero position (see Table 10). There is a level part at the right hand side of the line, and this is due to the fact that after the slit has reached its maximum (or minimum). The program controlling the slit does not allow it to move any further, but the CSD program, which sets the position for the

controller to then move the slit, does not have feedback, and so does not know that the slit is not moving anymore. Hence for all calculations, the data received that is outside the minimum and maximum points of each slit is removed.

The two slits, which oppose each other (top and bottom, and left and right) are then put on a single x-axis, to show the beam current relative to all slit positions, as shown in Figure 51.

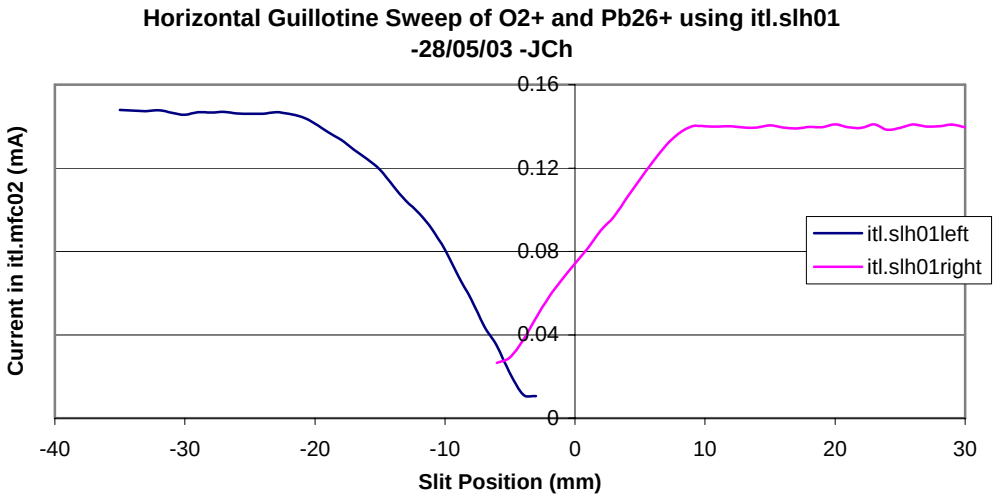

Figure 51:Example of two opposing slits placed on the same x-axis.

If the beam is transversely symmetrical and centred, then the beam current at position zero should be half (50%) of the amount when the slits are fully opened. Notice that this is not true in Figure 51. It is assumed that the beam is symmetrical, and each slit is shifted so that the zero position corresponds to half the normal beam current. This assumption can be backed up because when the differential of this graph is completed with shifted slits, the resulting beam profile for each guillotine sweep is centred on the zero position. Horizontally, there is a great difference between the shifts of each slit, and hence it is thought that the position encoder of the left slit is not well aligned. Vertically, the shifts in each slit are similar, and so this could

be due to an offset of the beam. The average amount the slits had to be shifted is shown in Table 11.

Slit Name	Average Amount Shifted (mm)
ITL.SLH01left	+ 8.5
ITL.SLH01right	+ 0.5
ITL.SLH01top	+ 3.0
ITL.SLH01bottom	+ 2.5

Table 11: Table showing the average amount the slits had to be shifted.

The left (or bottom) slit was then modified to give a graph, which is equivalent to a single guillotine sweep from –30mm to +30mm, using the equation shown in the legend in Figure 52. An example of this is shown in the figure below.

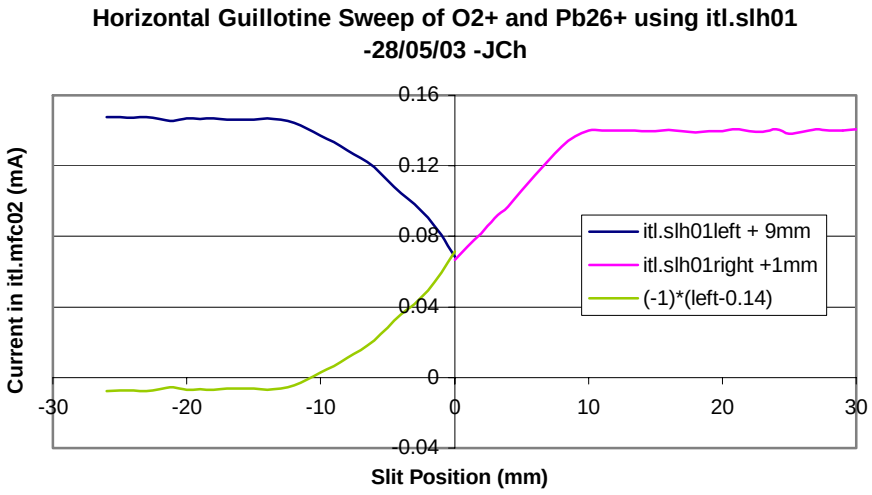

Figure 52: Example of how two guillotine scans were put together.

Figure 53 shows two differential graphs of the same horizontal slit sweep. This was before and after the slit-scanning program had been modified to average 10 beam shots before moving the slit to the next position. The noise in the differential graph was caused by shot to

shot variations in beam current, which can be seen to be greatly reduced after the modifications.

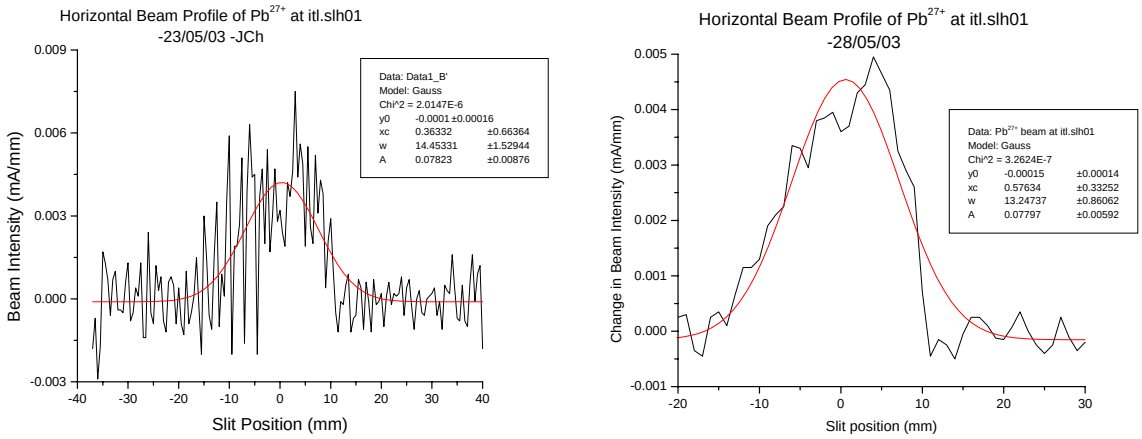

Figure 53: Comparison of graphs before and after modifications to the slit-scanning program.

It can be seen in Table 12 that this process has also reduced the errors in the results. The red lines in Figure 53 are a Gaussian fitting function provided by the graph-plotting program used to differentiate the data. The errors in Table 12 are the errors given by this fitting function.

The beam width given is the width variable, w, of the Gaussian fitting program used. The equation that was used:

$$y = y_0 + \frac{A}{w\sqrt{\frac{\pi}{2}}} e^{\frac{-2(x-x_c)^2}{w^2}} \qquad (6.1.1)$$

From [6-2] and (6.1.1) this shows that $w^2 = 4\sigma^2$ and so $\mathbf{w = 2\sigma}$.

6.1.4: Results

Table 12 gives the results of the beam widths for the scans completed. These results were calculated during the afterglow of the ECR source, which is 0μs to +370μs with respect to trigger IX.SEJ. This shows that the Pb^{27+} ions have a similar beam width to the O^{2+} ions. The Latest simulation results [6-4] give 2σ, of Pb^{27+} to be 8.6mm. This does not compare well and so further investigations will be carried out.

Part Of Beam Measured	Horizontal / Vertical	Beam Width (mm), 2σ.	
		Single shot scan	10 shot average scan
Total Beam	H	11.6 ±1.6	n/a
	V	9.5 ±1.1	n/a
O^{2+} / Pb^{26+}	H	11.2 ±3.2	13.8 ±0.86
	V	13.0 ±3.4	14.0 ±0.86
Pb^{27+}	H	14.5 ±1.5	13.2 ±0.86
	V	15.0 ±1.8	13.9 ±0.81

Table 12: Table of Beam width results at ITL.SLHV01, including results averaged over 10 shots.

6.2: Emittance Measurement before the spectrometer of the LEBT

6.2.1: Method

Guillotine sweeps of the method given above at the slits ITL.SLH01 were performed at different ITL.SOL01 solenoid magnetic strengths. The main parameters of the source are given in Table 13. Pb^{27+} was the particle measured for all profiles, and all other parameters were kept constant as much as possible. For higher solenoid currents the maximum intensity in the Faraday cup decreased significantly. When ITL.QDN01 was increased, this improved the current in the faraday cup to a level similar to before. This will not affect the beam width

results as there is the differentiation process, and also due to the fact the Faraday cup is position independent (apart from whether the particles go into the cup or not). However the intensity of the beam profile measurements cannot be compared. The beam profiles were plotted and the beam widths were calculated as in previous measurements. Figure 54 shows a comparison between the beam profile at the beam waist and another not at the beam waist. The beam widths were then plotted against the strength of the current in the solenoid, which is shown in Figure 55.

Extraction voltage	20.15 kV
Particle / Atomic mass	Pb / 208
Rest Mass	1.94 x 10^5 MeV
Charge State	27+
Velocity (β)	0.00237 c
Energy of particle / Energy per nucleon	0.54 MeV / 2.62 keV/u
Current at nominal setting (in itl.mfc02)	80 μA

Table 13: Parameters used in the lead emittance measurements.

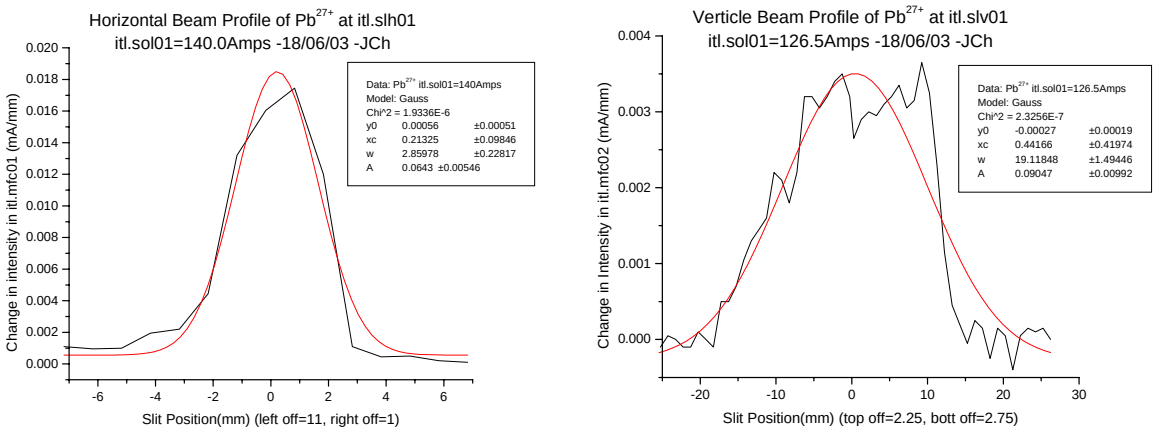

Figure 54: Graphs showing the beam profile at the waist (left) and away from the waist (right).

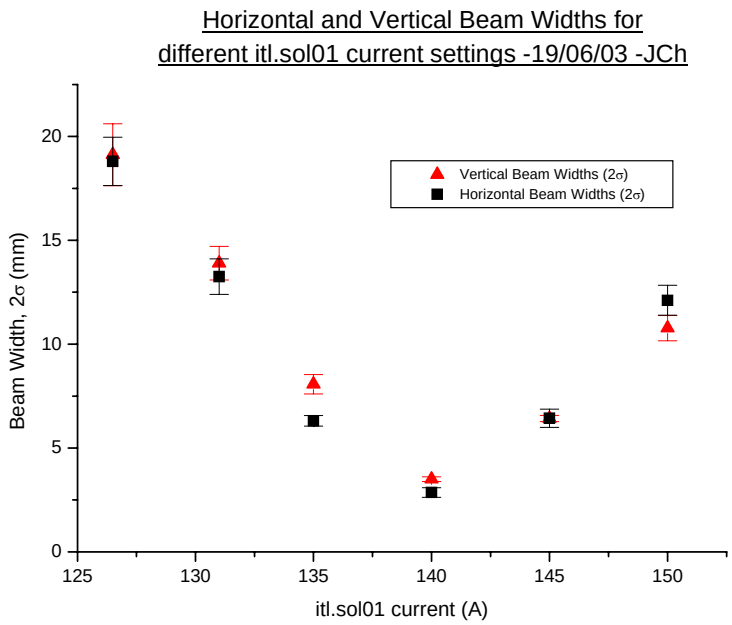

Figure 55: Graph showing the change in beam width against the current of the ITL.SOL01 solenoid.

The linear beam transport through the solenoid ITL.SOL01 was calculated with MathCAD, according to the sigma matrices given in section 2.1.3 and [6-5]. This transfer matrix changes with the strength of the solenoid, and so we can make this matrix a function of B, the magnetic field strength. We know the beam widths at σ_1, and from equation 2.1.3.3, we know σ_{11} (which is equal to the beam width squared) and can relate this to the Twiss parameters for each different R(B) as shown:

$$2 \times \mathrm{bw} = \sqrt{\sigma_{11}} = \sqrt{\beta \varepsilon_{\mathrm{rms}}} \qquad (6.2.1.1)$$

The Twiss parameters of the input σ matrix can then be varied to fit the beam profile to the measurements as a function of the solenoid B field. Figure 8 shows the best-fit beam width as a function of the solenoid B field.

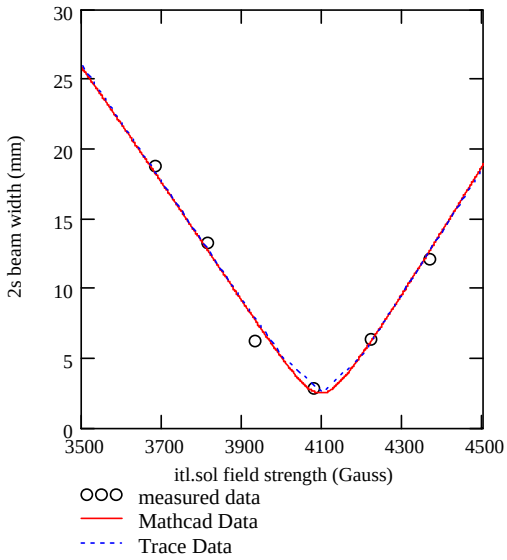

Figure 56: The MathCAD fitted curve, showing the measured data and the corresponding Trace plot.

Trace-3D was used to verify the MathCAD data for discrete values of the magnetic field. For the same parameters, e.g. magnetic rigidity, the MathCAD curve matches the Trace beam widths at specific solenoid strengths, for the same α, β, γ values entered.

6.2.2: Results

The emittance has been calculated at a position of 0.445m before first solenoid, where the transfer matrix starts. This is where the Trace file for the LEBT of Linac 3 begins, an example of this is shown in Figure 57. In Trace the slits are at the end of element 3, marked by a small vertical line. This is 0.851m after the solenoid and is where the transfer matrix ends. At the starting position the emittance and Twiss parameters are shown in Table 14. It is assumed that the beam is horizontally and vertically symmetric and so this applies for both

horizontal and vertical planes. The MathCAD file that calculated this can be seen in Appendix A.

α	β	ε_{4rms} (mm.mrad)
-0.89	0.04	100

Table 14: Results of the emittance measurement.

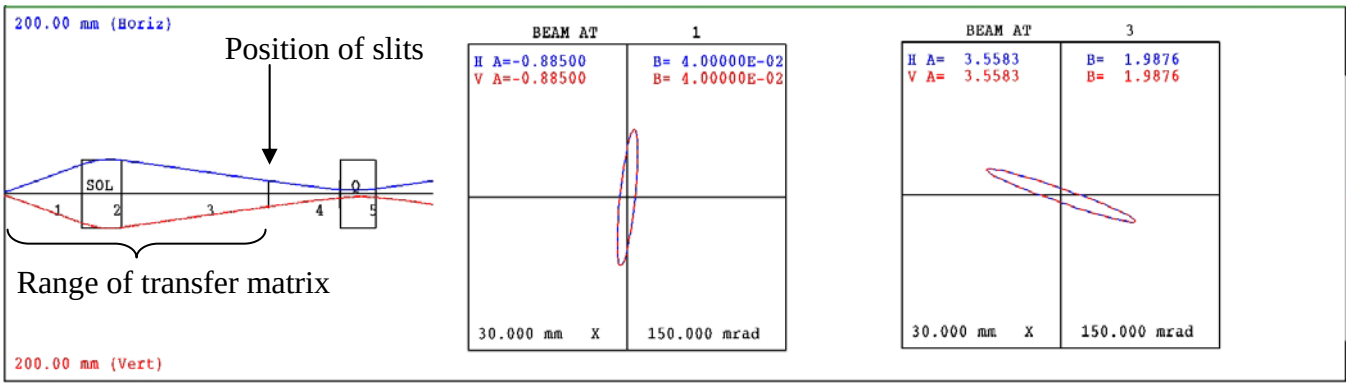

Figure 57: Example of the Trace program in the LEBT.

From recent simulation results [6-6], it has been suggested that the beam is scraping the beam pipe at or before the solenoid. Using Trace, it is possible to show the beam envelope size along the beam tube. The diameter of the beam tube at the solenoid is 70mm [6-7]. Figure 58 shows a zoomed picture of the beam with the measured parameters placed into the program, and also an added part to show the physical aperture of the tube. This shows that with the measured parameters, the beam does appear to be limited by the beam tube.

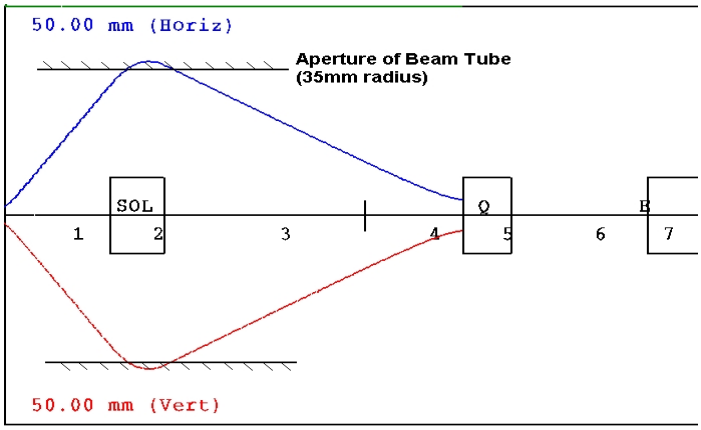

Figure 58: Trace beam showing the physical aperture of the beam tube.

So if the beam is touching the inside of the tube, we should be able to capture more particles by moving the solenoid towards the source. Due to vacuum valves and vacuum gauges, there was very limited space and so the solenoid could only be moved by 30mm. Figure 59 shows a comparison of a solenoid scan before and after the solenoid was moved, and we can see there was no increase in maximum beam intensity. This could also be due to the fact that the source had to be switched off for 30 minutes while the solenoid was moved, and so after this happens the source does not always return with the same output current. Calculations were made to estimate the amount of intensity we were expecting, and this gave 2.5% with a Gaussian distribution. This would be difficult to measure given the instabilities of the source.

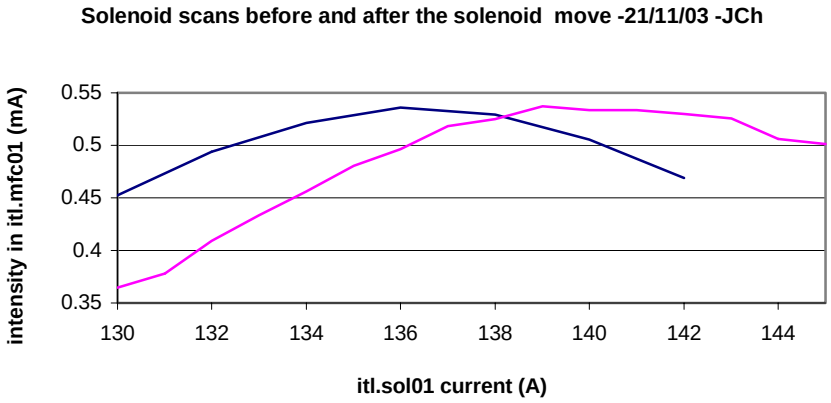

Figure 59: The result of the solenoid scans before and after the solenoid was moved.

When the measured parameters are put into Trace, the program should be able to calculate the beam parameters further along the LEBT. Emittance and Twiss parameters have been measured [6-8] at the exit of the second bending magnet to be:

	α	β	ε_{4rms} (mm.mrad)
Horizontal	4.84	5.58	133
Vertical	5.97	5.98	90

Table 15: Results of Measurements after the bending magnets.

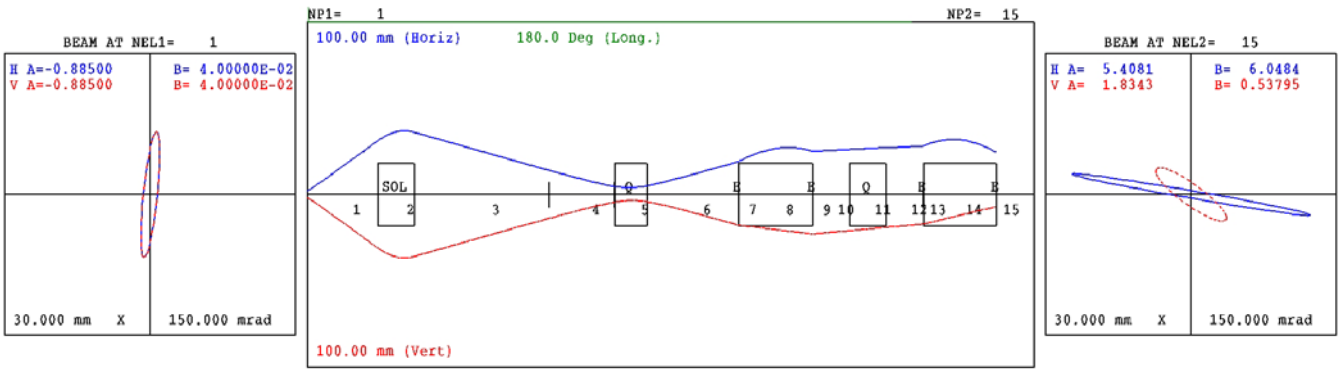

Figure 60: Trace file to compare the results after the bending magnets.

	α	β	ε_{4rms} (mm.mrad)
Horizontal	5.41	6.05	100
Vertical	1.83	0.54	100

Table 16: Trace's predictions of results after the bending magnets.

Figure 60 and Table 16 shows the result of Trace calculating the beam path through the bending magnets. The ellipse on the left shows the measured parameters from the measurements in this report and the ellipse on the right should give similar results to the measurements after the bending magnets. It can be seem that horizontally the Twiss parameters are quite similar, but vertically the results are very different. Trace only takes into account linear forces during the bending process, and so that might be the reason for this. There is no change in emittance in Figure 60 as Trace assumes that it stays constant through the LEBT, because the momentum spread was set to zero, meaning there was no simulated Emittance growth.

6.2.3: Data Analysis

A method to show how well a curve is fitted to measured data is the "chi-square test for goodness of fit". This method gives the square of the difference between the fitting function and measured data and is written as [6-9]:

$$\chi^2 = \sum_i^n \frac{\left[f(x_i) - y_i\right]^2}{f(x_i)} \qquad (6.2.3.1)$$

Where i is the i^{th} measurement in n measurements, y_i is the measured value at x_i and $f(x_i)$ is the value of the fitted curve at that measurement point. The $f(x_i)$ on the denominator is the weighting value. However, for these results, each measurement point was weighted the same,

and so the average value of the beam widths was used in place. The chi-square value should be minimised, this means when there is the least difference between the fitted curve and the measured data, and then the "best-fit" is found. The chi-square value for the final emittance and Twiss parameters was χ^2=0.32, and this was the minimum number found when using a MathCAD minimising function. From [6-9] this shows that the curve is 80% fitted to the measured data, for a function with 2 degrees of freedom (number of measurements minus number of parameters found).

6.2.4: Calibration value

It was only possible to fit the theoretical data to the measured beam widths if the calibration factor (the ratio of Gauss per Ampere) was changed into a free parameter. The best fit was found with 29.1 G/A, instead of 33.2 G/A, which was given in the LEBT trace file.

Figure 61 shows how the beam width against current has changed as a result of these measurements. For the initial beam width measurement, the solenoid was set at 131Amps, and so it now can be seen why there was a difference in simulation and the measured result.

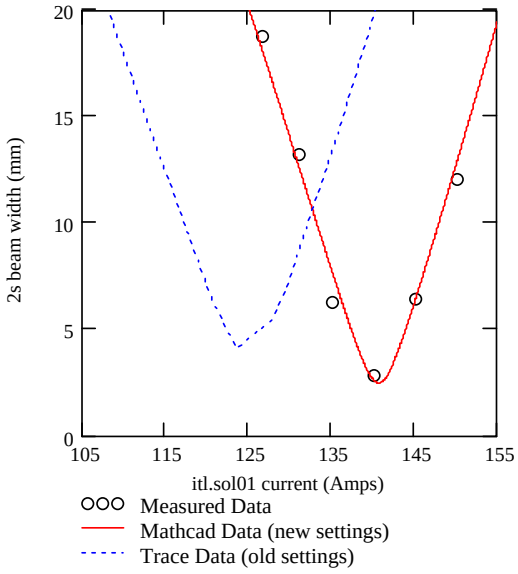

Figure 61: Showing how the simulation data changed from the measurements.

6.3: Emittance Measurement of Indium

6.3.1: Method

The slit scan method was also used to calculate the Emittance of the Indium 21+ beam, which the ECR source provided in the summer of 2003.

The currents of ITL.SOL01 were chosen to co-inside with the ratio of the charge to mass ratios between Pb^{27+} and In^{21+} particles. This is given as:

$$Curr_{In} = Curr_{Pb} \cdot \frac{\left(\frac{q_{Pb}}{m_{Pb}}\right)}{\left(\frac{q_{In}}{m_{In}}\right)} \qquad (6.3.1.1)$$

Where “Curr” is the current in the solenoid, q is the charge on the particle, and m is the mass. From this, we can relate the two sets of measurements.

Extraction voltage	14.30 kV
Particle / Atomic mass	In /115
Rest Mass	1.07 x 10^5 MeV
Charge State	21+
Velocity (β)	0.00237 c
Energy of particle / Energy per nucleon	0.30 MeV / 2.61 keV/u
Current at nominal setting (in ITL.MFC02)	85 μA

Table 17: Parameters for the Indium emittance measurements.

6.3.2: Results

Figure 62 shows the results of the beam widths for the In^{21+} beam, and the comparison with the lead beam.

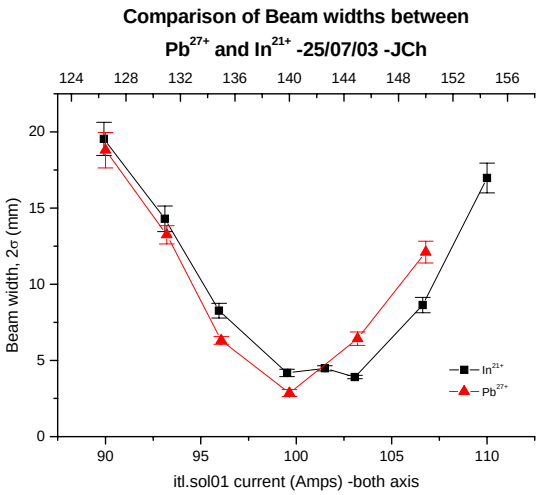

Figure 62: The Indium beam width results, with a comparison to the lead beam widths.

In Figure 62, the top axis and the bottom axis have been put together, to give corresponding charge to mass ratios, as given in (6.3.1.1). It is noticeable that the beam widths are similar

when the waist is after the slits (solenoid strength < 100), but they are different when the waist is before the slits. In Chapter 5, measurements showed that there was less total ion current with indium than with lead. Less current reduces space-charge effects, which would be most affective at the waist, where all the particles are closest together. This could explain the difference in results, as the Indium particles disperse slower after the waist.

The widths for the Indium beam were put into the MathCAD file, and a theoretical curve fitted to the data.

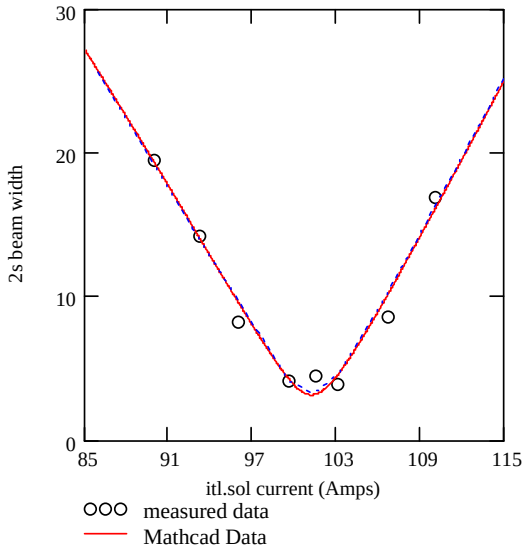

Figure 63: The MathCAD fitted curve for the indium beam widths.

Again Trace-3D was used to check the data, and it is shown in Figure 63 that the two programs are similar. After fitting the Twiss parameters were found to be:

α	β	ε_{4rms} (mm.mrad)
-0.2	0.03	120

Table 18: Results of the horizontal and vertical emittance measurement.

This was found using the "Chi-square best-fit" method as shown with the lead measurements. With these parameters, chi minimised to give χ^2=0.697, and this corresponds to a fitting rating of 70%, given that this measurement had 5 degrees of freedom. This reduction in confidence is due to the waist point being away from the fitted curve.

6.4: Conclusions

This chapter introduces a new method to calculate the emittance of the ECR source before the spectrometer, by scanning the spectrometer slits across the beam and fitting the resulting beam width as a function of solenoid strength. The previous beam profile monitor, a SEM grid consisting of an array of wires, was broken due to the high beam intensity. The new technique using the slits did not require the installation of any additional equipment, and allows the measurement of a single charge-state due the spectrometer. For Pb^{27+}, the emittance was found to be 100mm.mrad un-normalised, at a position of 0.851m before the first solenoid. At the same position, the emittance of the In^{21+} beam was 120mm.mrad un-normalised. The emittance has not been measured at this position. When the source was built, the beam emittance was measured on a test beam, after passing a spectrometer, and a value of 125mm.mrad was found. This means the measurements here show the source has improved its performance since then, and the method is a reliable way to take the emittance, as it was expected the indium beam would have a larger value [6-10]. A more accurate emittance device is currently being installed in 2004, and this will also test the accuracy of this method. During these measurements, a slit misalignment was discovered, as well as an error in solenoid calibration. These measured beam parameters were also used to determine if there was any beam loss in the first solenoid. Only a 2.5% increase in intensity was expected, and with source instabilities this was not recorded. It was decided this loss was not significant to warrant further study.

Chapter 7: Beam Profile preliminary measurements

7.1: Introduction

As part of the restudy of Linac 3 in 2003, it was required that a 2 two-dimensional beam profile of the source be measured. The main concern for this experiment was the lifetime of the screen, as some estimates suggested it could be as low as 100ms for the beam from the Linac 3 ECR source. It was decided that a test measurement should be performed, which would allow the prediction of the lifetime of different types of screen, when they were placed directly after the source. Therefore, two different screens were prepared and placed into a lower intensity beam. Presented here are the results of the two test screens.

7.2: Experimental Apparatus

Using a straight through output of the first ITL bending magnet, the beam could be sent to a test area, shown in Figure 64. This was convenient because it was in a direct path from the source, so that the beam the test screen received would be similar in mixture and duration to the actual beam profile measurement. Also there was already a vacuum valve in place so the vacuum of the Linac would not be affected when inserting or changing the screen.

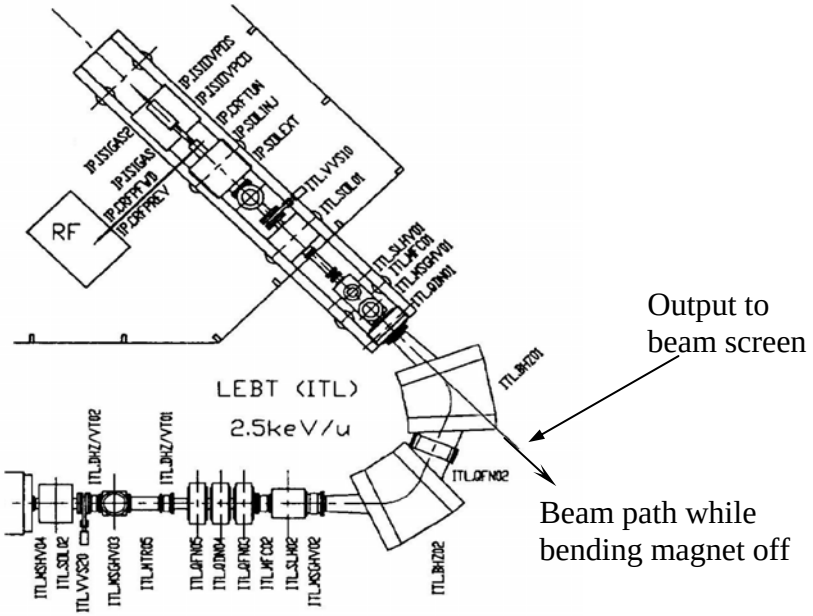

Figure 64: A view of the LEBT showing the position of the output of the first bending magnet.

However, the output from the magnet had a beam pipe diameter of 16mm. This is much smaller than the beam size at that point, even when the first solenoid is used to focus the beam as small as possible. This meant that the beam screen would only intercept a fraction of the beam, and so the lifetime of the screen would increase.

A schematic view of the beam line is shown in Figure 65. The screen was connected to the screen chamber by a wire, and the chamber was electrically insulated from the rest of the beam line by ceramic insulators. So the amount of current hitting the screen could be measured, a 10kΩ resister was placed in parallel with the screen chamber and the oscilloscope taking the current. The screen was placed at an angle of 45° to the direction of the beam, so that the light created by the screen would be visible from the view ports on either side of the

screen chamber. After the second insulator, the beam chamber was connected to an X-piece, where the up-to-air valve, vacuum gauges and pump were situated.

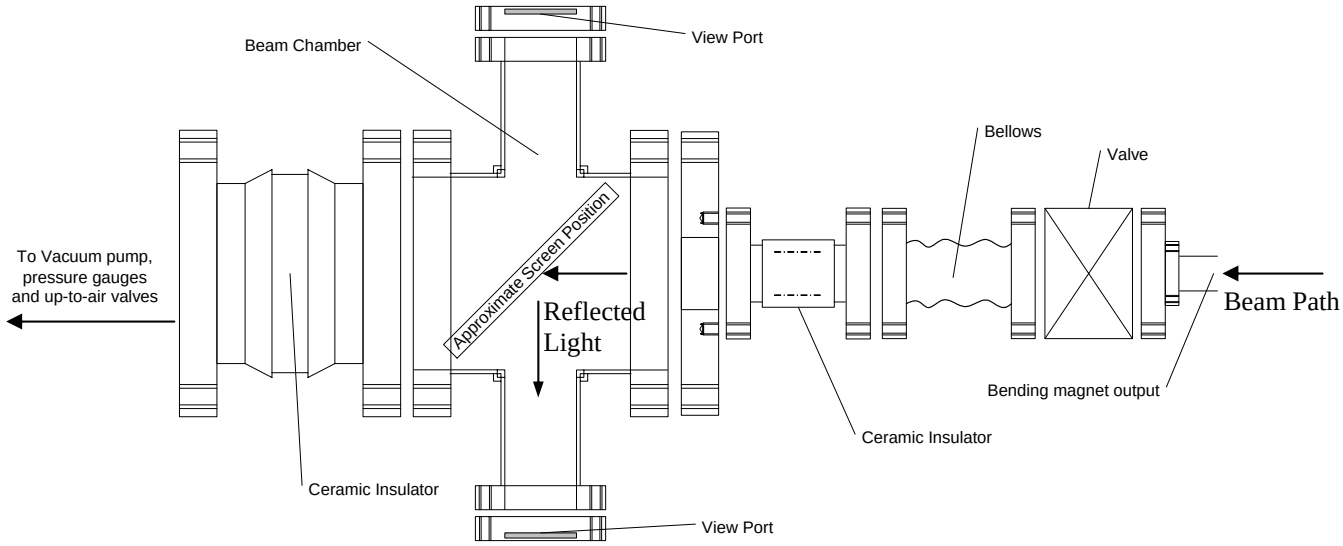

Figure 65 : Schematic view of the beam chamber.

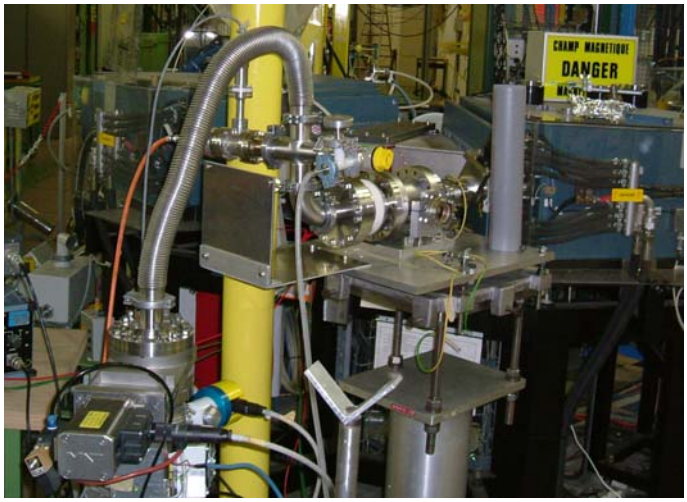

Figure 66: A photo of the experiment.

The first screen consisted of a phosper-47 layer on an aluminium plate. The layer of P-47 was hoped to be sufficiently thin to allow the ions to penetrate through and reach the metal, making sure there was no build up of charge. This screen was viewed by a camera from the front.

The second screen had a Schott Glass main layer, and coated with 50nm of aluminium to remove the charge. As the screen was placed 45° to the beam path, the ions travelled through ~71nm of the Al layer before illuminating the glass. A visual inspection suggested that the layer was not very uniform. With this screen, the florescence was viewed from the back of the screen, the side without the Al layer on it.

7.3: Method

The P47 screen was placed into the beam screen area, and then the chamber was evacuated. After several days, to allow the pressure to stabilise, the pressure was 3.5×10^{-7}mbar. This was sufficient to reduce the pressure difference on either side of the valve. When the valve was opened, the pressure rose to 6×10^{-7}mbar.

Firstly, a scan of the solenoid ITL.SOL01 was completed to find the current entering the beam screen area. For this scan, the quadrupole ITL.MFC01 and the first bending magnet were switched to stand-by, which means they had no magnetic field in them.

To measure the light intensity on the screen, a Digital Vision Technologies MICAM VHR2000 (normal BW CCD) was set up and placed to look into one of the side windows. A tube, between the window and the camera lens and a black cloth was installed to keep as much background light out of the beam chamber. However, light could still be seen though the camera and so the main lights of the Linac area were switched off too. The images were

captured with a PC and a Twist3 PCI frame grabber, and the image could be synchronised with the beam.

The coated glass screen produced a lot less amount of light, and so a doubled intensified, gated proxitronic camera NANOCAM HF 4 V 5N had to be used to take pictures of the beam, and again these were saved to computer.

After 2 hours, the camera was replaced with a photo-multiplier. This only has one effective pixel, because it measures the amount of photons entering its aperture, and not the distribution. The signal was then captured on an oscilloscope, and read to a PC every 61 seconds over 15 hours.

7.4: Results

A selection of waveforms from the solenoid scan is given in Figure 67. This shows the duty cycle of the source, which is 50ms in 10Hz mode. The peaks at the beginning and the end are where the RF source microwave generator is turned on and off respectively, and also vary according to the charge state which is most focused into the screen area. If there is a peak at the end then it is more likely to be lead ions and O^{1+}, as it has slow decay time after the after-glow [7-1]. Figure 68 shows the amount of current hitting the beam screen as a function of the ITL.SOL01 current. From this, it can be seen that the maximum current was at 125Amps with a value of 18μA, within the time period 0.04 to 0.08 seconds on the oscilloscope. Due to the three peaks in this graph, it can be assumed that at the maximum intensity that most of the beam is oxygen. However, there was no electron suppression in this area, and experience suggests that the actual beam is approximately 50% of the electrical current.

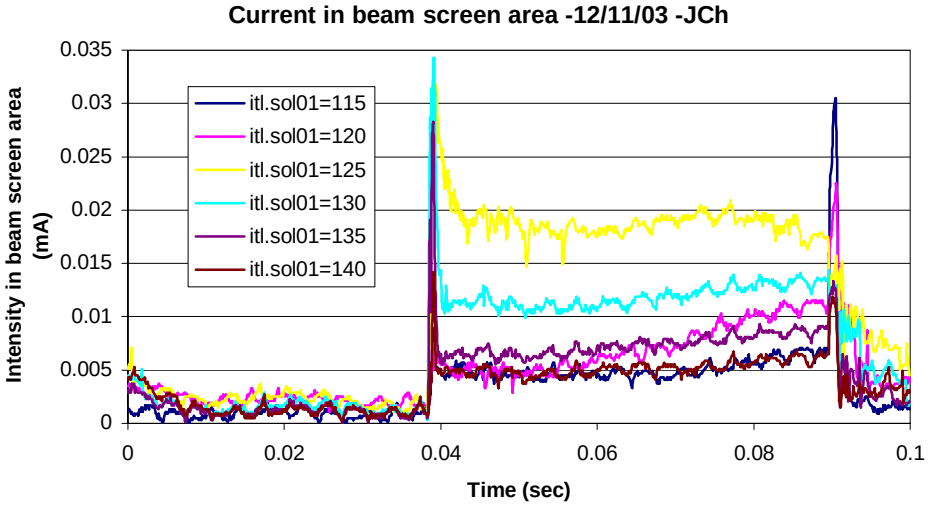

Figure 67: A selection of waveforms from the solenoid scan, showing the current onto the screen.

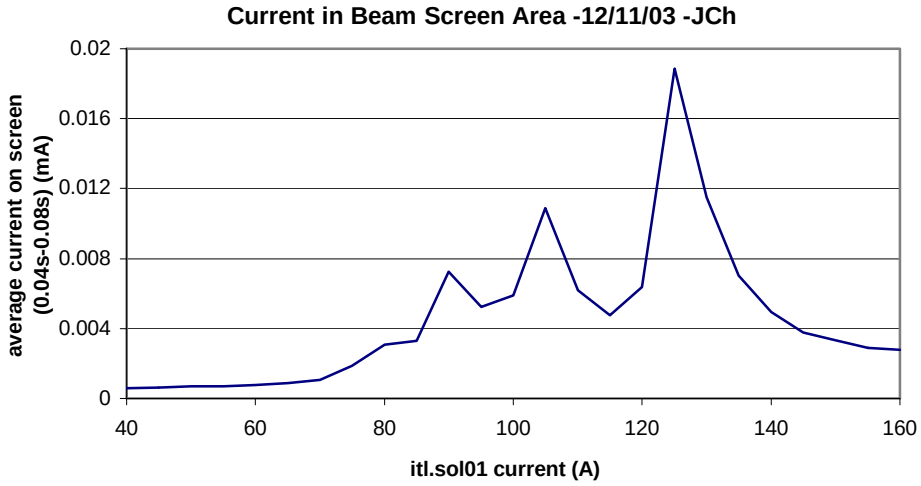

Figure 68: The current hitting the beam screen as a function of solenoid strength.

With the phosphor-47 screen, there was plenty of visible light, but periodically there were bright flashes. This can be seen in the set of pictures in Figure 69. It is thought that the phosphor charges up until a breakdown occurs. This is not normally a problem because the layer of P47 is usually thinner than the penetration depth of the ions, and so the charge would

dissipate away through the aluminium plate, but did not occur in this instance. The rate of breakdown increased when the intensity of the beam into the chamber area was also increased.

The camera was set to trigger with the 10Hz source trigger, SRC, which occurs at the start of the heating phase. At every trigger, the camera recorded a set amount of pictures with a spacing of 20ms, before waiting for the next trigger. With this spacing, the data recorded shows that there was light coming off the screen many milli-seconds after the afterglow. As the decay time (to 10%) of P47 is 120ns [7-2], it is thought that electrons are being pulled into the plate, by the positive charge on the plate, as the light continues long after the beam.

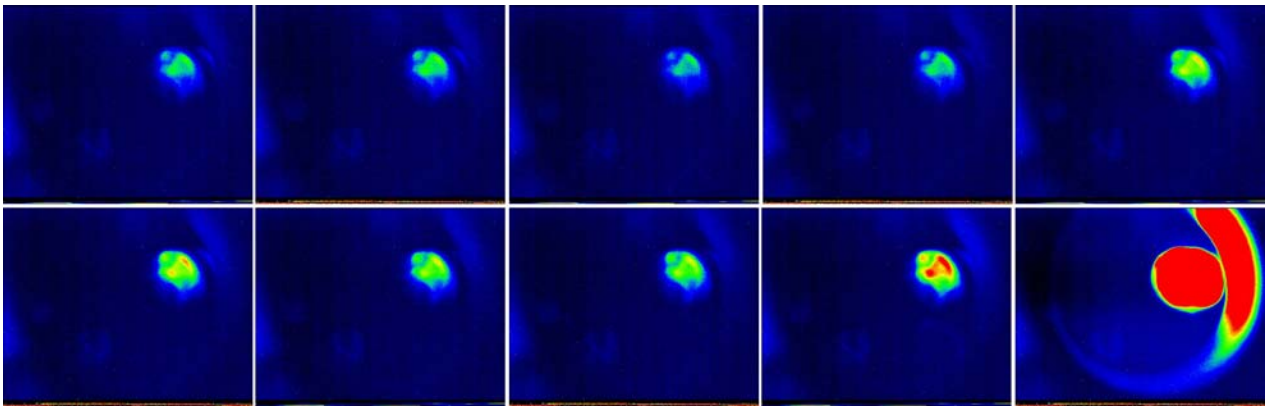

Figure 69: Showing the build up of charge and then a break down.

Before the flashes on the screen, it is possible to see the shape of the beam. An example is shown in Figure 70, and here the red intensity takes the shape of a triangle, showing the beam is star shaped, with a hollow centre. This proves an incorrect assumption, that the beam has a Gaussian distribution, was used in Chapter 6. However, because of the small aperture of the output from the bending magnet, we cannot say that this is the distribution of the beam. The profile is heavily distorted by the accumulated charge on the screen.

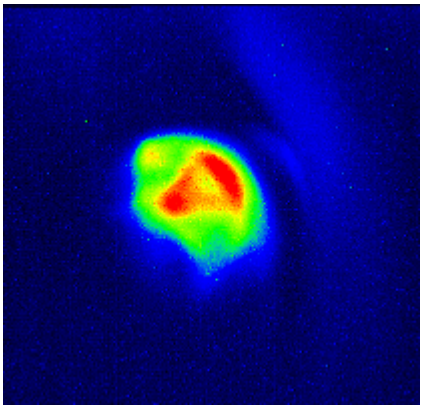

Figure 70: Image-0393, an example where the shape of the beam can be seen.

A few pictures were taken with the intensified camera viewing the second screen, are shown in Figure 72. This time, the camera was set to trigger with RBO, at a gain of 40%, and a time frame of 1ms, and then the delay after the trigger could be chosen as displayed on each image in Figure 72. The timing diagram shows the place in the duty cycle where each photo was taken (the black dashed lines). Each picture is an average of 16 consecutive shots.

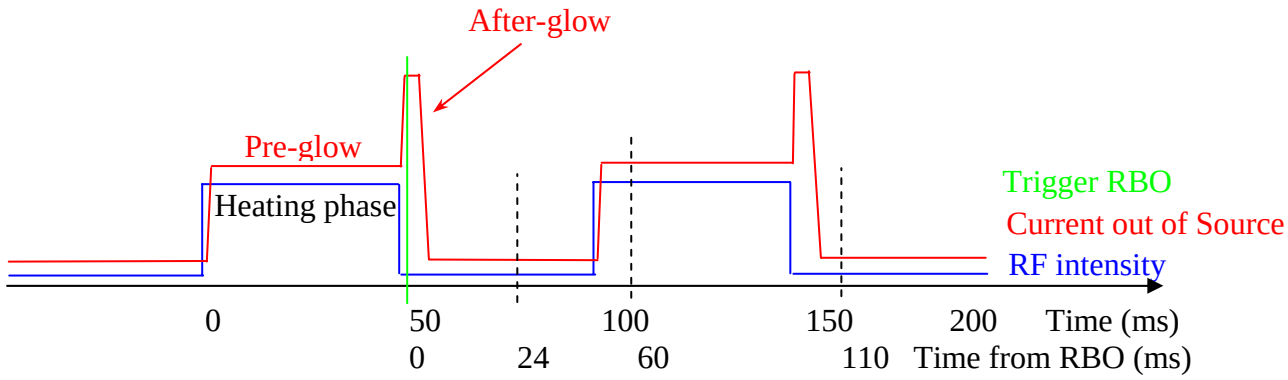

Figure 71: Timing diagram.

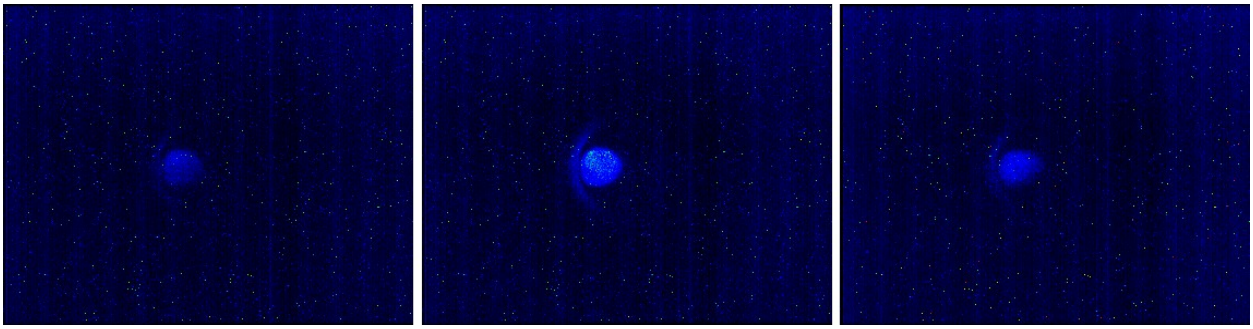

24ms 60ms 110ms

Figure 72: Pictures from the glass screen at the time shown after trigger RBO.

This shows we can see the beam, and we can see the variation of intensity in time. However, it is impossible to get a beam profile reading from these because of the small entrance of the output from the bending magnet chops most of the beam.

With the photo-multiplier in place of the intensified camera, a typical waveform recorded on the oscilloscope is given Figure 73.

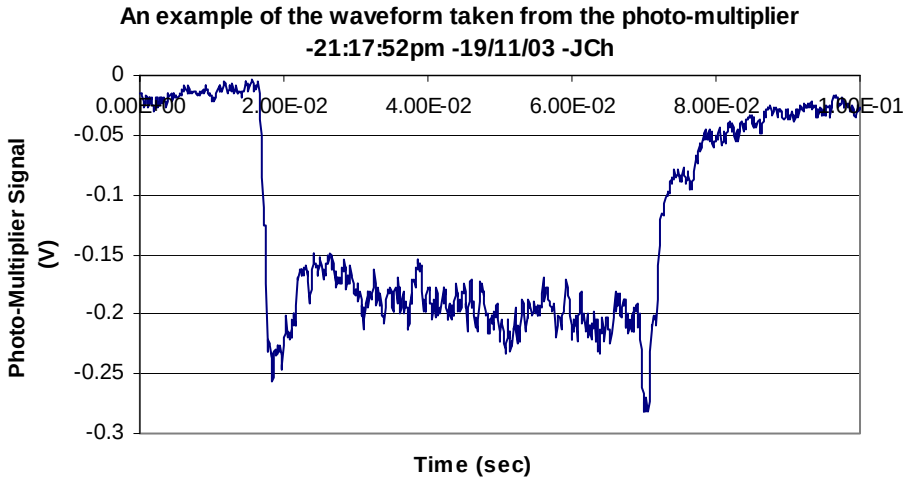

Figure 73: A typical example of the signal from the photo-multiplier.

The signal against time graph is shown in Figure 74. The beam was first placed onto the screen at 16:00hrs, which is 2 hours before the graph starts. During this time the intensified camera was measuring the profile as written above. It can be seen that at approximately 20:00hrs, the intensity of the light began to increase. This is where the aluminium layer started to be sputtered away, and so the layer was not scattering as many ions, and so more light was produced. By the end of the experiment, which the screen was incident in the beam for 15 hours, the entire aluminium layer had been removed. This is shown by the flat line at the very end of Figure 74 after the peak, and also in Figure 75, where the hole can be seen clearly. The reason for the flat line from 00:30hrs to 08:00hrs is that the waveform was saturated on the oscilloscope. The drop in intensity at 08:24 is where the beam was taken off the screen for 1 minute. This peak shows us that no light was viewed when the bending magnet was switched on, indicating that X and γ rays did not cause light emission from the screen.

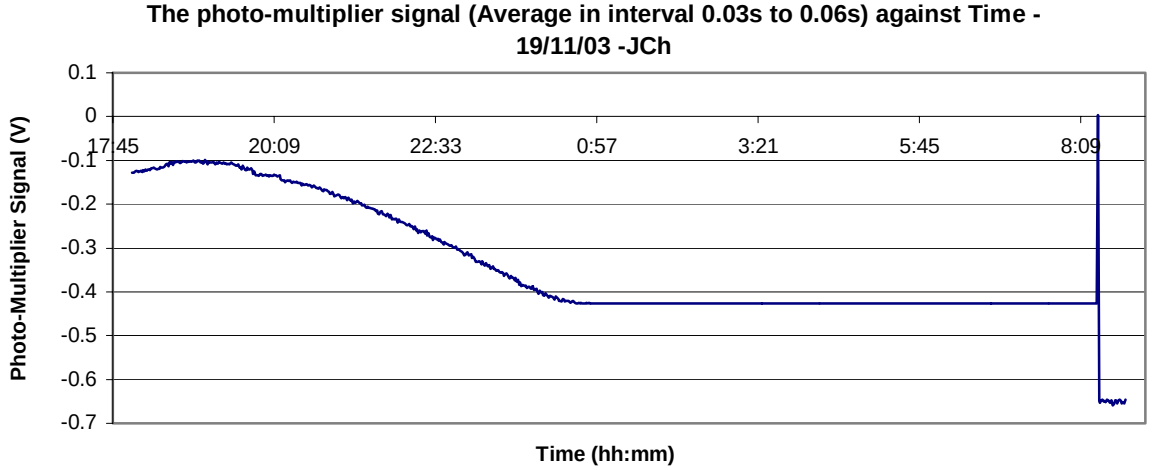

Figure 74: Showing the Signal of the photo-multiplier against time.

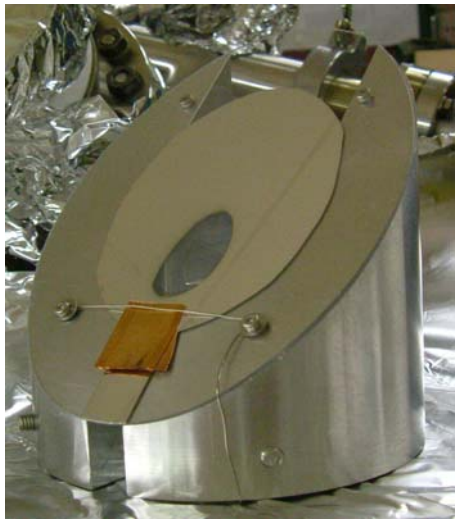

Figure 75: The beam screen on its holder after the experiment.

To see how much of the aluminium layer was removed, the resistance of each section of the screen was measured. Outside of the aluminium section, where no layer was placed, the voltmeter gave an open current reading, even when the electrodes were separated by 1mm. On the untouched aluminium layer, the voltmeter gave an average reading of $2.5\Omega cm^{-1}$. Inside the hole where the layer had been eroded, the voltmeter again did not give a reading anywhere, and again even with the two electrodes 1mm apart. This means that the entire aluminium layer was removed by the beam.

The area of hole was measured by the equation to find the area of an ellipse:

$$A = \pi wh \tag{7.4.1}$$

Where w and h are the width and height of the ellipse respectively. Hence the area was found to $330mm^2$. As the solenoid ITL.SOL01 was set to 125Amps during the experiment, Figure 68 shows us that the peak current hitting the screen was 0.0188mA. The yellow waveform in Figure 67 was averaged over 0.1 second, and this gives the average continuous current hitting

the screen, which was 11μA. This corresponds to 11μCs^{-1} hitting the screen. With the area of the hole measured we have 33nCs^{-1}mm^{-2} hitting the screen. The screen lasted 4 hours, which is 1.4x10^{4}s, so the total amount of charge that hit the screen, before the erosion of the aluminium layer had a detrimental effect, was **47.5mCcm^{-2}**.

To estimate the length that a similar screen would last when placed directly into the beam, at approximately the position of Faraday cup ITL.MFC01, we have do a similar calculation. The average current entering Faraday cup ITL.MFC01 [7-1] is 100μA, and so the charge is 100μCs^{-1}. The size of the beam at this point varies according to the strength of ITL.SOL01, and also the different charge states have different beam widths [7-3]. As I have taken the current in Faraday cup ITL.MFC01, then that is the amount of charge entering the aperture of the cup, which has a diameter of 30mm [7-3]. So the area is 707mm^{2} and hence the charge density is **14.1μCs^{-1}cm^{-2}**.

According to the units of the two bold numbers above, dividing the first by the second will give the seconds that the real beam screen will last before it's aluminium layer becomes eroded. From these calculations the length of time it will last is **50 minutes**.

7.5: Conclusion

Although the results for the phosphor coated aluminium screen have not been successful, it opens up the opportunity to explore other ways to overcome the problem. One possibility is to coat the phosphor with an aluminium layer, similar to the other screen, to stop the charge build up. However this would reduce the lifetime to about an hour as shown with the other screen.

The Schott Glass and aluminium coated screen is a viable possibility for the beam profile measurement directly after the source, approximately where Faraday Cup ITL.MFC01 is presently located. This report has shown that the beam can be seen, and that a screen in that place, and of a similar nature would last for 50 minutes. This gives enough time to complete the profile measurements. However, with increased X and UV rays from the source and an added thermal load, the lifetime of the screen may decrease.

Chapter 8: Further Work

8.1: The Laser Ion Source

Having found an initial value of the emittance of the LIS, it can be seen the source is not very stable. More measurements could be taken to determine whether the emittance depends on ion intensity, in particular as the ion current is increased. The stability of the ion beam may be linked to the stability of the MO-PA laser system, as the regenerator was broken at the time of the measurements. However, the LIS has now been shipped to Russia, where tests will be performed on medium mass elements [8-1], and then will be used as a high current injector for the ITEP-TWAC (TeraWatt Accumulator) project, provided the reliability issues can be overcome. Maybe one day the research of the LIS experiment will fuel a future ion source at CERN.

8.2: Linac 3 and the Electron Cyclotron Resonance Ion Source

In this report, only a few measurements of the restudy of Linac 3 are presented. Other experiments, competed by the HSL section, are still being completed to help our understanding of the ECR source and the Linac. An emittance device is being installed at the place of the spectrometer slits. However, this device cannot distinguish between charge states, and maybe might not be able to get a reading. Also the beam screen may be placed at this position. Again, the 2 dimensional beam profile that is recorded will be a superposition of the intensities of all the charge states, and this may cause problems.

Even though the study has not been completed, methods to find extra intensity are being investigated. Using the present ECRIS, a multi-charge accelerating procedure is being

studied, which either requires a re-location of the source, or a three magnet bending system. Both these methods need further study to verify their efficiency. Presently, CEA Grenoble is building a new ECRIS, with a larger plasma volume and optimised magnetic system, with the aim to deliver twice the Pb^{27+} ion current. When installed all the parameters of the Linac would need to be re-optimised, and maybe another study of the entire length will be required, for further understanding of the new source. The new method to perform beam profiles in Chapter 4 will be useful for this.

Appendix A: The MathCAD Fitting Sheet

Shown here is the program that fits the measured beam width curve to theoretical beam width values to find the Twiss parameters of the beam.

$B\rho := 0.0564741$

$k(gau) := \frac{gau}{2B\rho \cdot 10000}$

$l := 0.234$

$C(gau) := \cos(k(gau)\cdot l)$

$S(gau) := \sin(k(gau)\cdot l)$

$cali := 29.1$

$TBW := \begin{pmatrix} 18.79861 \\ 13.24737 \\ 6.31115 \\ 2.85978 \\ 6.42843 \\ 12.10577 \end{pmatrix}$ $BWcurr := \begin{pmatrix} 126.5 \\ 131 \\ 135 \\ 140 \\ 145 \\ 150 \end{pmatrix}$ $traceBW := \begin{pmatrix} 25.9052 \\ 9.1294 \\ 5.0167 \\ 2.4803 \\ 5.2886 \\ 18.8030 \end{pmatrix}$ $traceGs := \begin{pmatrix} 3500 \\ 3900 \\ 4000 \\ 4100 \\ 4200 \\ 4500 \end{pmatrix}$

$$R1(gau) := \begin{pmatrix} C(gau)^2 & \frac{S(gau)\cdot C(gau)}{k(gau)} & S(gau)\cdot C(gau) & \frac{S(gau)^2}{k(gau)} \\ -k(gau)\cdot S(gau)\cdot C(gau) & C(gau)^2 & -k(gau)\cdot S(gau)^2 & S(gau)\cdot C(gau) \\ -S(gau)\cdot C(gau) & \frac{-S(gau)^2}{k(gau)} & C(gau)^2 & \frac{S(gau)\cdot C(gau)}{k(gau)} \\ k(gau)\cdot S(gau)^2 & -S(gau)\cdot C(gau) & -k(gau)\cdot S(gau)\cdot C(gau) & C(gau)^2 \end{pmatrix}$$

$BWsqr := \left(\frac{TBW}{1000}\right)^2$ $BWgs(cali) := cali \cdot BWcurr$

$j := 0 .. 6$

$i := 0 .. 5$

first gues s'

$\alpha x := -0.885$

$\beta x := 0.04$

$\gamma x := \frac{1 + \alpha x^2}{\beta x}$

$\varepsilon x := 100 \cdot 10^{-6}$

$\gamma x = 44.581$

$$R2(L) := \begin{pmatrix} 1 & L & 0 & 0 \\ 0 & 1 & 0 & 0 \\ 0 & 0 & 1 & L \\ 0 & 0 & 0 & 1 \end{pmatrix}$$

$R(gau) := R2(0.851)\, R1(gau)\cdot R2(0.445)$

$$\frac{\sum_i TBW_i}{6} = 9.959$$

$$sigS(\alpha x, \beta x, \varepsilon x) := \begin{pmatrix} \beta x\cdot\varepsilon x & -\alpha x\cdot\varepsilon x & 0 & 0 \\ -\alpha x\cdot\varepsilon x & \gamma x\cdot\varepsilon x & 0 & 0 \\ 0 & 0 & \beta x\cdot\varepsilon x & -\alpha x\cdot\varepsilon x \\ 0 & 0 & -\alpha x\cdot\varepsilon x & \gamma x\cdot\varepsilon x \end{pmatrix}$$

$sigF(gau, \alpha x, \beta x, \varepsilon x) := R(gau)\cdot sigS(\alpha x, \beta x, \varepsilon x)\cdot R(gau)^T$

$horzwidth(gau, \alpha x, \beta x, \varepsilon x) := 1000\sqrt{(sigF(gau, \alpha x, \beta x, \varepsilon x)_{0,0})}$

$vertwidth(gau, \alpha x, \beta x, \varepsilon x) := 1000\sqrt{(sigF(gau, \alpha x, \beta x, \varepsilon x)_{2,2})}$

$horiz(gau) := horzwidth(gau, \alpha x, \beta x, \varepsilon x)$

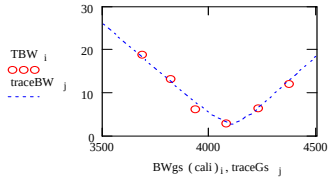

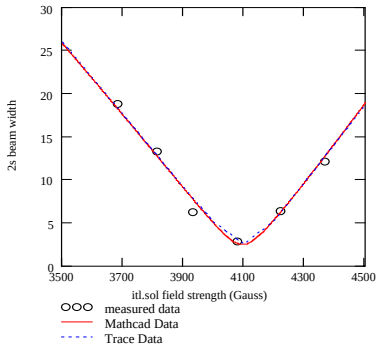

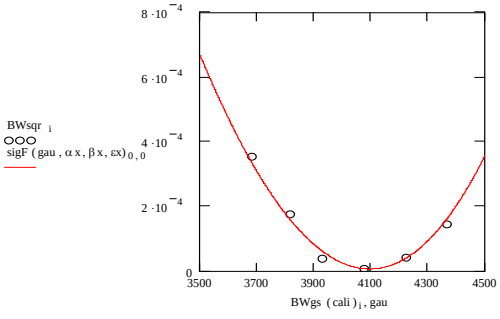

$gau := 4000$

$Minimize(horiz, gau) = 4.094 \times 10^3$

$$chisqr(cali, \alpha x, \beta x, \varepsilon x) := \sum_i \left[\frac{(horzwidth(BWgs(cali)_i, \alpha x, \beta x, \varepsilon x) - TBW_i)^2}{9.959}\right]$$

$chisqr(cali, \alpha x, \beta x, \varepsilon x) = 0.32$

$$Minimize(chisqr, cali, \alpha x, \beta x, \varepsilon x) = \begin{pmatrix} 29.092 \\ -0.904 \\ 0.039 \\ 9.986 \times 10^{-5} \end{pmatrix}$$

$horzwidth(BWgs_i, \alpha x, \beta x, \varepsilon x)$

9.959

Bibliography

[1-1] http://user.web.cern.ch/user/cern/CERNName.html

[1-2] http://public.web.cern.ch/Public/about/what/history/history.html

[1-3] http://lhc.web.cern.ch/lhc/general/gen_info.htm

[1-4] http://edms.cern.ch/cedar/plsql/navigation.tree?cookie=2424750&p_top_id=1205733706&p_top_type=P&p_open_id=1755811172&p_open_type=P

[1-5] http://scrivens.home.cern.ch/scrivens/lis/home.html

[1-6] http://linac2.home.cern.ch/linac2/default.htm

[1-7] http://morsch.home.cern.ch/morsch/docs/WEOA01A.PDF

[1-8] M. Channel, "*Ions for LHC: LEIR and PS*". Presented 28th June 2002 -LHC Ions Workshop.

[2-1] H. Wiedemann, "*Particle Accelerator Physics I*". Second Edition, Springer 2003.

[2-2] Fifth General CERN Accelerator Physics Course, 1992 Vol I.

[2-3] http://mathworld.wolfram.com

[2-4] K. R. Crandall, D. P. Rusthoi, "*Trace 3-D Documentation*", third edition 1997, University of California.

[2-5] http://www.triumf.ca/people/baartman/ISAC/training/ISACtraining.html

[2-6] Private Discussion with R. Scrivens.

[2-7] K. Wille, "*The physics of particle accelerators: an introduction*". Oxford University Press, 2000.

[3-1] Private Discussion with S. Kondrashev.

[3-2] See [1-5].

[3-3] G. Shirkov, "*Highly Charged Ion Production in ECR source of Heavy Ions*". CERN/PS 94-33 (HI).

[3-4] "*The ECR4 Lead Ion Source, How, What, Why.*" Unknown author, Unpublished.

[3-5] G. Shirkov, "*Fundamental processes determining the highly charged ion production in ECR ion sources*". Nuclear Instruments and Methods in Physics Research A322 (1992) 161-165.

[3-6] See [2-6].

[3-7] http://nautilus.fis.uc.pt/st2.5/scenes-e/elem/e08292.html

[3-8] C. Hill, "*Ion and Electron Sources*", CERN summer school seminar (http://linac2.home.cern.ch/linac2/seminar/seminar.htm)

[4-1] J. Chamings, S. Kondrashev, R. Scrivens, A. Shumshurov, "*First Emittance Measurements and Continued Source Current Measurements, 12 March 2003*", LIS Note 2003-11.

[4-2] J. Chamings, "*Examples of CCD Camera and Zoom Lens Settings*", LIS Note 2003-02.

[4-3] R. Scrivens, "*Extraction of an Ion Beam from a Laser Ion Source*", Ph.D Thesis, University of Wales, Swansea 1999.

[4-4] http://ps-div.web.cern.ch/ps-div/Meetings/Technical/TM117.pdf

[5-1] V. Coco, J. Chamings, A. Lombardi, E. Sargsyan and R. Scrivens, "*Acceleration of Several Charge States of Lead Ion in CERN Linac 3*", to be presented at the Linear Accelerator Conference, August 2004, Lubeck, Germany.

[5-2] Linac 3 restudy - Meeting Summary - 8 May 2003.

[5-3] See [2-6].

[6-2] P. Spadtke, "*Numerical simulation of ion related problems*", Rev. Sci. Instrum. 63 (4), April 1992.

[6-2] http://mathworld.wolfram.com/GaussianFunction.html

[6-3] LINAC 3 DESIGN report PS note 94-01.

[6-4] Trace3D simulation data of Pb27+ for the LEBT of Linac 3. (at 10/06/03)

[6-5] N. Catalan Lasheras, "*A new tool to calculate emittances from profile measurements in the filter line of Linac 3*", PS/HI Note 95-05.

[6-6] R. Scrivens, "*ECR4 Ion Extraction*", RS Note 2003-20.

[6-7] Technical drawing, "*Dimensions des ouvertures*", no. LIN3-8024.

[6-8] J. Chamings, V. Coco, A. Lombardi, R, Scrivens, "*Measurements of emittance and twiss parameters in LINAC 3: comparison between measurements and simulations*", AB-Note-2004-002-ABP.

[6-9] P.R. Bevington, D.K. Robinson, "*Data Reduction and error analysis for the physical sciences*", second edition 1992, McGraw-Hill Inc.

[6-10] See [2-6].

[7-1] J. Chamings, "*Charge State Distribution Scans on LEBT of Linac 3*" RS Note 2003-19.

[7-2] http://www.appscintech.com/pdf-files/data-sheets/phosphor-data-sheet24-p47_iss2.pdf

[7-3] J. Chamings, "*Beam Profile Measurements to calculate Emittance in the LEBT of Linac 3*", RS Note 2003-21.

[8-1] S. Kondrashev, "*Laser Ion Source Based on 100J / 1Hz CO2-Laser System*", Proc. International Ion Source Conference, September 2003, Dubna, Russia.

Filename: Chamings-MPhysDissertation
Directory: C:\Documents and Settings\julie\Desktop
Template: C:\Documents and Settings\julie\Application Data\Microsoft\Templates\Normal.dot
Title: Chapter 1:
Subject:
Author: James Chamings
Keywords:
Comments:
Creation Date: 04-May-04 3:21 PM
Change Number: 8
Last Saved On: 10-May-04 10:20 AM
Last Saved By: julie
Total Editing Time: 77 Minutes
Last Printed On: 10-May-04 10:24 AM
As of Last Complete Printing
Number of Pages: 111
Number of Words: 21,974 (approx.)
Number of Characters: 106,576 (approx.)